Jefferson Lab PAC 44

Nuclear Exclusive and Semi-inclusive Measurements with a New CLAS12 Low Energy Recoil Tracker

ALERT Run Group[†]

EXECUTIVE SUMMARY

In this run group, we propose a comprehensive physics program to investigate the fundamental structure of the ^{4}He nucleus. An important focus of this program is the study of the partonic structure of bound nucleons. To this end, we propose next generation nuclear measurements in which low energy recoil nuclei are detected. Tagging of recoil nuclei in deep inelastic reactions is a powerful technique that will provide unique information about the nature of medium modifications, through the measurement of the EMC ratio and its dependence on the nucleon off-shellness. Other important channels are the coherent exclusive Deep Virtual Compton Scattering (DVCS) and Deep Virtual Meson Production (DVMP) with a focus on the ϕ meson. These are particularly powerful tools enabling model-independent nuclear 3D tomography through the access of partons' position in the transverse plane. These exclusive measurements will also be used to study the generalized EMC effect and for the first time access the gluonic tomography of nuclei via exclusive ϕ electroproduction channel. Finally, we propose to measure tagged DVCS on light nuclei (d, ^{4}He) to extract both quasi-free neutron and bound neutron and proton Generalized Parton Distributions (GPDs). In both cases, the objective is to study nuclear effects and their manifestation in GPDs including the effect of final state interactions in the measurements of the bound nucleon beam spin asymmetries and the EMC ratio.

At the heart of this program is the Low Energy Recoil Tracker (ALERT) combined with the CLAS12 detector. The ALERT detector is composed of a stereo drift chamber for track reconstruction and an array of scintillators for particle identification. Coupling these two types of fast detectors will allow ALERT to be included in the trigger for efficient background rejection, while keeping the material budget as low as possible for low energy particle

---

detection. ALERT will be installed inside the solenoid magnet instead of the CLAS12 Silicon Vertex Tracker. We will use an 11 GeV longitudinally polarized electron beam (80% polarization) of 150 nA on a gas target straw filled with deuterium or ^{4}He at 3 atm to obtain a luminosity of 3.10^{34} cm^{-2}s^{-1}. In addition we will need to run hydrogen and ^{4}He targets at different beam energies for detector calibration. The following table summarizes our beam time request:

Measurements	Particles detected	Targets	Beam time request	Luminosity*
ALERT Commissioning	p, d, ^{4}He	H and He	5 days	Various
Tagged EMC	p, ^{3}H, ^{3}He	^{2}H and He	$20 + 20$ days	3.10^{34} cm^{-2}s^{-1}
Tagged DVCS	p, ^{3}H, ^{3}He	^{2}H and He	$20 + 20$ days	3.10^{34} cm^{-2}s^{-1}
Nuclear GPDs	^{4}He	He	extra 10 days on He	6.10^{34} cm^{-2}s^{-1}
Additional Topics	p, d, ^{3}H, ^{3}He	^{2}H and He	$20 + 20 + (10)$ days	$3(6).10^{34}$ cm^{-2}s^{-1}
TOTAL			**55 days**	

---

*This luminosity value is based on the effective part of the target. When accounting for the target's windows, which are outside of the ALERT detector, it is increased by 60%

Partonic Structure of Light Nuclei

W.R. Armstrong, J. Arrington, I. Cloet, K. Hafidi[†], M. Hattawy[†], D. Potteveld, P. Reimer, Z. Yi

Argonne National Laboratory, Lemont, IL 60439, USA

J. Ball, M. Defurne, M. Garçon, H. Moutarde, S. Procureur, F. Sabatié

CEA, Centre de Saclay, Irfu/Service de Physique Nucléaire, 91191 Gif-sur-Yvette, France

W. Cosyn

Department of Physics and Astronomy, Proeftuinstraat 86, Ghent University, 9000 Ghent, Belgium

M. Mazouz

Faculté des Sciences de Monastir, 5000 Tunisia

J. Bettane, G. Charles, R. Dupré[†], M. Guidal, D. Marchand, C. Muñoz, S. Niccolai, E. Voutier

Institut de Physique Nucléaire, CNRS-IN2P3, Univ. Paris-Sud, Université Paris-Saclay, 91406 Orsay Cedex, France

K. P. Adhikari, J. A. Dunne, D. Dutta, L. El Fassi, L. Ye

Mississippi State University, Mississippi State, MS 39762, USA

M. Amaryan, G. Dodge

Old Dominion University, Norfolk, VA 23529, USA

V. Guzey

Petersburg Nuclear Physics Institute, National Research Center "Kurchatov Institute", Gatchina, 188300, Russia

N. Baltzell[†], S. Stepanyan

Thomas Jefferson National Accelerator Facility, Newport News, VA 23606, USA

[†]Spokesperson

S. Joosten, Z. E. Meziani[†‡], M. Paolone[†]

Temple University, Philadelphia, PA 19122, USA

F. Cao, K. Joo, A. Kim, N. Markov

University of Connecticut, Storrs, CT 06269, USA

S. Scopetta

Università di Perugia, INFN, Italy

W. Brooks, A. El-Alaoui

Universidad Técnica Federico Santa María, Valparaíso, Chile

S. Liuti

University of Virginia, Charlottesville, VA 22903, USA

a CLAS Collaboration Proposal

[‡]Contact person

Abstract

We propose to study the partonic structure of ^{4}He by measuring the Beam Spin Asymmetry (BSA) in coherent Deep Virtual Compton Scattering (DVCS) and Meson Production (DVMP). In the latter, coherent production of ϕ mesons will be measured. Despite its simple structure, a light nucleus such as ^{4}He has a density and a binding energy comparable to that of heavier nuclei. Therefore, by studying ^{4}He nucleus, one can learn typical features of the partonic structure of atomic nuclei. In addition, due to its spin-0, only one chiral-even GPD, H_A, at twist-2 parameterizes its partonic structure.

A major goal of this proposal is to cover a wide kinematical range and collect higher statistics leveraging the knowledge obtained during eg6 running (E08-024), where, for the first time, exclusive coherent DVCS off ^{4}He was successfully measured. The real and imaginary parts of the ^{4}He Compton form factors (CFFs) will be extracted in a model independent way from the experimental asymmetries, allowing us to access the nuclear transverse spatial distributions of quarks and their spin correlations.

An equally important focus of this proposal is to study the gluonic structure of nuclei for the first time through the measurement of exclusive coherent ϕ meson electroproduction off a ^{4}He target in tandem with the DVCS measurement. The kinematic regime to be explored includes very low $|t|$ up to the first diffractive minimum as found in ^{4}He elastic scattering ($|t'| \simeq 0.6$ GeV^2), Q^2 up to 8 GeV^2, and x_B up to 0.3. The ϕ meson will be detected primarily through the charged K^+K^- channel, with the neutral $K_S^0 K_L^0$ channel also available through $K_S \to \pi^+\pi^-$. Differential cross-sections for ϕ electroproduction off ^{4}He will be measured for the first time.

The combination of CLAS12 and the ALERT detector provides a unique opportunity to study both the quark and gluon structure of a dense light nucleus. Coherent exclusive DVCS off ^{4}He will probe the transverse spatial distribution of quarks in the nucleus as a function of the quarks' longitudinal momentum fraction, x. In parallel, the average transverse gluon density of the ^{4}He nucleus will be extracted within a GPD framework using the measured longitudinal cross-section of coherent ϕ production. Additionally, threshold effects of ϕ production can be explored by exploiting the ALERT detector's large transverse acceptance for low $|t|$ events. This experiment will complement the previously approved experiment E12-12-007 that will study the gluon contribution to the proton structure using a very similar framework.

Contents

Introduction

Inclusive deep inelastic scattering (DIS) experiments have been instrumental in advancing our understanding of the QCD structure of nuclei and the effect of nuclear matter on the structure of hadrons. A great example is the observation by the European Muon Collaboration (EMC) of a deviation of the deep inelastic structure function of a nucleus from the sum of the structure functions of the free nucleons, the so-called EMC effect [1]. It became clear that even in a DIS process characterized by high locality of the probe-target interaction region, a different picture emerges from the nucleus other than a collection of quasi-free nucleons. On the theory side, despite decades of theoretical efforts [2, 3, 4, 5, 6] with increased sophistication, a unifying physical picture of the origin of the EMC effect is still a matter of intense debate. To reach the next level of our understanding of nuclear QCD and unravel the partonic structure of nuclei, experiments need to go beyond the inclusive measurements and focus on exclusive and semi-inclusive reactions.

Hard exclusive experiments such as Deep Virtual Compton Scattering (DVCS) and Deep Virtual Meson Production (DVMP) provide an important new probe that will allow us to discern among the different interpretations of nuclear effects on the structure of embedded nucleons in the nuclear medium. By introducing a new framework to describe both the intrinsic motion of partons and their transverse spatial structure in nuclei [4, 5, 6, 7, 8, 9]. valuable information can be obtained from the measurement of the nuclear Generalized Parton Distributions (GPDs) representing the soft matrix elements for these processes. The GPDs correspond to the coherence between quantum states of different (or same) helicity, longitudinal momentum, and transverse position. In an impact parameter space, they can be interpreted as a distribution in the transverse plane of partons carrying a certain longitudinal momentum [10, 11, 12]. A crucial feature of GPDs is the access to the transverse position of partons which, combined with their longitudinal momentum, leads to the total angular momentum of partons [13]. This information is not accessible to inclusive DIS which measures probability amplitudes in the longitudinal plane.

A high luminosity facility such as Jefferson Lab offers a unique opportunity to map out the three-dimensional quark and gluon structure of nucleons and nuclei. While most of submitted proposals to JLab Program Advisory Committee (PAC) have focused on the studies of the 3D nucleon structure considered as one of the main motivations for the JLab

12 GeV upgrade, we propose here to extend the measurements to light nuclei. While this proposal focuses on ^{4}He nucleus, we also plan to measure few deuteron GPDs[1]. Pioneering measurements of exclusive coherent DVCS off ^{4}He have been successfully conducted during the JLab 6 GeV era (E08-024) using the CLAS detector enhanced with the radial time projection chamber (RTPC) for the detection of low energy recoils and the inner calorimeter for the detection of forward high energy photons. The experiment, however covered only limited kinematic range and the results were dominated by statistical uncertainties [14].

We propose a new measurement of hard exclusive DVCS and deep virtual ϕ production off ^{4}He nuclei. The focus of this proposal is on the coherent DVCS (DVMP) channel where the scattered electron, the produced photon (the ϕ meson) and the recoil ^{4}He are all detected in the final state. The advantage of using CLAS12 is the large acceptance which will allow us to mine the data collected in this experiment for other final states as well, such as the π^0, ρ and ω mesons and other reaction channels described in the accompanying proposals of the ALERT run group[1]. The novelty of the proposed measurements is the use of a new low energy recoil tracker (ALERT) in addition to CLAS12. The ALERT detector is composed of two types of fast detectors: a stereo drift chamber for track reconstruction and an array of scintillators for particle identification. ALERT will be included in the trigger for efficient background rejection, while keeping the material budget as low as possible to detect low energy particles. This was not possible with the previous GEM based RTPC due to the long drift time.

---

[1]See the 4th proposal of the ALERT run group which summarizes additional measurements we plan to perform with no additional beam time.

Chapter 1

Physics Motivations

1.1 DVCS Measurement

A wealth of information on the QCD structure of hadrons lies in the correlations between the momentum and spatial degrees of freedom of the constituent partons. Such correlations are accessible via GPDs which, more specifically, describe the longitudinal momentum distribution of a parton located at any given position in the plane transverse to the longitudinal momentum of the fast moving nucleon. Various GPDs extracted from measurements of hard exclusive reactions with various probe helicities and target spin configurations are necessary to identify this subset of the hadronic phase-space distribution, known as the Wigner distribution. The processes which are most directly related to GPDs are DVCS and DVMP corresponding to the exclusive electroproduction of a real photon or a meson in the final state respectively, see Fig. 1.1.

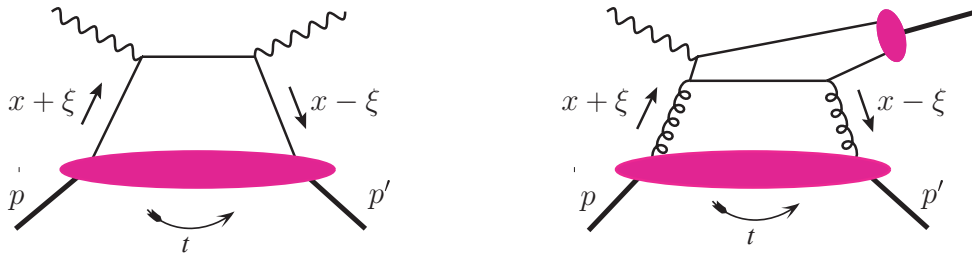Figure 1.1: Left figure: DVCS process in the handbag approximation. Right figure: DVMP diagram at the lowest order, dominated by two-gluon exchange.

The number of GPDs needed to parametrize the partonic structure of a nucleus depends on the different configurations between the spin of the nucleus and the helicity direction of the struck quark. For example, for a target of spin s, the number of chiral-even GPDs is
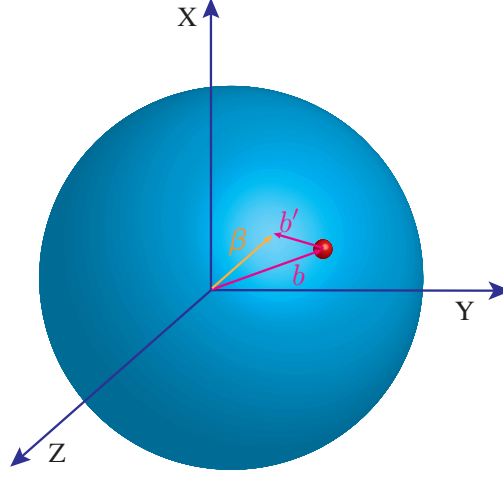
Figure 1.2: The spatial coordinates of quarks in a nucleus. See main text for definition of the variables.

equal to $(2s + 1)^2$ for each quark flavor. DVCS off spin 0 nuclear targets, such as ^{4}He, is simpler to study since only one chiral-even GPD, H_A, is present at leading twist.

The ^{4}He nucleus is a well studied few-body system in standard nuclear physics. It is characterized by a strong binding energy and relatively high nuclear core density similar to some more complex nuclei. Inclusive scattering off ^{4}He shows a large EMC effect. By measuring GPDs in nuclei, one also access transverse spatial degrees of freedom, by which one can infer space dependent nuclear modifications directly from data. In Figure 1.2, the Fourier transform of the nucleon GPDs over the momentum transfer Δ gives the transverse separation (b') between quarks in the nucleon, while the Fourier transform of the nuclear GPD gives the transverse separation (b) between quarks in the nucleus. Knowing these two separations, one can access the transverse separation ($\beta = b - b'$) between the center of momenta of nucleons in a nucleus [4]. This attractive possibility would enable us to obtain quantitative information on *e. g.* the confinement size of bound nucleons, as well as the transverse overlap areas of hadronic configurations inside the nucleus. ^{4}He nucleus provides textbook case for DVCS measurements since it has only one chiral-even GPD. Therefore, by measuring coherent exclusive DVCS, one can, in a model independent way, access the single Compton form factor and subsequently extract the transverse spatial distribution of quarks in the fast moving nucleus.

The DVCS process off nuclear targets differs from single proton scattering in that it can

occur via either the coherent or incoherent channels. In this proposal, we will be measuring the coherent channel where the target nucleus remains intact and recoils as a whole while emitting a real photon ($eA \to e'A'\gamma$). This process allows one to measure the nuclear GPDs, which contain information on the parton correlations and the nuclear forces in the target [15, 4]. We propose to measure coherent DVCS Beam Spin Asymmetries (BSA) in order to
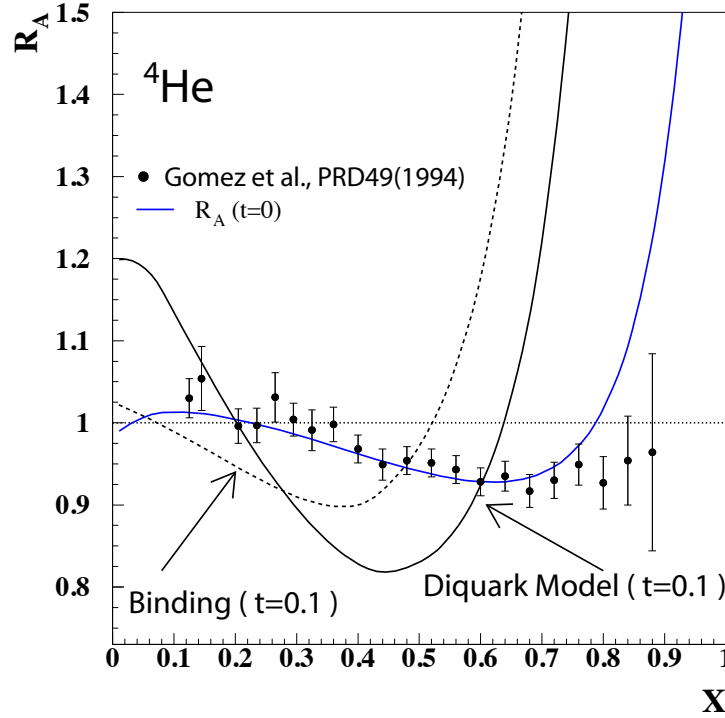

Figure 1.3: Off-forward EMC effect in ^{4}He. Theoretical predictions at $t = 0.1$ GeV^2 from both "conventional" binding models and within a diquark picture for nuclear modifications are shown. For comparison we show the effect at $t = 0$ along with the experimental data [16] (adapted from Ref. [4]).

extract in a model independent way both the real and imaginary part of the ^{4}He nuclear Compton form factor H_A. This will lead the way toward the determination of the nucleus 3D picture in terms of its basic degrees of freedom, namely valence quarks in this case. In addition, the comparison between the coherent nuclear BSA and the free proton ones will allow us to study a variety of nuclear medium effects, such as the modification of quark confinement size in the nuclear medium. In fact, configuration size modifications have been advocated as responsible for the behavior of the EMC ratio in the intermediate x_B region [17, 18, 19, 20]. The generalized EMC effect $i.e.$ the modification of the nuclear GPDs with respect to the free nucleon ones, normalized to their respective form factors was studied in Refs. [21, 22, 23, 24]. Measurements in the intermediate x_B range between 0.1 and 0.6, and for

an appropriate t-range are crucial for both establishing the role of partonic configuration sizes in nuclei, and for discerning among the several competing explanations of the EMC effect. As shown in Ref. [21], the role of partonic transverse degrees of freedom, both in momentum and coordinate space, could be important in the generalized EMC effect, thus predicting an enhancement of signals of nuclear effects with respect to the forward case (Fig. 1.3).

1.2 Deep Virtual ϕ Production Measurement

As we mentioned in the previous section, over the last two decades, there has been an increasing interest in multidimensional imaging of the structure of the nucleon. Through measurements of deep scattering in exclusive processes off the nucleon, information on Compton form factors and subsequently GPDs has been obtained successfully combining a number of published DVCS experiments with further constraints from long measured elastic scattering form factors and DIS longitudinal momentum parton distributions in the nucleon. Through these GPDs, the transverse parton density of the nucleon in the infinite momentum frame is obtained by a Fourier transform of the momentum transfer dependence leading to a transverse spatial parton density description of the nucleon.

In comparison to DVCS extraction of the quark GPDs in a nucleon, exclusive ϕ production off the nucleon provides access to gluon GPDs. The analog interpretation of this case is fairly straightforward, see Fig.1.1. In the DVCS case, the scattering is facilitated through quark exchange as denoted by the solid lines carrying the momentum fraction $x \pm \xi$. In the exclusive ϕ production case, we consider the scattering particle ϕ, which is mostly strange, interacts with the mostly up-down nucleon primarily via a two-gluon exchange. In this way, one can directly extend the quark GPD extraction in the DVCS case to the gluon GPD extraction in the ϕ production case.

A recently approved proposal using the CLAS12 detector, E12-12-007 [25], aims to extract the transverse gluon distribution of the proton and its gluonic size. In analogy, this proposal uses a very similar framework to the one discussed in E12-12-007 but focuses on the gluon GPD for a tightly bound spin zero nucleus, namely ^{4}He, thus extending the investigation of quark GPDs in a nucleus to the case of gluons. An experiment to extract gluon distributions on heavy nuclei through coherent ϕ electroproduction at the EIC has already been proposed in the most recent EIC white paper [26]. JLab 12 GeV can start such an investigation at large x where the quark distributions will be extracted initiating a full three-dimensional partonic structure investigation of a nucleus for the first time.

Gluons are the salient partners of the quarks in a nucleon as well as in a nucleus. We know they are responsible for the confinement of quarks and themselves and represent a large fraction of the energy or the mass of the nucleon. However, gluons are charge neutral and cannot be probed directly using the electromagnetic probe. For example we know the charge

distribution of ^{4}He and how to interpret it through the charge of nucleons. For instance, the diffraction minima in the measured charge distribution of ^{4}He tells us that nucleons are the appropriate degrees of freedom to consider when describing the electromagnetic properties of a nucleus. In fact we have yet to see unambiguously the elusive signature of quarks in elastic scattering off a nucleus even though we know they must be there as the building blocks of nucleons. Similarly, we do not know where the gluons are distributed in the nucleon and how they participate in the long and short-range nucleon-nucleon correlations that are responsible for the structure of the nucleus. One can ask whether in a nucleus the gluons are localized in the confined volume defined by the nucleons or spread beyond the size of the nucleons. Considering only the gluonic matter in a nucleus, a natural question arises, is a nucleus the sum of localized gluon density corresponding to that of free nucleons, or else? It would be of paramount importance to test our naive understanding of the charge neutral gluonic matter when we discuss the size of the nucleon and that of the nucleus. Among the interesting questions one might ask is whether there is evidence that the gluon transverse spatial distribution is homogenous, or does it appear to be affected by the location of the bound nucleons? In the same spirit of the discussion of quarks which was carried in the previous section, the discussion of the gluons is at least as relevant to our understanding of nuclei from basic principles.

Measuring the gluon distributions in the nucleon is an important step and will be carried by the approved experiment E12-12-007 [25]. Understanding how these distributions are modified to provide the binding and structure in a nucleus is as fascinating of a question and an integral part of our quest of using QCD to explore nuclear matter. The future electron Ion Collider will have the tools to address these questions using heavier mesons like J/Ψ and Υ. At JLab 12 GeV we can use the lighter vector mesons, namely the ϕ, to initiate this physics program and provide a glimpse into the salient features of nuclear matter.
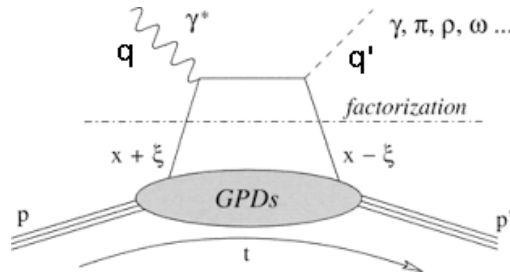
Chapter 2

Formalism and Experimental Observables

Figure 2.1: Lowest order (QCD) amplitude for the DVCS and DVMP processes, the so-called handbag diagram. q, q' represent the the four-momentum of the virtual and real photons or mesons, and p, p' are the initial and final four-momentum of the target nucleus.

GPDs are universal non-perturbative objects, entering the description of hard exclusive electroproduction processes. They are defined for each quark flavor f and gluon as matrix elements of light cone operators [27] describing the transition between the initial and final states of a hadron. The GPDs depend on two longitudinal momentum fraction variables (x, ξ) and on the momentum transfer t to the target. x is the average longitudinal momentum fraction of the parton involved in the process and ξ is the longitudinal fraction of the momentum transfer Δ, with $\Delta^2 = t = (p - p')^2$. Particularly, its perpendicular component $\Delta_\perp$ is Fourier conjugate to the transverse position of the parton in the impact parameter space. The handbag diagram in Fig. 2.1 displays a hard part which is calculable in perturbative QCD, and a soft/non-perturbative part which contains the fundamental partonic structures known as the Compton Form Factors (CFFs). The CFFs are convolution integrals containing GPDs. GPDs can also be considered as the off-forward kinematic extensions (or generalizations) of the standard Parton Distributions Functions (PDFs) from inclusive Deep

Inelastic Scattering, which are obtained in the limit of zero momentum transfer between the initial and final protons (the forward limit), with no proton spin flip. Similar to DIS, higher twist terms describe quark-gluon-quark correlations which are suppressed by powers of $1/Q$, where the final state is a meson in the case of the DVMP reaction. Experimentally, only ξ and t are measurable in the DVCS reaction. At twist-2 order, ξ can be calculated as $x_B/(2 - x_B)$. In the limit $\xi \to 0$, the Fourier transform of the GPDs in the variable Δ can be interpreted as the probability distribution of finding a parton with momentum x at a position b (the Fourier conjugate to Δ) with respect to the proton's center of momentum [28].

The spin zero of the ^{4}He target allows for a simple parametrization of its partonic structure characterized at leading twist by one chirally-even GPD H_A. In the forward limit ($t \to 0$), this GPD reduces to the usual parton densities of ^{4}He measured in DIS. The polynomiality property of GPDs leads to interesting consequences: the first Mellin moment provides an explicit link with the electromagnetic form factor F_A of the nucleus

$$\sum_f e_f \int_{-1}^{1} dx\, H_A^f(x, \xi, t) = F_A(t) \,, \tag{2.1}$$

and the second moment yields the relationship

$$\int_{-1}^{1} dx\, x\, H_A^f(x, \xi, t) = M_2^{f/A}(t) + \frac{4}{5}\xi^2 d_A^f(t) \tag{2.2}$$

which constrains the ξ-dependence of the GPDs. At $t \to 0$, the first term of the right-hand side of Eq. (2.2) is the momentum fraction of the target carried by a given quark. The second term of Eq. (2.2) is the so-called D-term which was shown to encode information about the spatial distribution of forces experienced by quarks and gluons inside hadrons [15].

From a practical point of view, we need to extract H_A from its CFFs $\mathcal{H}_A$, that appear directly in the cross section expressions. Experimentally, the DVCS reaction is indistinguishable from the Bethe-Heitler (BH) process, which is the reaction where the final photon is emitted either from the incoming or the outgoing leptons. The BH process is not sensitive to GPDs and does not carry information about the partonic structure of the hadronic target. The BH cross section is calculable from the well-known electromagnetic FFs. The DVCS amplitude is enhanced through the interference with the BH process. Figure 2.2 shows the world measurements of the ^{4}He $F_A(t)$ along with theoretical calculations. Following the ^{4}He $F_A(t)$ parametrization by R. Frosch and his collaborators [30] (valid at the small values of $-t$ which are of interest in this work), Figure 2.3 shows the calculated BH as a function of the azimuthal angle between the leptonic and the hadronic planes (ϕ), using a 6 GeV electron beam on a ^{4}He target.

The differential cross section for a longitudinally-polarized electron beam (λ) and an unpolarized ^{4}He target can be decomposed into BH, DVCS, and interference terms. Similarly
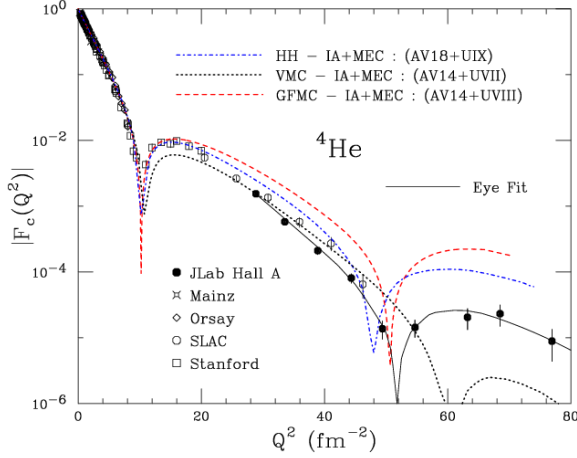
Figure 2.2: ^{4}He charge form factor measurements at Stanford, SLAC, Orsay, Mainz and JLab Hall A compared with theoretical calculations. The figure is from [29].
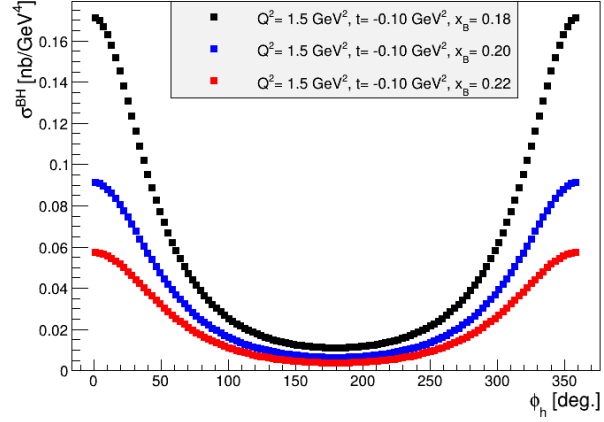

Figure 2.3: The calculated BH cross section as a function of ϕ on a ^4He target at three values of x_B and fixed values of Q^2 and t. ($t = $ - 0.1 GeV^2/c^2 corresponds to $Q^2 \approx 2.57$ fm^{-2} on figure 2.2).

to a nucleon target one can write out the azimuthal angle, ϕ, dependence for the nuclear BH, DVCS and interference terms in the cross section: each modulation in ϕ is multiplied by a structure function containing the GPDs of interest. The different contributions are written as [31],

$$|\mathcal{T}_{BH}|^2 = \frac{e^6(1+\gamma^2)^{-2}}{x_A^2 y^2 t \mathcal{P}_1(\phi)\mathcal{P}_2(\phi)} \left[c_0^{BH} + c_1^{BH}\cos(\phi) + c_2^{BH}\cos(2\phi) \right] \tag{2.3}$$

$$|\mathcal{T}_{DVCS}|^2 = \frac{e^6}{y^2 Q^2} \left[c_0^{DVCS} + \sum_{n=1}^{2} \left(c_n^{DVCS}\cos(n\phi) + \lambda s_n^{DVCS}\sin(n\phi) \right) \right] \tag{2.4}$$

$$\mathcal{I}_{BH*DVCS} = \frac{\pm e^6}{x_A y^3 t \, \mathcal{P}_1(\phi)\mathcal{P}_2(\phi)} \left[c_0^I + \sum_{n=0}^{3} \left(c_n^I\cos(n\phi) + \lambda s_n^I\sin(n\phi) \right) \right], \tag{2.5}$$

where $x_A = Q^2/(2p \cdot q) = Q^2/2M_A\nu$, M_A being the nuclear mass. The explicit expressions of the coefficients can be found in Appendix A. It is convenient to use the beam-spin asymmetry as DVCS observable because most of the experimental normalization and acceptance issues cancel out in an asymmetry ratio. The beam-spin asymmetry is measured using a longitudinally polarized lepton beam (L) on an unpolarized target (U) and defined as:

$$A_{LU} = \frac{d^5\sigma^+ - d^5\sigma^-}{d^5\sigma^+ + d^5\sigma^-}. \tag{2.6}$$

where $d^5\sigma^+ (d^5\sigma^-)$ is the DVCS differential cross section for a positive (negative) beam helicity. At leading twist, the beam-spin asymmetry (A_{LU}) with the two opposite helicities of a longitudinally-polarized electron beam (L) on a spin-zero target (U) can be written as:

$$A_{LU} \;\;=\;\; \frac{x_A(1+\varepsilon^2)^2}{y}\, s_1^{INT}\sin(\phi) \;\Big/\; \Big[\sum_{n=0}^{n=2} c_n^{BH}\cos{(n\phi)} + \qquad\qquad (2.7)$$

$$\frac{x_A^2 t(1+\varepsilon^2)^2}{Q^2} P_1(\phi)P_2(\phi)\, c_0^{DVCS} + \frac{x_A(1+\varepsilon^2)^2}{y}\sum_{n=0}^{n=1} c_n^{INT}\cos{(n\phi)} \Big].$$

where $\mathcal{P}_1(\phi)$ and $\mathcal{P}_2(\phi)$ are the Bethe-Heitler propagators. The factors: $c_{0,1,2}^{BH}$, c_0^{DVCS}, $c_{0,1}^{INT}$ and s_1^{INT} are the Fourier coefficients of the BH, the DVCS and the interference amplitudes for a spin-zero target [9, 31]. The beam-spin asymmetry (A_{LU}) can be rearranged as

$$A_{LU}(\phi) = \frac{\alpha_0(\phi)\,\Im m(\mathcal{H}_A)}{\alpha_1(\phi)+\alpha_2(\phi)\,\Re e(\mathcal{H}_A)+\alpha_3(\phi)\big(\Re e(\mathcal{H}_A)^2+\Im m(\mathcal{H}_A)^2\big)} \qquad (2.8)$$

where $\Im m(\mathcal{H}_A)$ and $\Re e(\mathcal{H}_A)$ are the imaginary and real parts of the CFF $\mathcal{H}_A$ associated to the GPD H_A. The α_i's are ϕ-dependent kinematical factors that depend on the nuclear form factor F_A and the independent variables Q^2, x_B and t. These factors are simplified as:

$$\alpha_0(\phi) \;\;=\;\; \frac{x_A(1+\varepsilon^2)^2}{y}S_{++}(1)\sin(\phi) \qquad\qquad (2.9)$$

$$\alpha_1(\phi) \;\;=\;\; c_0^{BH} + c_1^{BH}\cos(\phi) + c_2^{BH}\cos(2\phi) \qquad\qquad (2.10)$$

$$\alpha_2(\phi) \;\;=\;\; \frac{x_A(1+\varepsilon^2)^2}{y}\left(C_{++}(0)+C_{++}(1)cos(\phi)\right) \qquad\qquad (2.11)$$

$$\alpha_3(\phi) \;\;=\;\; \frac{x_A^2 t(1+\varepsilon^2)^2}{y}\mathcal{P}_1(\phi)\mathcal{P}_2(\phi)\cdot 2\frac{2-2y+y^2+\frac{\varepsilon^2}{2}y^2}{1+\varepsilon^2} \qquad\qquad (2.12)$$

Where $S_{++}(1)$, $C_{++}(0)$, and $C_{++}(1)$ are the Fourier harmonics in the leptonic tensor. Their explicit expressions can be found in Appendix A. Using the α_i factors, one can obtain in a model-independent way $\Im m(\mathcal{H}_A)$ and $\Re e(\mathcal{H}_A)$ from fitting the experimental A_{LU} as a function of ϕ for given values of Q^2, x_B and t.

Chapter 3

Experimental Overview

The study of coherent nuclear DVCS is still in its infancy due to the challenging detection of the low energy recoil nucleus. The deuterium was investigated at HERMES [32] and JLab Hall A [33], and the HERMES experiment was the only one to study heavier nuclei (^{4}He, N, Ne, Kr, and Xe) [32]. In the latter, the DVCS process was measured by identifying the scattered lepton and the real photon in the forward spectrometer. Sizable asymmetries (Fig. 3.1) have been reported in the missing mass region -1.5$< M_X <$ 1.7 GeV mass, while they generally vanish at higher masses [32]. These asymmetries are further separated
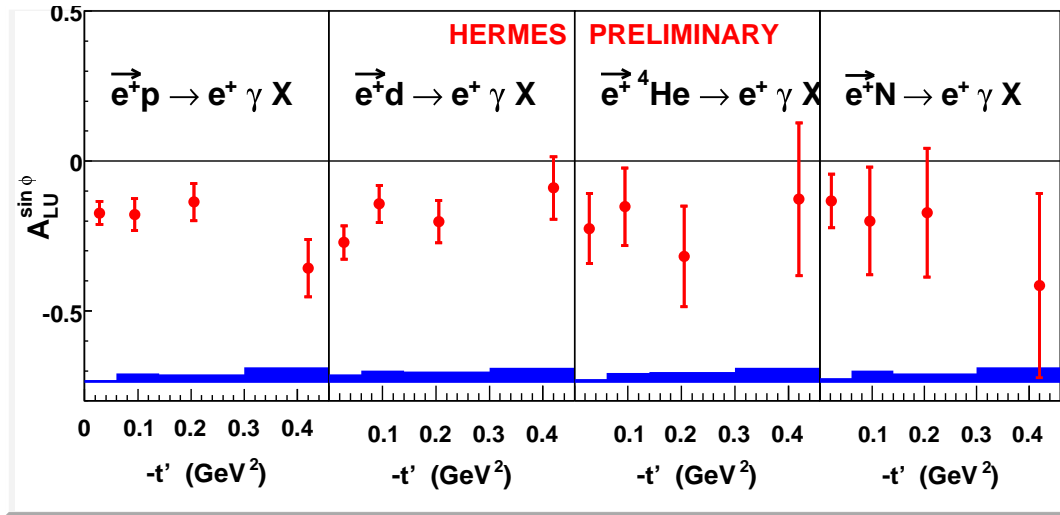

Figure 3.1: The t-dependence of the BSA on ^{1}H, ^{2}H, ^{4}He, and ^{14}N expressed in terms of the coefficient $A_{LU}^{\sin(\phi)}$ of the $\sin(\phi)$ contribution to A_{LU} [32]; we note that in the context of the HERMES fitting procedure $A_{LU}^{\sin(\phi)} \equiv A_{LU}$ i.e. the denominator of Eq. (2.8) was neglected.

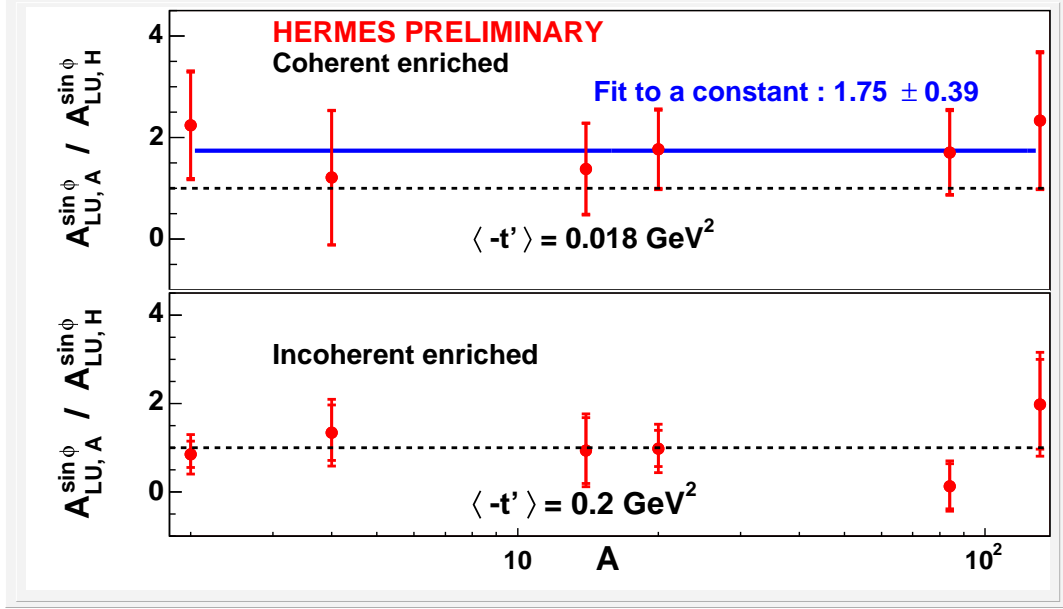into coherent and incoherent asymmetries taking advantage of the different t-dependence

Figure 3.2: The *A*-dependence of the ratio of the BSA on a nucleus to the BSA on the proton for the coherent enriched (upper panel) and incoherent enriched (lower panel) data samples [32].

of the electromagnetic form factors: in the ^{4}He case, for example, the coherent channel was found to dominate below $-t = 0.05$ GeV^2. The selection of the different regions in t (below and above) is then used to define coherent enriched and incoherent enriched data samples. The *A*-dependence of the ratio of the nuclear BSA to the proton BSA is shown on Fig. 3.2. Within the precision of the measurements, no obvious *A*-dependence of the BSA is observed: the coherent enriched ratio exhibits $\sim 2\sigma$ deviations from unity, consistent with the predictions of different models [21, 22, 34]; the incoherent enriched ratio is compatible with unity as one would expect from an impulse approximation approach [22].

The CLAS collaboration has performed a pioneering measurement (E08-024) of coherent exclusive DVCS on ^{4}He, where all the products of the reaction have been detected including the low energy recoil ^{4}He nucleus. This measurement was possible due to the high luminosity available at JLab, the large acceptance of CLAS spectrometer enhanced with the inner calorimeter (IC) and the addition of the newly built GEM based radial time projection chamber (RTPC). The IC was used to extend the photon detection to smaller angles and the RTPC was used to detect the recoil ^{4}He nucleus. The data analysis is being finalized and the review of the analysis by the CLAS collaboration is in an advanced stage [14]. The

preliminary results indicate that the collaboration has been successful in measuring the exclusive DVCS both for the coherent and incoherent channels. Figure 3.3 shows the BSA A_{LU} as a function of the azimuthal angle ϕ for different bins in Q^2 (top panel), x_B (middle panel) and $-t$ (lower panel). These asymmetries are sizable indicating a strong nuclear DVCS signal.

Figure 3.4 shows the $\sin\phi$ contribution to the coherent BSA A_{LU}, which also correspond to the coefficient $\frac{\alpha_0}{\alpha_1}$ in equation 2.8 as a function of Q^2, x_B and $-t$. It is clear the kinematic coverage and the statistics are limited, which made multidimensional binning impossible. Within the statistical uncertainties, CLAS data are roughly in good agreement with the model by Liuti et al. [4] for both the x_B and t dependencies, although a better comparison should be made with similar binning in x_B, Q^2 and t. The Liuti at al. model includes dynamical off-shellness of the nucleons taking into account medium modifications beyond the conventional Fermi motion and binding effects, which are included in their spectral function. The model also appears to be consistently giving slightly smaller asymmetries than the data, which might indicate that some of the nuclear effects are still missing in the model. The CLAS measurements also agree with the HERMES data, considering HERMES large uncertainties.

As shown in equation 2.8, one can extract both real and imaginary parts of the ^{4}He CFF $\mathcal{H}_A$ from fitting the beam-spin asymmetry signals. This extraction is fully model independent and, in contrast with the proton's GPD extraction, does not make any assumption on additional GPDs. Figure 3.5 presents the first ever experimental extraction of $\mathcal{H}_A$ from exclusive measurements as a function of Q^2, x_B, and $-t$. More theoretical effort is needed to develop predictions for $\mathcal{H}_A$. One can see a difference between the precision of the extracted real and imaginary parts, indicating the fact that the beam-spin asymmetry is mostly sensitive to the imaginary part of the CFF $\mathcal{H}_A$.

Comparing CLAS measured BSA for coherent DVCS off ^{4}He to that of the free proton will allow us to investigate the nuclear medium effects at the GPD level. For this ratio, CLAS DVCS proton data [35, 36] has been used. The results are presented in figure 3.6 along with the available theoretical calculations for this ratio. CLAS measurements show a nuclear beam-spin asymmetry enhancement compared to the free proton for all three kinematical variables. The data seem to favor the model by Guzey et al. [37], which introduces medium modification to the GPDs in a similar way than medium modified form factors. The bound nucleon form factors were calculated using the quark meson coupling model. The disagreement of the CLAS data with the Liuti et al. model [4] seems to be stronger for the t dependence of the BSA ratio.

These challenging CLAS measurements were a first step toward a promising program dedicated to nuclear QCD studies. With the 12 GeV upgrade and CLAS12 augmented with the ALERT detector, exclusive nuclear DVCS and DVMP measurements in addition to tagged EMC and tagged DVCS experiments will allow our understanding of nuclear structure and nuclear effects to reach a new frontier.
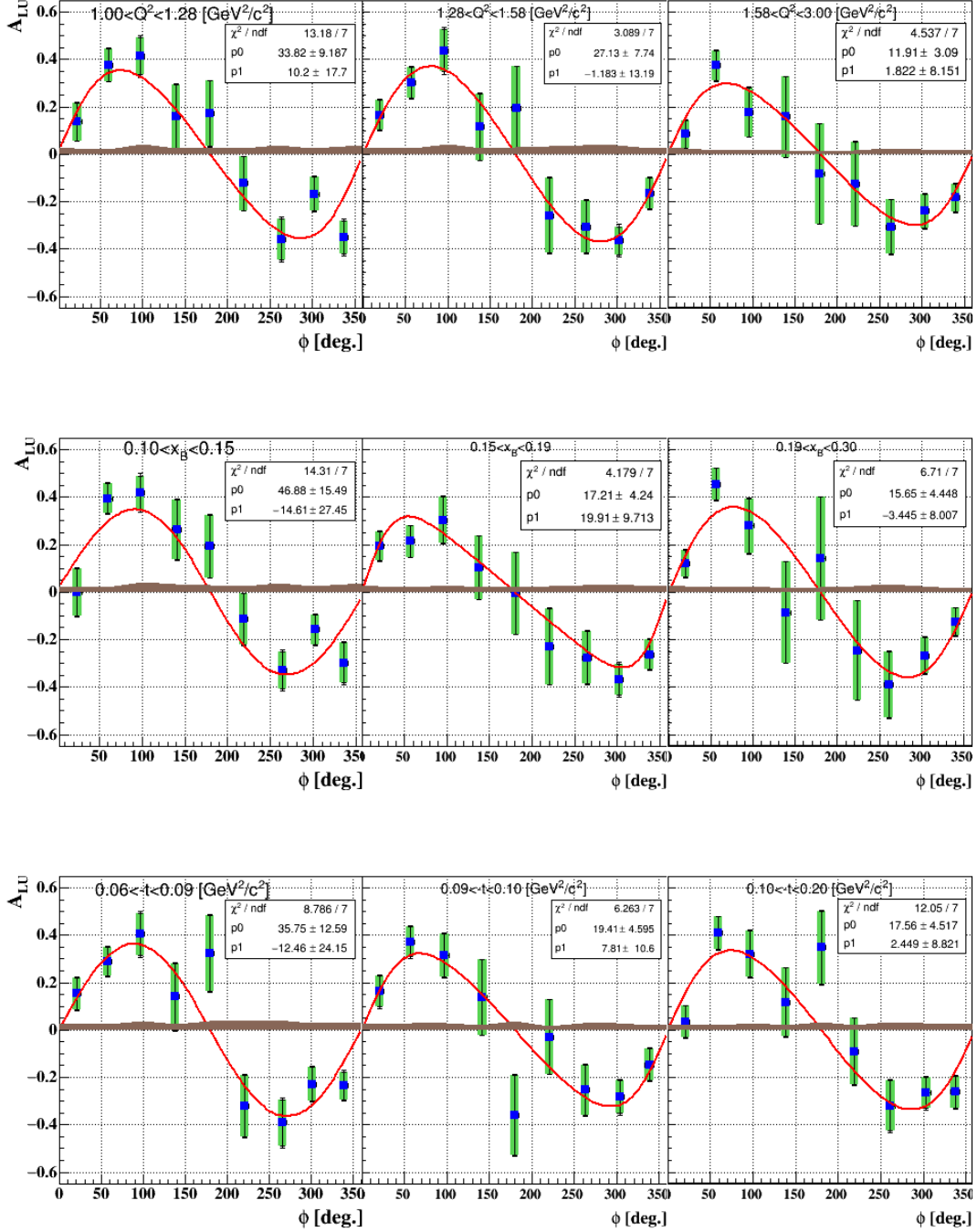
Figure 3.3: The measured coherent ^{4}He DVCS A_{LU}, from EG6 experiment, as a function of ϕ and Q^2 (top panel), x_B (middle panel), and $-t$ (bottom panel) bins [14]. The blue error bars represent the statistical and the systematic uncertainties, added quadratically, shown on the top of green error bars representing only the statistical uncertainties. The brown bands represent the full systematic uncertainties, including the normalization systematic uncertainties. The red curves represent fits in the form of equation 2.8. The parameters $p0$ and $p1$ are the imaginary and the real components of the CFF H_A resulting from fitting the experimental A_{LU}.
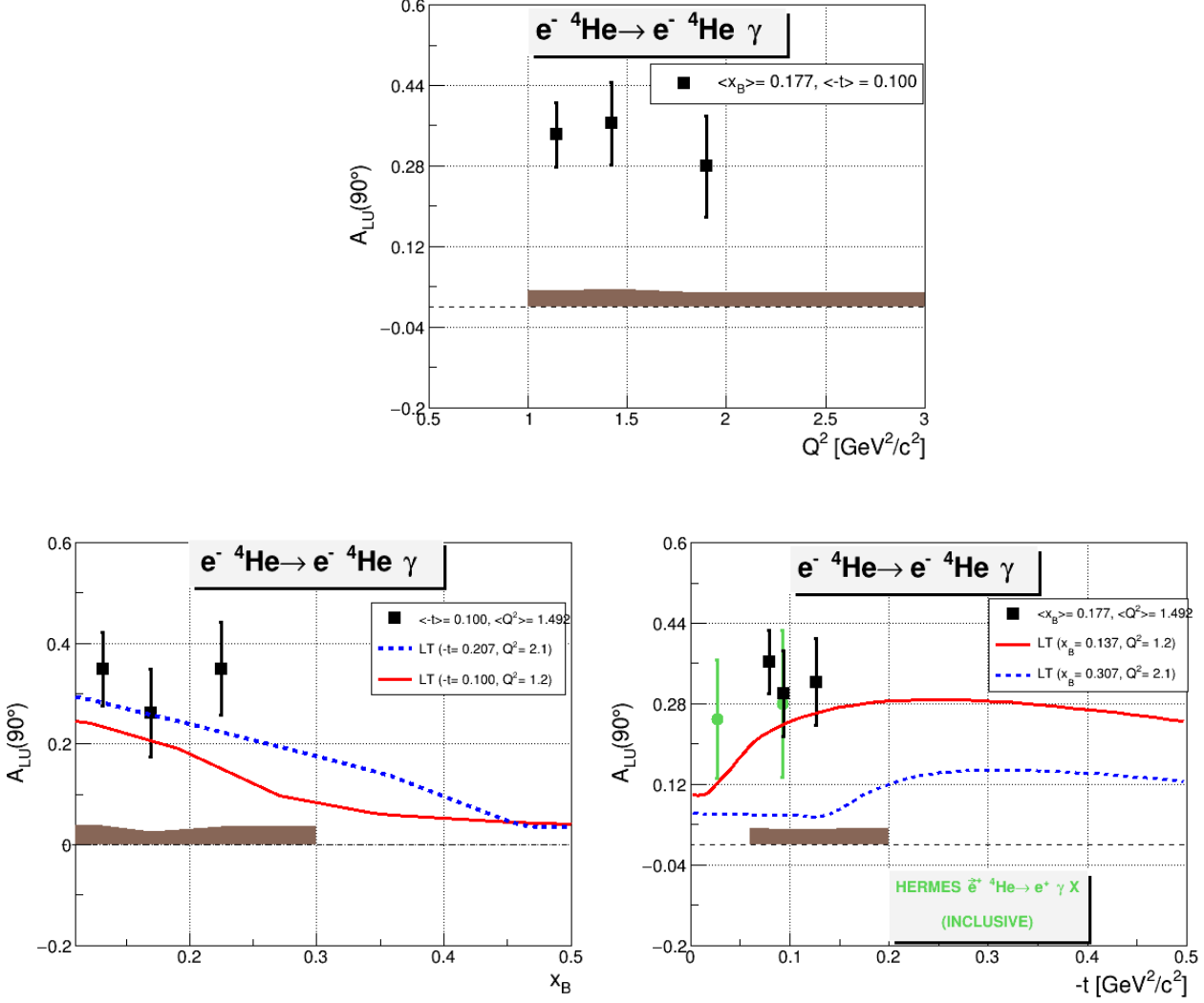
Figure 3.4: From EG6 experiment, the Q^2-dependence (top panel), the x_B and the t-dependences (bottom panel) of the fitted coherent ^{4}He DVCS A_{LU} asymmetry at $\phi = 90°$ (black squares) [14]. The curves are theoretical predictions from [4] for two values of $-t$. The green circles are the HERMES $-A_{LU}$ (a positron beam was used) inclusive measurements[38].
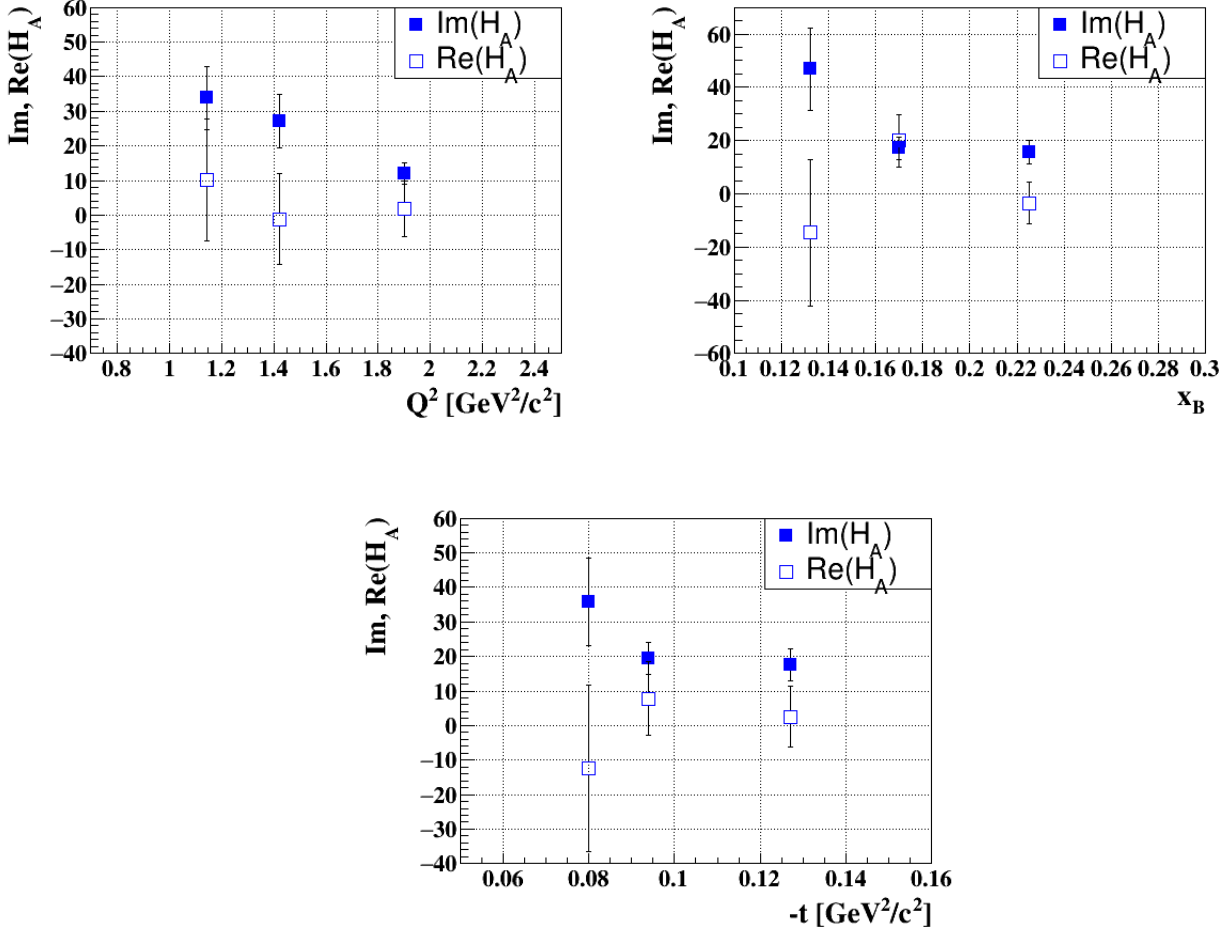
Figure 3.5: Model-independent extraction of the imaginary (full squares) and real (empty squares) parts of the ^{4}He CFF $\mathcal{H}_A$, from EG6 experiment [14], as function of Q^2, x_B (top panel), and t (bottom panel).
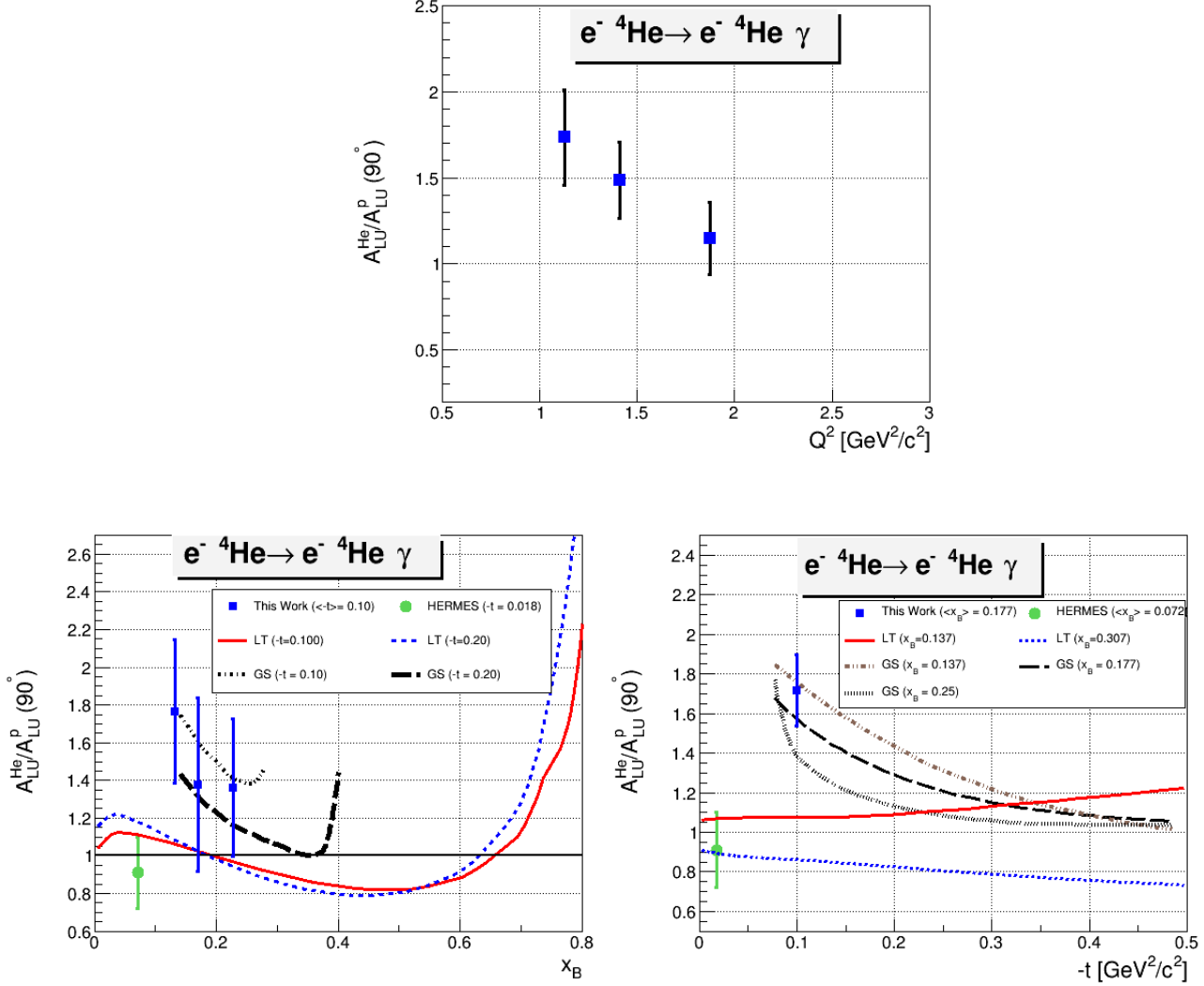
Figure 3.6: From EG6 and E1DVCS-1 experiments, the A_{LU} ratio between ^{4}He and the free proton [35, 36] at $\phi = 90°$, as a function of Q^2 (top panel), x_B and $-t$ (bottom panel). The full square represents the result of this work and the full circle is the HERMES measurement [38]. The curves are theoretical predictions from Liuti et al. [4] and Guzey et al. [37] (see legend for details).

Chapter 4

Experimental Setup

The different measurements of the ALERT run group require large kinematic coverage and the ability to identify the different nuclear species properly. The CLAS12 detector augmented by a low energy recoil detector is key for the success of such measurements. We summarize in Table 4.1 the requirements for the different experiments proposed in the run group.

This chapter will begin with a description of CLAS12 and the ALERT detector. After presenting the details of this new detector system, we will present an overview of the BoNuS12 RTPC followed by a discussion of how already approved or existing detectors do not satisfy the requirements for our run group.

Measurement	Particles detected	$p_{threshold}$	θ_{max}
Tagged EMC	p, ^{3}H, ^{3}He	As low as possible	As close to π as possible
Tagged DVCS	p, ^{3}H, ^{3}He	As low as possible	As close to π as possible
Nuclear GPDs	^{4}He	$230 < p < 400 MeV/c$	$\pi/4 < \theta < \pi/2$ rad

Table 4.1: Requirements for the detection of low momentum spectators fragments of the proposed measurements.

4.1 The CLAS12 Forward Detector

The CLAS12 detector is designed to operate with 11 GeV beam at an electron-nucleon luminosity of $\mathcal{L} = 1 \times 10^{35}$ cm^{-2}s^{-1}. The baseline configuration of the CLAS12 detector consists of the Forward Detector and the Central Detector packages [39] (see Fig. 4.1).
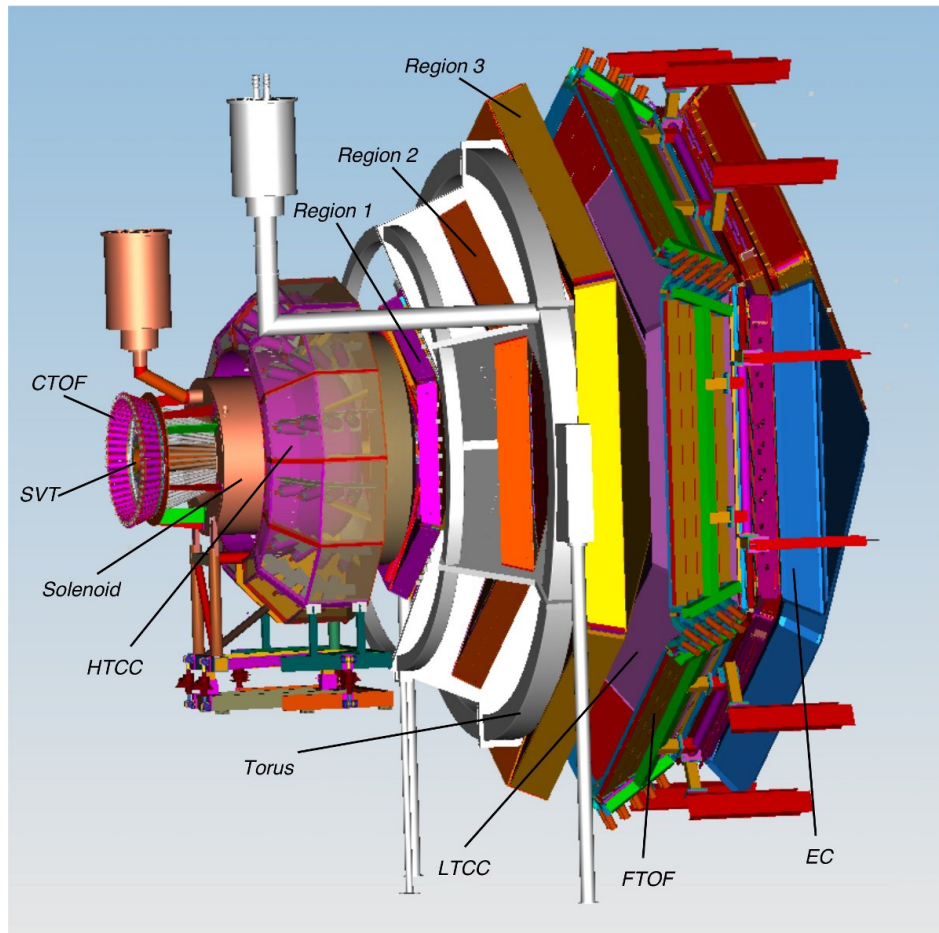
Figure 4.1: The schematic layout of the CLAS12 baseline design.

The scattered electrons will be detected in the forward detector which consists of the High Threshold Cherenkov Counters (HTCC), Drift Chambers (DC), the Low Threshold Cherenkov Counters (LTCC), the Time-of-Flight scintillators (TOF), the Forward Calorimeter and the Preshower Calorimeter. The charged particle identification in the forward detector is achieved by utilizing the combination of the HTCC, LTCC and TOF arrays with the tracking information from the Drift Chambers. The HTCC together with the Forward Calorimeter and the Preshower Calorimeter will provide a pion rejection factor of more than 2000 up to a momentum of 4.9 GeV, and a rejection factor of 100 above 4.9 GeV/c.

4.2 Design of the ALERT Detector

We propose to build a low energy recoil detector consisting of two sub-systems: a drift chamber and a scintillator hodoscope. The drift chamber will be composed of 8 layers of sense wires to provide track information while the scintillators will primarily provide particle identification. To reduce the material budget, thus pushing the energy threshold for detecting recoil particles as low as possible, the scintillator hodoscope will be placed inside the chamber, just outside of the last layer of drift wires. The good time resolution, and therefore position resolution, of the drift chamber, when coupled with the scintillators, will provide energy loss, timing, and azimuthal angle measurements for a sizable fraction of recoil particles.

The drift chamber volume will be filled with a light gas mixture (90% He and 10% C_4H_{10}) in order to not be sensitive to relativistic particles (*i.e.* electrons, gammas) and neutron backgrounds. Furthermore, a light gas mixture will increase the drift speed of electrons created during the ionization. This allows the chamber to withstand higher rates due to a shorter hit occupancy time window. The gas will likely be at atmospheric pressure but we plan to evaluate the possibility of working at a lower pressure. Based on these characteristics, the signals from this chamber and the scintillators will be used as an independent trigger, thus, reducing the DAQ trigger rate and allowing for operation at increased luminosity.

The detector must be designed to fit inside the outermost layer of Micromegas; the silicon vertex tracker and the remaining layers of Micromegas will be removed. The available space has thus an outer radius of 20 cm. A schematic layout of the preliminary design is shown in Fig. 4.2. The different detection elements are all covering about 340° of the polar angle to leave room for mechanics, and are 30 cm long with an effort made to reduce the particle energy loss through the materials. It is composed of:

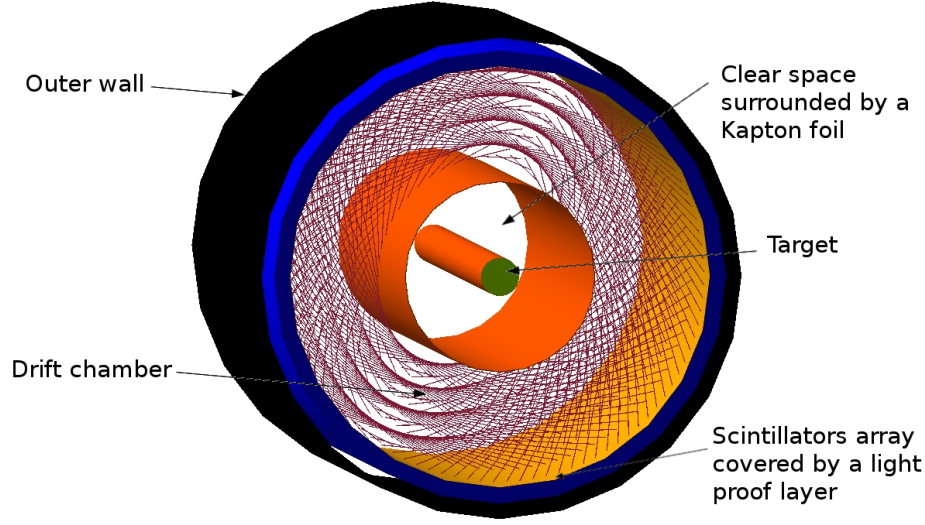- a cylindrical target, that compared to the eg6 run, is longer ($\sim$ 30 cm), wider (outer

Figure 4.2: The schematic layout of the ALERT detector design, viewed from the beam direction.

radius is 6 mm) and operating with lower pressure (~ 3 atm) in order to use a thinner target wall ($\sim 25\mu$m Kapton) [1];

- a clear space filled with helium to reduce secondary scattering from the high rate Moller electrons. Its outer radius is 30 mm;

- the drift chamber, its inner radius is 32 mm and its outer radius is 85 mm. It will detect the trajectory of the low energy nuclear recoils;

- two rings of plastic scintillators placed inside the gaseous chamber, with total thickness of roughly 20 mm.

4.2.1 The Drift Chamber

While drift chambers are very useful to cover large areas at a moderate price, huge progress has been made in terms of the ability to withstand higher rates using better electronics, shorter distance between wires and optimization of the electric field over pressure ratio. Our design is based on other chambers developed recently. For example

---

[1]During the eg6 run, the pressure of the drift gas in the RTPC was ~ 1 atm, and the pressure of the target was ~ 6.5 atm. Recent tests from S. Christo (JLab) demonstrated the feasibility of a 3 atm target with a 30 μm wall, including safety margins.

for the dimuon arm of ALICE at CERN, drift chambers with cathode planes were built in Orsay [40]. The gap between sense wires is 2.1 mm and the distance between two cathode planes is also 2.1 mm, the wires are stretched over about 1 m. Belle II is building a cylindrical drift chamber very similar to what is needed for this experiment and for which the space between wires is around 2.5 mm [41]. Finally, a drift chamber with wire gaps of 1 mm is being built for the small wheel of ATLAS at CERN [42]. The cylindrical drift chamber proposed for our experiment is 300 mm long, and we therefore considered that a 2 mm gap between wires was technically a rather conservative goal. Optimization is envisioned based on experience with prototypes.

The radial form of the detector does not allow for 90 degrees x-y wires in the chamber. Thus, the wires of each layer are at alternating angle of $\pm$ 10°, called the stereo-angle, from the axis of the drift chamber. We use stereo-angles between wires to determine the coordinate along the beam axis (z). This setting makes it possible to use a very thin forward end-plate to reduce multiple scattering of the outgoing high-energy electrons. A rough estimate of the tension due to about 2600 of 30 cm long wires is under 600 kg, which appears to be reasonable for a composite endplate.

Our drift chamber cells are composed of one sense wire made of gold plated tungsten surrounded by field wires, however the presence of the 5 T magnetic field complicates the field lines. Several cell configurations have been studied with MAGBOLTZ [43] and will be tested in a prototype (see section 4.4). For now, we decided to choose a conservative configuration as shown in Fig. 4.3. The sense wire is surrounded by 6 field wires placed equidistantly from it in a hexagonal pattern. The distance between the sense and field wires is constant and equal to 2 mm. Two adjacent cells share the field wire placed between them. The current design will have 8 layers of cells of increasing radius. The simulation code MAGBOLTZ is calculating the drift speed and drift paths of the electrons (Fig. 4.3). With a moderate electric field, the drift speed is around 10 microns/ns, the average drift time expected is thus 250 ns (over 2 mm). Assuming a conservative 10 ns time resolution, the spatial resolution is expected to be around 200 microns due to field distortions and spread of the signal.

The maximum occupancy, shown in Fig. 4.4, is expected to be of 5% for the inner most wires at 10^{35} cm^{-2}s^{-1} (including the target windows). This is the maximum available luminosity for the baseline CLAS12 and is obtained based on the physics channels depicted in Fig. 4.5, assuming an integration time of 200 ns and considering a readout wire separation of 4 mm. This amount of accidental hits does not appear to be reasonable for a good tracking quality, we therefore decided to run only at half this luminosity for our main production run. This will keep occupancy below 3%, which is a reasonable amount for a drift chamber to
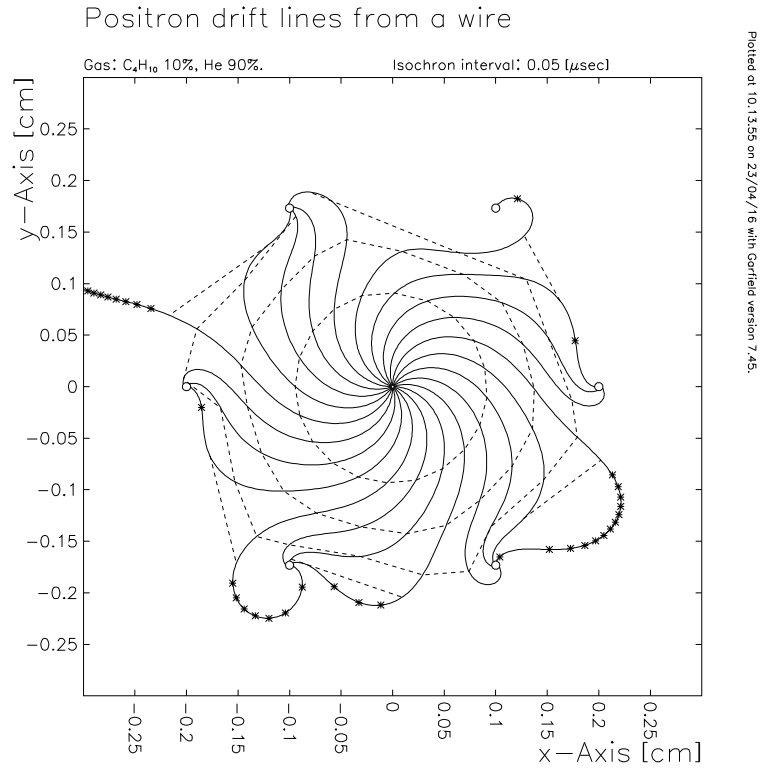
Figure 4.3: Drift lines simulated using MAGBOLTZ [43] for one sense wire (at the center) surrounded by 6 field wires. The two electric field lines leaving the cell disappear when adjusting the voltages on the wires. Dashed lines are isochrones spaced by 50 ns. This shows that the maximum drift time is about 250 ns.
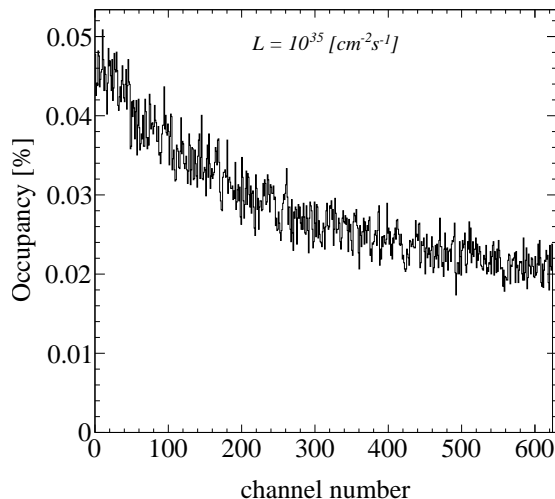
Figure 4.4: A full Geant4 simulation of the ALERT drift chamber hit occupancy at a luminosity of 10^{35} cm^{-2}s^{-1}. The channel numbering starts with the inner most wires and works outwards.

maintain high tracking efficiency. When running the coherent processes with the ^{4}He target, it is not necessary to detect the protons[2], and the rate of accidental hits can then be highly reduced by increasing the detection threshold, thus making the chamber blind to protons[3]. In this configuration, considering that our main contribution to occupancy are quasi-elastic protons, we are confident that the ALERT can work properly at 10^{35} cm^{-2}s^{-1}.

We are currently investigating two options to read out the signals from the wires. The first option would be to use the same preamplifier as the one developed for the CLAS inner calorimeter and improved for the Heavy Photon Search [44] experiment installed in Hall B. Depending on the gain in the drift chamber and the number of primary ionizations, it is possible to tune the gain of the preamplifier to adapt it to the needs of this experiment. More studies will be needed to evaluate how the gains of the chamber and the preamplifier can be tuned to ensure a noise that allows to select a threshold high enough to be blind to minimum ionizing particles. The time resolution of HPS has been shown to be few-hundred picoseconds for all crystals (Fig. 4.6) which is much better than our requirements.

The second option would be to use the electronics used by the Micromegas of CLAS12, known as the DREAM chip. Its dynamic range and time resolution seem to correspond to the need of our drift chamber. To ensure that it is the case, tests with a prototype will be

---

[2]This running condition is specific to the proposal "Partonic Structure of Light Nuclei" in the ALERT run group.

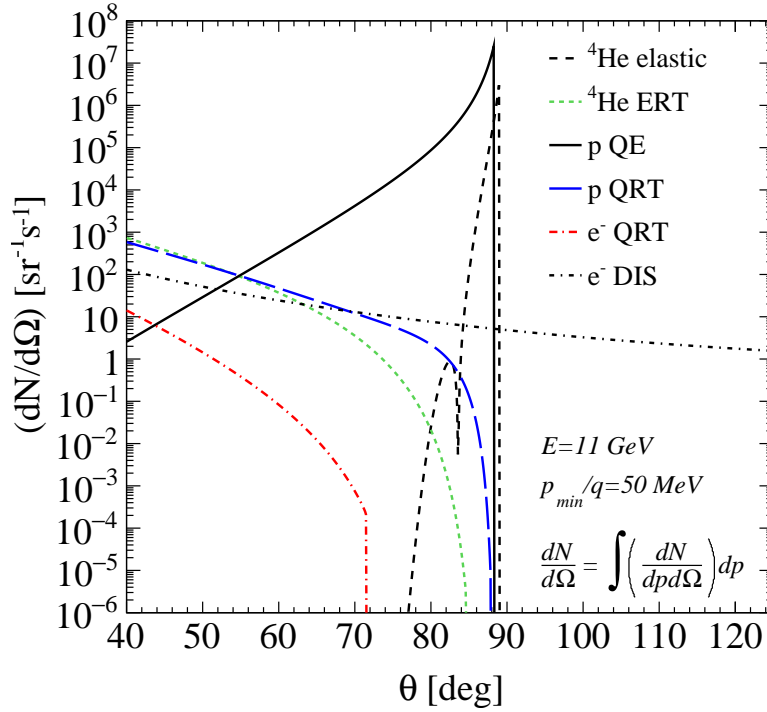[3]The CLAS *eg6* run period was using the RTPC in the same fashion.

Figure 4.5: The rates for different processes as function of angle. The quasi-elastic radiative tails (QRT), ^{4}He elastic radiative tail (ERT), and DIS contributions have been integrated over momenta starting at $p/q = 50$ MeV/c, where q is the electric charge of the particle detected.
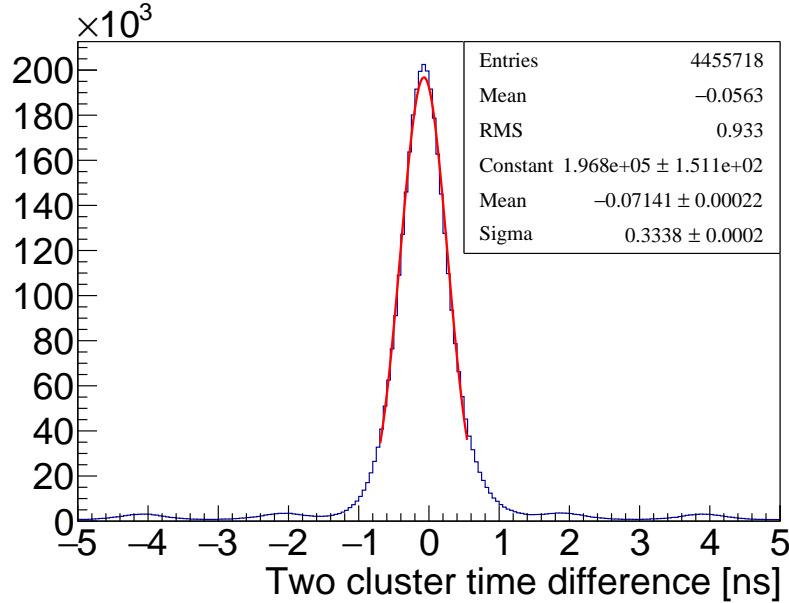
Figure 4.6: Typical time resolution of a crystal for HPS calorimeter.

performed (see section 4.4).

4.2.2 The scintillator array

The scintillator array will serve two main purposes. First, it will provide a useful complementary trigger signal because of its very fast response time, which will reduce the random background triggers. Second, it will provide particle identification, primarily through a time-of-flight measurement, but also by a measurement of the particle total energy deposited and path length in the scintillator which is important for doubly charged ions.

The length of the scintillators cannot exceed roughly 40 cm to keep the time resolution below 150 ps. It must also be segmented to match with tracks reconstructed in the drift chamber. Since ^{3}He and ^{4}He will travel at most a few mm in the scintillator for the highest anticipated momenta (~ 400 MeV/c), a layered scintillator design provides an extra handle on particle identification by checking if the range exceeded the thickness of the first scintillator layer.

The initial scintillator design consists of a thin (2 mm) inner layer of 60 bars, 30 cm in length, and 600 segmented outer scintillators (10 segments 3 cm long for each inner

bar) wrapped around the drift chamber. Each of these thin inner bars has SiPM detectors attached to both ends. A thicker outer layer (18 mm) will be further segmented along the beam axis to provide position information and maintain good time resolution.

For the outer layer, a dual ended bar design and a tile design with embedded wavelength shifting fiber readouts similar to the forward tagger's hodoscope for CLAS12 [45] were considered. After simulating these designs, it was found that the time resolution was insufficient except only for the smallest of tile designs ($15 \times 15 \times 7$ mm^3). Instead of using fibers, a SiPM will be mounted directly on the outer layer of a keystone shaped scintillator that is 30 mm in length and 18 mm thick. This design can be seen in Fig. 4.7 which shows a full Geant4 simulation of the drift chamber and scintillators. By directly mounting the SiPMs to the scintillator we collect the maximum signal in the shortest amount of time. With the large number of photons we expect, the time resolution of SiPMs will be a few tens of ps, which is well within our target.

The advantage of a dual ended readout is that the time sum is proportional to the TOF plus a constant. The improved separation of different particles can be seen in Fig. 4.8. Reconstructing the position of a hit along the length of a bar in the first layer is important for the doubly charged ions because they will not penetrate deep enough to reach the second layer of segmented scintillator.

4.3 Reconstruction

The general detection and reconstruction scheme for ALERT is as follows. Fitting a track with the drift chamber and scintillator position information yields a track radius which is proportional to the transverse momentum over the charge. Next, using the scintillator time-of-flight, the particles are separated and identified by their mass-to-charge ratio, therefore leaving a degeneracy for the deuteron and α particles.

The degeneracy between deuteron and α particles can be resolved in a few ways. The first and most simple way is to observe that an α will almost never make it to the second layer and therefore the absence (presence) of a signal would indicate the particle is an α (deuteron). Furthermore, as will be discussed below, the measured dE/dx will differ for ^{4}He and ^{2}H, therefore, taking into account energy loss in track fitting alone can provide separation. Additionally taking further advantage of the measured energy deposited in the scintillators can help separate the αs and deuterons.
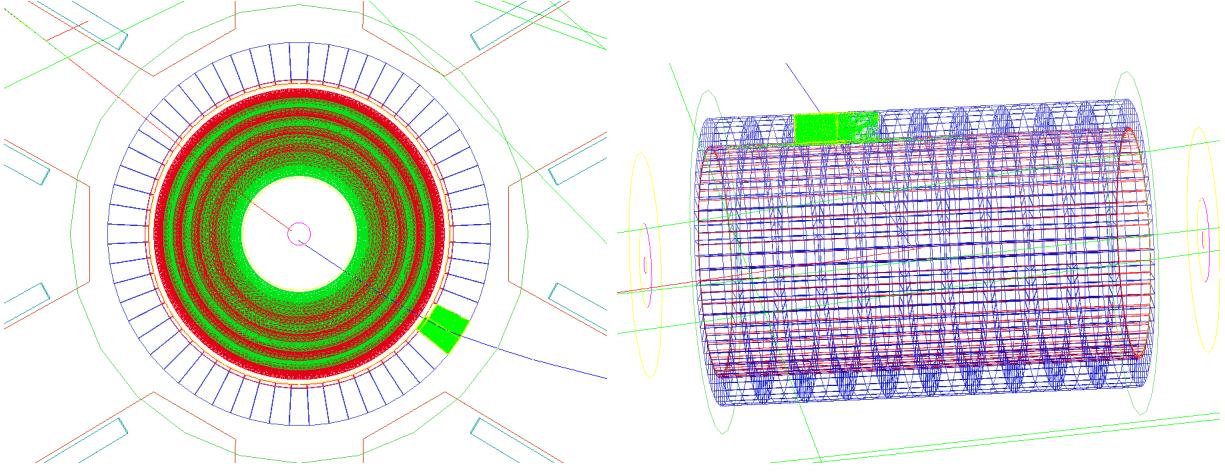
Figure 4.7: Geant4 simulation of a proton passing through the recoil drift chamber and scintillator hodoscope. The view looking downstream (left) shows the drift chamber's eight alternating layers of wires (green and red) surrounded by the two layers of scintillator (red and blue). Simulating a proton through the detector, photons (green) are produced in a few scintillators.
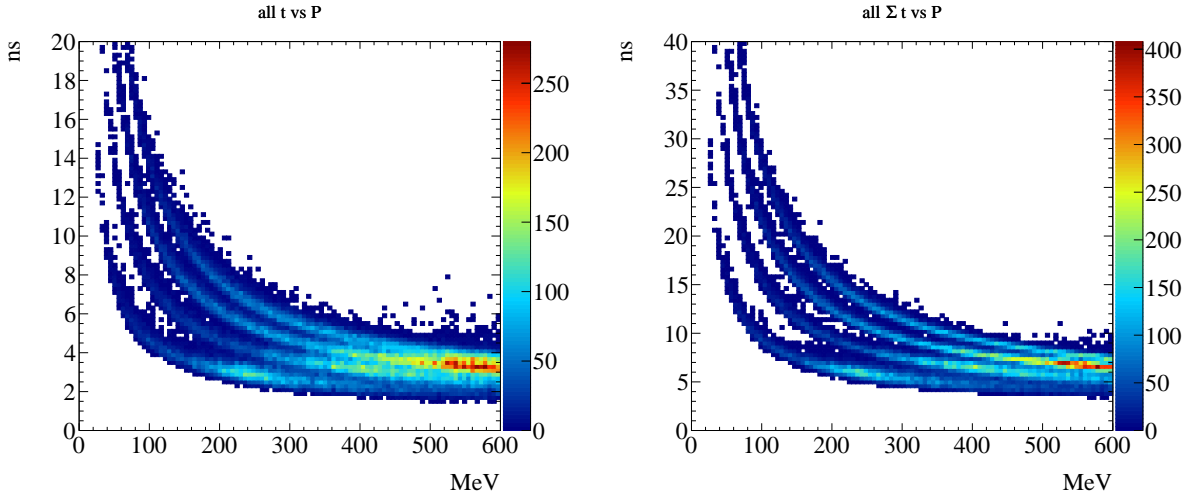

Figure 4.8: Simulated TOF for the various recoil particles vs Momentum. The TOF from just a single readout is shown on the left and the sum of the dual ended readout is shown on the right.

In the studies we present here, we do not include these latter step. However, it is important to point out that extra information is available to us in form of energy deposited in both the drift chamber and the two scintillator layers. In a full (offline) reconstruction these will give extra constraints on the identification but also on the total momentum of the detected nucleus.

As mentioned earlier, we also want a DAQ trigger, that is independent of the CLAS12 triggers. This trigger will be given by the scintillator, in coincidence with signal in a number of layers in the drift chamber. The exact number of drift chamber layers needed for the trigger will be determined during the commissioning based on actual noise and occupancy levels.

4.3.1   Track Fitting

The track obtained from a helix fitter is used to determine the coordinates of the vertex and the transverse momentum of the particle. The energy deposited in the scintillators can also be used to determine the kinetic energy of the nucleus. The feasibility and precision of the proposed vertex reconstruction and particle identification scheme were investigated with GEANT4 simulation.

The simulation of the recoil detector has been implemented with the full geometry and material specifications. It includes a 5 Tesla homogeneous solenoid field. The entire detector is filled with a very light gas mixture of He(90%) and C_4H_{10}(10%) set at atmospheric pressure to reduce the energy loss and limit the energy deposition by minimum ionizing particles.

4.3.2   Track Reconstruction and Particle Identification

In the current study all recoil species are generated with the same distributions: flat in momentum from threshold up to 40 MeV ($\sim$ 250 MeV/c) for protons and about 25 MeV for other particles; isotropic angular coverage; flat distribution in z-vertex; and a radial vertex coordinate smeared around the beam line center by a Gaussian distribution of sigma equal to the expected beam radius (0.200 mm).

With the requirement that the particle reaches the scintillator and with a 30 cm length limit, there is a smoothly varying acceptance when averaged over the z-vertex position. This is shown from simulation in Fig. 4.9 for the lightest and heaviest recoil nuclei. However, this is a conservative estimate, since it only uses tracking information. A more elaborate PID scheme may be able to accommodate a larger acceptance for lower energy recoils.
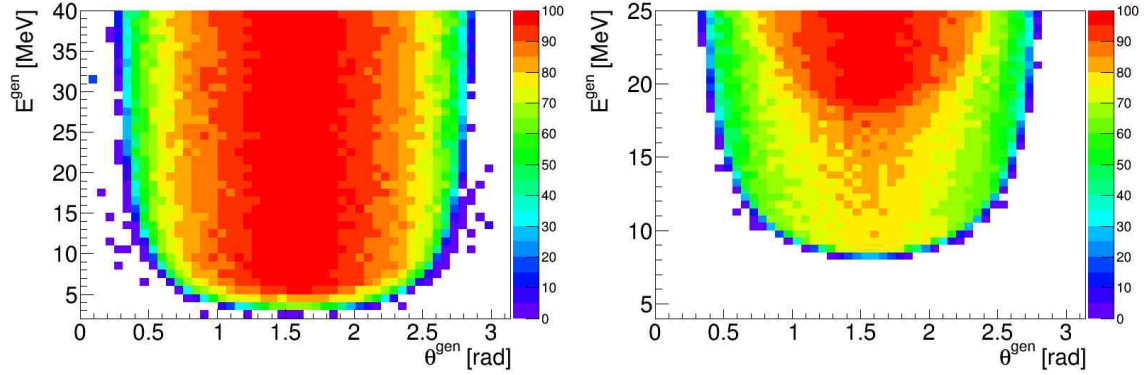
Figure 4.9: Simulated recoil detector acceptance percentage, for protons (left) and ^{4}He (right), when requiring energy deposition in the scintillators arrays.

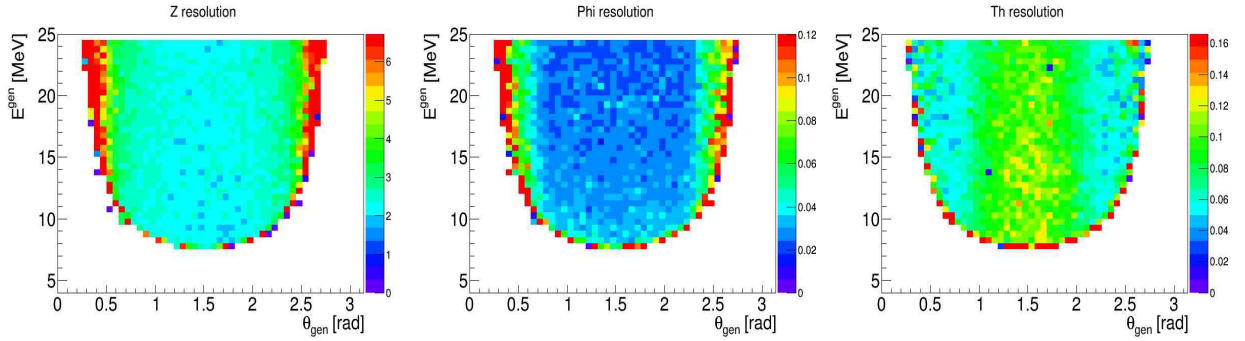Figure 4.10: Simulated resolutions, integrated over z for ^{4}He, of the z-vertex (in mm) and the polar and azimuthal angles (in rad) for the lowest energy regime when the recoil track reaches the scintillator. Note the z-axis is in units of percent.

First, the tracking capabilities of the recoil detector are investigated assuming a spatial resolutions of 200 μm for the drift chamber. The wires are strung in the z-direction with a stereo angle of 10°. For particles stopped in the scintillators, the resulting difference between generated and reconstructed variables from simulation is shown in Fig. 4.10 for ^{4}He particles. The momentum for protons and ^{4}He was also reconstructed (Fig. 4.11) from the radius of the helix assuming a uniform 5 T field. From these plots, it is clear that the resolutions required are fulfilled.

Next, the particle identification scheme is investigated. The scintillators have been designed to ensure a 150 ps time resolution. To determine the dE/dx resolution, measurements will be necessary for the scintillators and for the drift chamber as this depends on
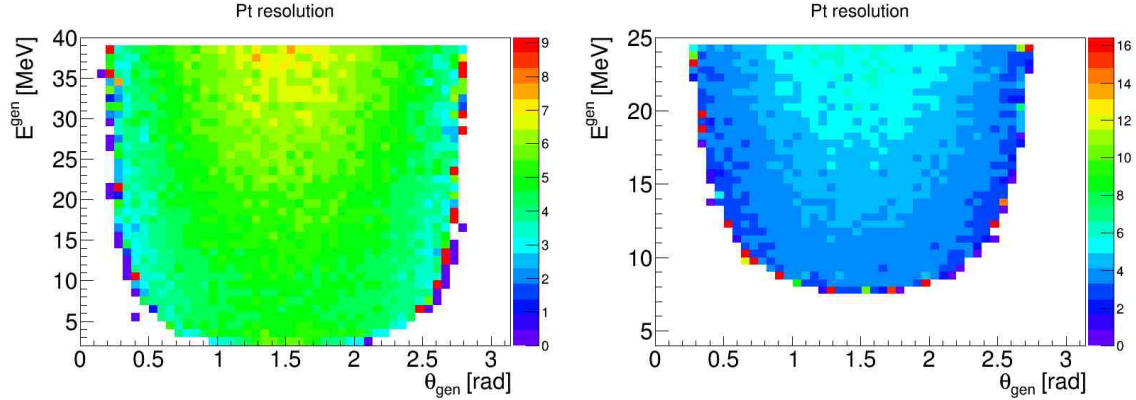
Figure 4.11: Simulated momentum resolutions for proton (left) and ^{4}He (right) integrated over z, when the recoil track reaches the scintillators array. Note the z-axis is in units of percent.

the detector layout, gas mixture, its electronics, voltages... Nevertheless, from [46], one can assume that with the 8 drift chamber measurements and the measurements in the scintillators, the energy resolution should be around 10% or better.

Under those conditions, a clean separation of three of the five nuclei is shown in Fig. 4.12 which represents the time of arrival in the scintillator as a function of the reconstructed radius in the drift chamber. ^{2}H and α are separated using dE/dx in the drift chamber and in the scintillators.

To quantify the separation power of our device, we simulated an equal quantity of each species. We obtained a particle identification efficiency of 99% for protons, 95% for ^{3}He and 98% for ^{3}H and around 90% for ^{2}H and α with equally excellent rejection factors. It is important to note that for this analysis, only the energy deposited in the scintillators was used, not the energy deposited in the drift chamber nor the path length in the scintillators, thus these number are very conservative. This analysis suggests that the proposed reconstruction and particle identification schemes for this design are quite promising. Studies, using both software and prototyping, are ongoing to determine the optimal detector parameters to minimize the detection threshold while maximizing particle identification efficiency. The resolutions presented above have been implemented in a fast Monte-Carlo used in the next section to evaluate the impact on our measurements.
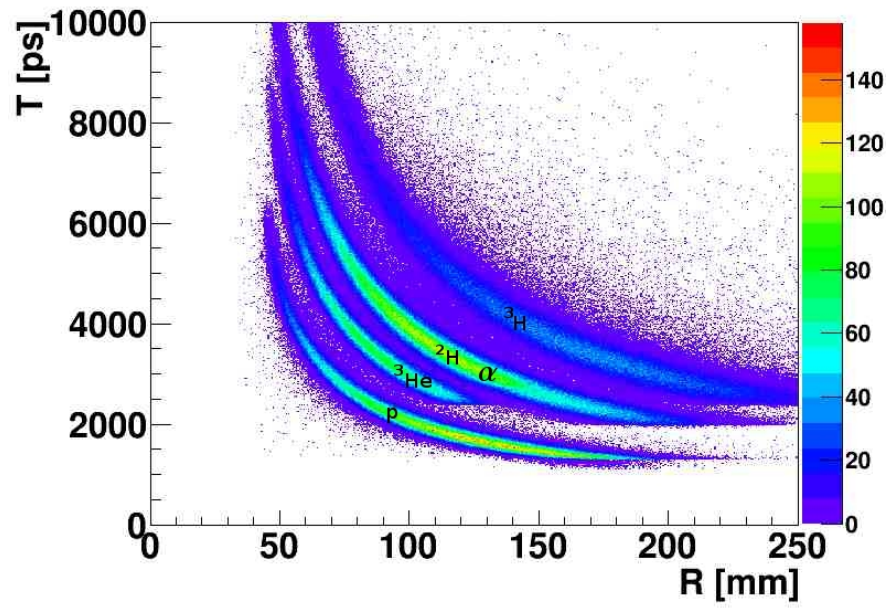
Figure 4.12: Simulated time of flight at the scintillator versus the reconstructed radius in the drift chamber. The bottom band corresponds to proton, next band is the ^{3}He nuclei, ^{2}H and α are overlapping in the third band, the uppermost band is ^{3}H. ^{2}H and α are separated using dE/dx.
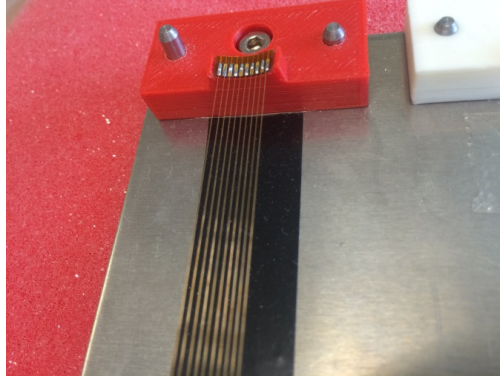
Figure 4.13: Welded wires on a curved structure with a 2 mm gap between each wire.

4.4   Drift chamber prototype

Since the design of the drift chamber presents several challenges, we decided early to start the R&D for the project and build a prototype to investigate the feasibility. This section presents the work done in Orsay to address the main questions concerning the mechanics that needed to be answered:

- Can we build a stereo drift chamber with a 2 mm gap between wires?

- Can we design a frame that can be quickly changed in case of a broken wire?

- Can the forward structure be both light to reduce the multiple scattering and rigid enough to support the tension due to the wires?

For the first question, small plastic structures realized with a 3D printer were tested and wires welded on it, as shown in Fig. 4.13. This demonstrated our ability to weld wires with a 2 mm gap on a curved structure.

To limit issues related to broken wires, we opted for a modular detector made of identical sectors. Each sector covers 20° of the azimuthal angle (Fig. 4.14) and can be rotated around the beam axis to be separated from the other sectors. This rotation is possible due to the absence of one sector, leaving a 20° dead angle. Then, if a wire breaks, its sector can be removed independently and replaced by a spare. Plastic and metallic prototype sectors were made with 3D printers to test the assembling procedure and we have started the construction of a full size prototype of one sector.

The shape of each sector is constrained by the position of the wires. It has a triangular shape on one side and due to the stereo angle, the other side looks like a pine tree with
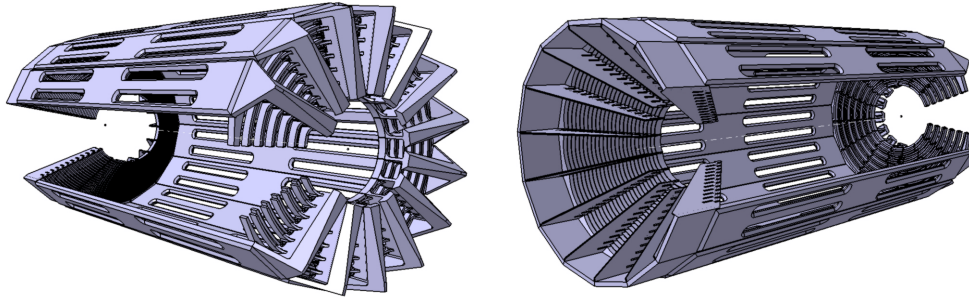
Figure 4.14: Upstream (left) and downstream (right) ends of the prototype detector in CAD with all the sectors included.

branches alternatively going left and right from a central trunk (Fig. 4.15).

The last question about the material used to build the structure will be studied in details with future prototypes. Nevertheless, current design plans are to use carbon in place of the aluminum in the forward region and titanium for the backward structure. The prototype was designed to check the mechanical requirements summarized above but also to verify the different cell configurations, and to test the DREAM electronics (time resolution, active range, noise). Since a total of five sectors have been build for tests, this will allow us to check that the elements can be properly positioned relatively to each other and one sector will be completely equipped with wires to be tested with a cosmic test bench and an α source.

4.5 Other options for a Low Energy Recoil Detector

We explored other available solutions for the low-energy recoil tracker (ALERT) with adequate momentum and spatial resolution, and good particle identification for recoiling light nuclei (p, ^{3}H and ^{3}He). After investigating the feasibility of the proposed measurements using the CLAS12 Central Detector and the BoNuS Detector [47, 48], we concluded that we needed to build a dedicated detector. We summarize in the following the facts that led us to this conclusion.

4.5.1 Central Detector

The CLAS12 Central Detector [39] is designed to detect various charged particles over a wide momentum and angular range. The main detector package includes:

- Solenoid Magnet: provides a central longitudinal magnetic field up to 5 Tesla, serves to curl emitted low energy Møller electrons and determine particle momenta through
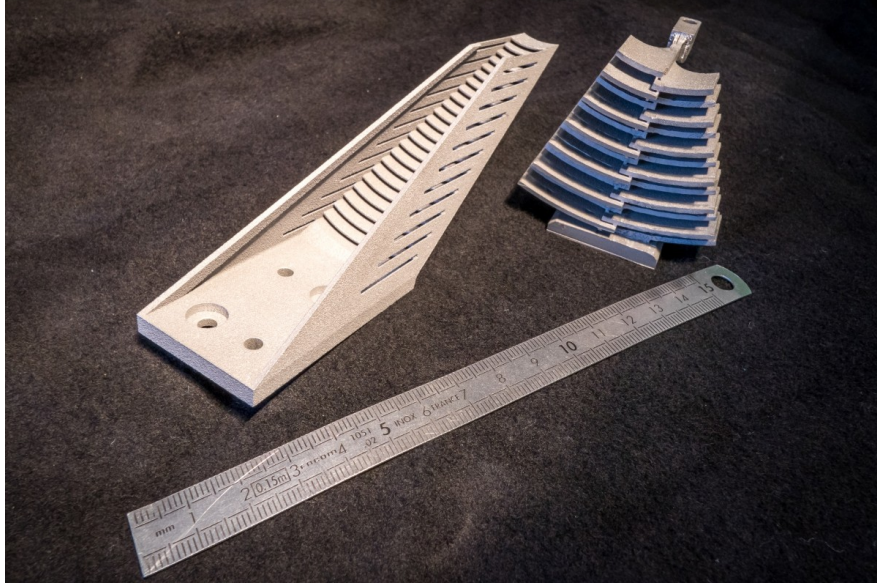
Figure 4.15: Mechanics of one sector for the prototype made with 3D printer.

tracking.

- Central Tracker: consists of 3 layers of silicon strips and 3 layers of Micromegas. The thickness of a single silicon layer is 300μm.

- Central Time-of-Flight: an array of scintillator paddles with a cylindrical geometry of radius 26 cm and length 50 cm; the thickness of the detector is 2 cm with designed timing resolution of $\sigma_t = 50$ ps, used to separate pions and protons up to 1.2 GeV/c.

The current design, however, is not optimal for low energy particles ($p < 300$ MeV/c) due to the energy loss in the first 2 silicon strip layers. The momentum detection threshold is ~ 200 MeV/c for protons, ~ 350 MeV/c for deuterons and even higher for ^{3}H and ^{3}He. These values are significantly too large for our proposed measurements, which makes the CLAS12 central detector not suitable for our measurements.

4.5.2 BoNuS12 Radial Time Projection Chamber

The original BoNuS detector was built for Hall B experiment E03-012 to study neutron structure at high x_B by scattering electrons off an almost on-shell neutron inside deuteron. The purpose of the detector was to tag the low energy recoil protons ($p > 60$ MeV/c). The key component for detecting the slow protons was the Radial Time Projection Chamber (RTPC) based on Gas Electron Multipliers (GEM). A later run period (eg6) used a ^{4}He gas

Detectors	RTPC	New Tracker
Drift region radius	4 cm	5 cm
Longitudinal length	~ 40 cm	~ 40 cm
Gas mixture	80% helium/20% DME	90% helium/10% isobutane
Azimuthal coverage	$360°$	$340°$
Momentum range	70-250 MeV/c protons	70-250 MeV/c protons
Transverse mom. resolution	10% for 100 MeV/c protons	10% for 100 MeV/c protons
z resolution	3 mm	3 mm
Solenoidal field	~ 5 T	~ 5 T
ID all light nuclei	No	Yes
Trigger	can not be included	can be included

Table 4.2: Comparison between the RTPC (left column) and the new tracker (right column).

target and a newly built and improved RTPC to detect recoiling α particles in coherent DVCS scattering. The major improvements of the eg6 RTPC were full cylindrical coverage and a higher data taking rate.

The approved 12 GeV BoNuS (BoNuS12) proposal is planning to use a similar device with some upgrades. The target gas cell length will be doubled, and the new RTPC will be longer as well, leading to a doubling in luminosity and an increased acceptance. Taking advantage of the larger bore (~ 700 mm) of the 5 Tesla solenoid magnet, the maximum radial drift length will be increased from the present 3 cm to 4 cm, improving the momentum resolution by 50% [48] and extending the momentum coverage. The main features of the proposed BoNuS12 detector are summarized in Table 4.2.

In principle, particle identification can be obtained from the RTPC through the energy loss dE/dx in the detector as a function of the particle momentum (see Fig. 4.16). However, with such a small difference between ^{3}H and ^{3}He, it is nearly impossible to discriminate between them on an event by event basis because of the intrinsic width of the dE/dx distributions. This feature is not problematic when using deuterium target, but makes the RTPC no longer a viable option for our tagged EMC and tagged DVCS measurements which require a ^{4}He target and the detection of ^{4}He, ^{3}He, ^{3}H, deuterons and protons.

Another issue with the RTPC is its slow response time due to the long drift time ($\sim 5\mu$s). If a fast recoil detector could be included in the trigger it would have a significant impact on the background rejection. Indeed, in about 90% DIS on deuteron or helium the spectator fragments have too low energy or too small angle with the beam line to get out of the target to be detected. Since the data acquisition speed was the main
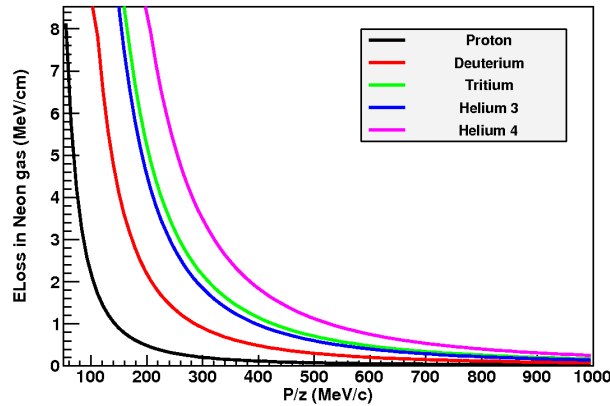
Figure 4.16: Calculation of energy loss in Neon gas as a function of the particle momentum divided by its charge for different nuclei.

limiting factor for both BoNuS and eg6 runs in CLAS, including the recoil detector in the trigger would allow us to run at higher luminosities. Indeed events without a hit in the recoil detector would not be recorded and this will significantly reduce the trigger's frequency.

4.5.3 Summary

As explained in the previous sections, the threshold of the CLAS12 inner tracker is clearly too high to be used for our measurements. On the other hand, the recoil detector planned for BoNuS12, a RTPC, is not suitable due to its inability to distinguish all kind of particles we need to measure. Moreover, as the RTPC cannot be efficiently included in the trigger, a lot of background events are sent to the readout electronics, which will cause its saturation and limit the maximum luminosity the detector can handle. Therefore, we propose to use A Low Energy Recoil Tracker (ALERT) based on a new detector design, described in the previous sections, that would provide good timing and energy loss information and a total energy measurement for each track. The fast timing will allow a tight time coincidence with CLAS12, thereby reducing the background that was encountered in previous RTPC detectors. The recoil detector can be included in the data acquisition trigger, which will significantly reduce triggering on events from the target windows, which are outside the acceptance and events with recoil too slow to exit the target.

Finally, the use of time of flight and dE/dx measurements will provide improved particle identification for the recoiling nuclei without ambiguity for ^{3}H and ^{3}He identification. The features and requirements for this new detector are compared with the current RTPC design

for BoNuS12 in Table 4.2. The transverse momentum and z resolution are chosen following the BoNuS specifications.

4.6   Technical contributions from the research groups

This effort is led by four research groups, Argonne National Lab (ANL), Institut de Physique Nucléaire d'Orsay (IPNO), Jefferson Lab and Temple University (TU).

Jefferson Lab is the host institution. ANL, IPNO and TU have all contributed technically to CLAS12. ANL was involved in the construction of the high-threshold Cherenkov counters (HTCC) for CLAS12. ANL has a memorandum of understanding (MOU) with JLab on taking responsibility for the HTCC light collection system including testing the photomultipliers and the magnetic shielding. For the RICH detector for CLAS12, ANL developed full GEANT-4 simulations in addition to the tracking software. ANL also developed the mechanical design of the detector support elements and entrance and exit windows in addition to the front-end electronics cooling system. IPNO took full responsibility for the design and construction of CLAS12 neutron detector (CND). The CND was successfully delivered to Jefferson Lab. TU played an important role in the refurbishment of the low threshold Cherenkov counters (LTCC), which was completed recently. All 216 photomultipliers have been coated with wavelength shifting material (p-Terphenyl) at Temple University, which resulted in a significant increase in the number of photoelectrons response.

The three institutions have already shown strong technical commitment to JLab 12 GeV upgrade, with a focus on CLAS12 and this proposal is a continuation of that commitment.

4.6.1   Argonne National Laboratory and Temple University

The ANL medium energy group is responsible for the ALERT scintillator system, including scintillation material, light collection device and electronics. First results of simulations have led to the design proposed here. This work will continue to integrate the scintillator system with the wire chamber. ANL will collaborate closely with Temple University to test the light detection system. Both institutions will be responsible to assemble and test the detector.

4.6.2   Institut de Physique Nucléaire d'Orsay

The Institut de Physique Nucléaire d'Orsay is responsible for the wire chamber and the mechanical structure of the detector design and construction. As shown in the proposal,

this work has already started as part of a wider R&D program focused on nuclear fragments detection with light wire chambers. A first prototype is being built to test different cell forms, wire material, wire thickness, pressure, etc. This experience will lead to a complete design of the ALERT detector integrating the scintillator built at ANL, the gas distribution system and the electronic connections. The funding already secured for this program should allow for the construction of these mechanical parts and the wire chamber itself.

Funding is also available, in partnership with *CEA Saclay*, to test the use of the DREAM front-end chip for our wire chamber. Further tests are planned to adapt the electronics to the ALERT chamber or test other chips. This chip will be used for the CLAS Micromegas, so we expect its integration to be straightforward when the ALERT run group will need it.

4.6.3 Jefferson Laboratory

We expect Jefferson Laboratory to help with the settings of the beam line. In particular, the maximum beam current will be around 500 nA for the run at 10^{35} cm^{-2}s^{-1}, which is not common for Hall-B. We also expect JLab to design and build the target for the experiment as it will be a very similar target as the ones build for CLAS Bonus and eg6 run.

We also expect Jefferson Laboratory to provide assistance in the detector installation in the Hall and to connect the electronics of ALERT to the acquisition and trigger systems of CLAS12 in addition to slow controls.

Chapter 5

Proposed Measurements

The analysis procedures for coherent DVCS and ϕ electroproduction off ^{4}He are described in this chapter. For DVCS, the scattered electron, the real photon and the recoiling ^{4}He nucleus will all be detected. For coherent ϕ production, we require the detection of the scattered electron, the recoiling ^{4}He nucleus along with either a kaon pair for the identification of the ϕ meson through its invariant mass or a single kaon, and in that case, the missing kaon will be reconstructed through missing momentum and energy.

5.1   Exclusive Coherent DVCS

DCVS is the hard exclusive production of a real photon in lepton scattering. For coherent production, we have

$$e(\mathbf{P}_e) + {}^4He(\mathbf{P}_{^4He}) \rightarrow e(\mathbf{P}'_e) + {}^4He(\mathbf{P}'_{^4He}) + \gamma(\mathbf{P}_\gamma) \tag{5.1}$$

where $\mathbf{P}_e(\mathbf{P}'_e)$ is the four-momentum of the incoming (outgoing) electron. $\mathbf{P}_{\gamma*} = \mathbf{P}_e - \mathbf{P}'_e$ is the four-momentum of the virtual photon and $\mathbf{P}_{^4He}(\mathbf{P}'_{^4He})$ is the four-momentum ^{4}He nucleus in the initial (final) state. The photon virtuality is $Q^2 = 4EE'\sin^2(\theta/2)$, where E and E' are the energy of the incoming and outgoing electron respectively. The four-momentum transfer to the nucleus is:

$$t = (\mathbf{P}_{^4He} - \mathbf{P}'_{^4He})^2 = (\mathbf{P}_{\gamma*} - \mathbf{P}_\gamma)^2. \tag{5.2}$$

Other variables of interest are ϕ the angle between the lepton scattering angle and photon production plane, $x_B = \dfrac{Q^2}{2M_p\nu}$ and $x_A = \dfrac{M_p \cdot x_B}{M_{^4He}}$, where $M_p(M_{^4He})$ is the proton (^4He) mass and $\nu = E - E'$ is the energy of the virtual photon. The kinematical cuts on the detected electron are:

- $Q^2 > 1$ GeV^2: to ensure that the interaction occurs at the partonic level and the

applicability of factorization in the DVCS handbag diagram.

- $-t > -t_{min}$: the transferred momentum squared to the recoil ^4He has to be greater than a minimum value defined by the kinematics of the beam and the scattered electron as:

$$t_{min} = -Q^2 \frac{2(1 - x_A)(1 - \sqrt{1 + \varepsilon^2}) + \varepsilon^2}{4x_A(1 - x_A) + \varepsilon^2}, \tag{5.3}$$

where $\varepsilon^2 = \dfrac{4M_{^4He}^2 x_A^2}{Q^2}$.

For all events, the scattered electron and the real photon will be detected in CLAS12 spectrometer while the recoiling ^{4}He nucleus will be detected in the ALERT detector. For both CLAS12 and ALERT, we use a FastMC package based on GEANT4 to simulate detector's acceptance. The different CLAS12 detector's resolutions were taken from CLAS12 fastMC. While for ALERT, we used parametrization of the resolutions obtained from the GEANT4 simulations described in section 4.3.

Figure 5.1 shows the correlations between Q^2, x_B and $-t$ variables which are determined by the acceptance of CLAS12 for electrons and ALERT for the recoiling ^{4}He nuclei. Figure 5.2 shows the correlation between the azimuthal angle ϕ and the polar angle θ in the laboratory frame for all detected particles from the coherent DVCS channel. The electron's ϕ versus θ distribution show the six CLAS12 sectors. Figure 5.3 presents the resolutions for the kinematic variables Q^2, x_B, t and ϕ.

We define the additional four-vectors:

$$\begin{aligned}
\mathbf{P}_X^{e^4He\gamma} &= \mathbf{P}_{\gamma^*} + \mathbf{P}_{^4He} - (\mathbf{P}_\gamma + \mathbf{P'}_{^4He}) & (5.4) \\
\mathbf{P}_X^{e^4He} &= \mathbf{P}_{\gamma^*} + \mathbf{P}_{^4He} - \mathbf{P'}_{^4He} & (5.5) \\
\mathbf{P}_X^{e\gamma} &= \mathbf{P}_{\gamma^*} + \mathbf{P}_{^4He} - \mathbf{P}_\gamma & (5.6)
\end{aligned}$$

In order to access the beam spin asymmetry, one need to identify exclusive DVCS-BH events. To ensure exclusivity, only events with a good electron, one real photon and a recoiling ^{4}He are selected as coherent events. To reduce even more the contribution of non-exclusive events, the following kinematical cuts have to be applied:

- For exclusive coherent DVCS, the virtual photon, the emitted real photon and the recoil helium have to be coplanar. The coplanarity angle ($\Delta\phi$) defined as the difference in angle between these two planes: the first defined by the virtual photon and the recoiling ^{4}He and the second defined by the real photon and the virtual one.

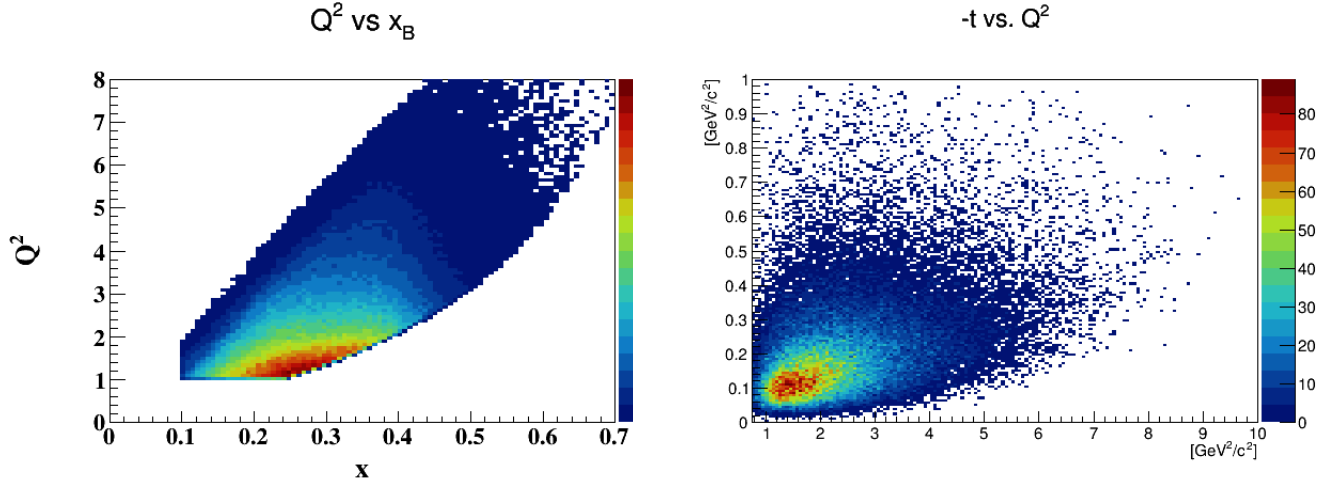Figure 5.1: Left: correlation between Q^2 and x_B. Right: correlation between $-t$ and Q^2 for coherent DVCS off ^{4}He.

- Missing energy, mass and transverse momentum ($p_X^T = \sqrt{(p_X^x)^2 + (p_X^y)^2}$) cuts on $\mathbf{P}_X^{e^4He\gamma}$.

- Missing mass cuts on the e^4HeX and $e\gamma X$ systems, which are defined as $(\mathbf{P}_X^{e^4He})^2$ and $(\mathbf{P}_X^{e\gamma})^2$ respectively.

- Cone angle cut between the measured real photon and the missing particle in the e^4HeX configuration. It is defined as:

$$\theta(\gamma, e^4HeX) = cos^{-1}\left(\frac{\overrightarrow{\mathbf{P}}_\gamma \cdot \overrightarrow{\mathbf{P}}_X^{e^4He}}{|\overrightarrow{\mathbf{P}}_\gamma||\overrightarrow{\mathbf{P}}_X^{e^4He}|}\right). \tag{5.7}$$

Even with all the previously presented exclusive cuts, the selected events are not all true DVCS events. In our kinematic region, the main contamination comes from the exclusive electroproduction of π^0 ($e^4He \rightarrow e^4He\pi^0 \rightarrow e^4He\gamma\gamma$), in which one of the two photons from the π^0 decay passes the requirements for the DVCS events. These events can however be subtracted to obtain the true number of DVCS events based on the experimentally measured number of $e^4He\pi^0$ events.

Figure 5.4 illustrates the contributions of non-exclusive (π^0) events to the coherent DVCS data sample. The number of simulated π^0 events is three times the number of the simulated single photon production events. The dependencies of the contamination from π^0 versus the exclusive distributions are shown in different panels of figure 5.4. The black
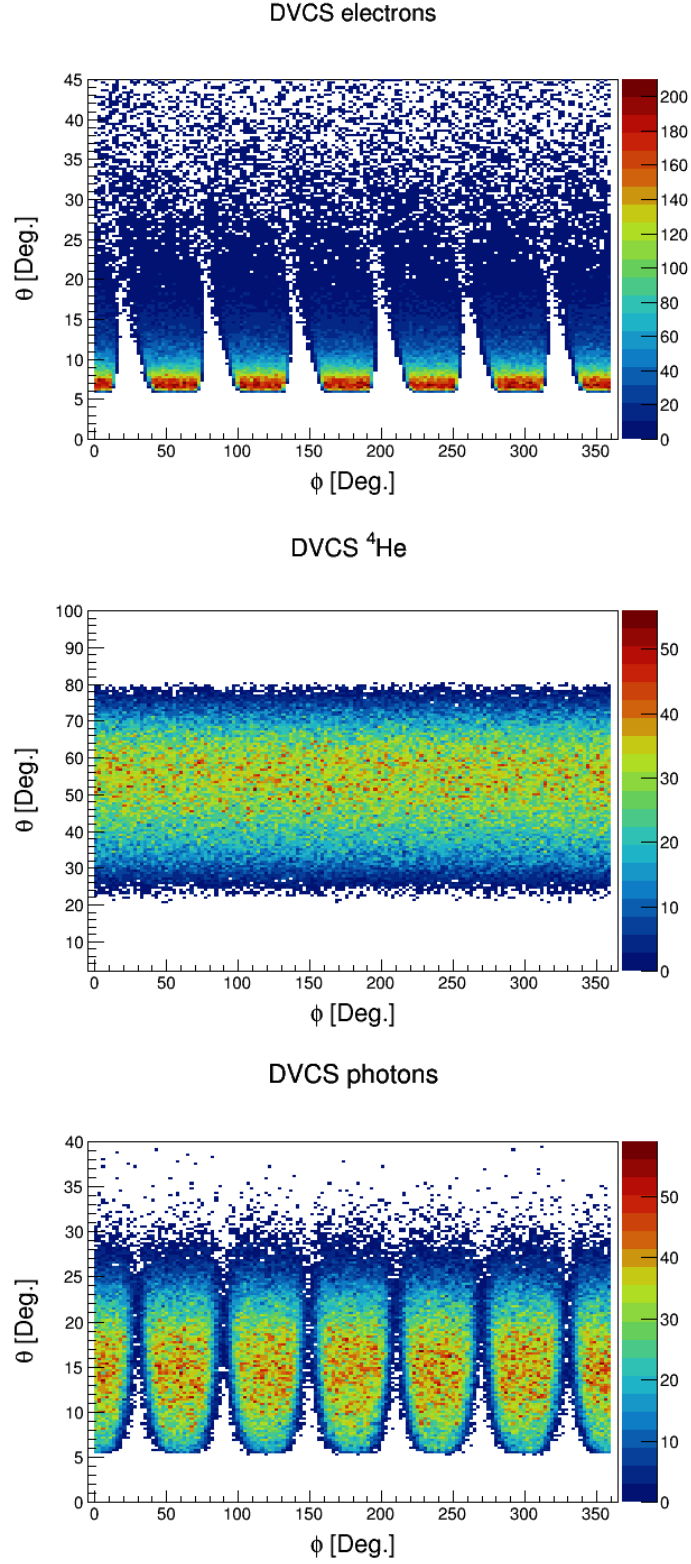
DVCS electrons

DVCS ^{4}He

DVCS photons

Figure 5.2: The angles θ and ϕ in the lab frame for all detected particles in coherent DVCS off ^{4}He. Top: the electron, middle: the ^{4}He nucleus, and bottom: the real photon.
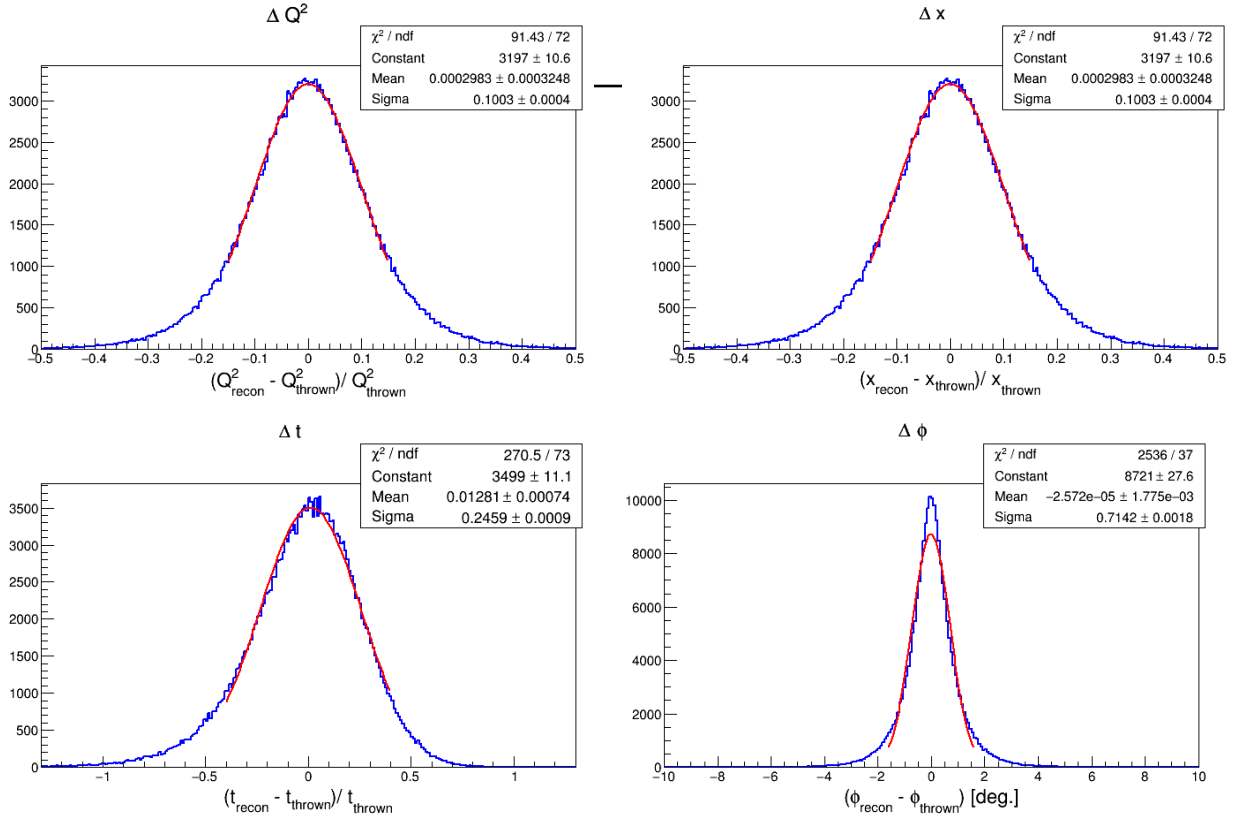
Figure 5.3: CLAS12 and ALERT resolutions for Q^2, x_B, t and ϕ.

histograms are the total simulated events (DVCS and π^0 events), while the blue histograms are for the simulated DVCS events only, and the red histograms are for the simulated π^0 events where only one photon of the π^0 two-photons decay is detected due to CLAS acceptance and may contaminate the DVCS sample. Figure 5.5 illustrates the effectiveness of the exclusivity cuts on reducing the background contamination to the coherent DVCS sample.

As mentioned previously, the simulated π^0 events were three times the number of the DVCS events. The true π^0 to coherent DVCS production ratio has been measured in eg6-experiment [14] to be 5% to 20% as can be seen in figure 5.6.

Figure 5.5 shows the remaining π^0 events after the exclusivity cuts that contaminate the DVCS sample. The true number of the coherent DVCS events can be formulated as:

$$N_{e^4He\gamma}^{True} = N_{e^4He\gamma}^{Exp.} - N_{e^4He\pi^0(\gamma)}^{Exp.}, \tag{5.8}$$

where $N_{e^4He\gamma}^{True}$, $N_{e^4He\gamma}^{Exp.}$ and $N_{e^4He\pi^0(\gamma)}^{Exp.}$ are the true number of coherent DVCS events, the experimentally measured number of $e^4He\gamma$ events and the contamination number, respectively. The contamination can be calculated by using real data and simulation. We define, for each
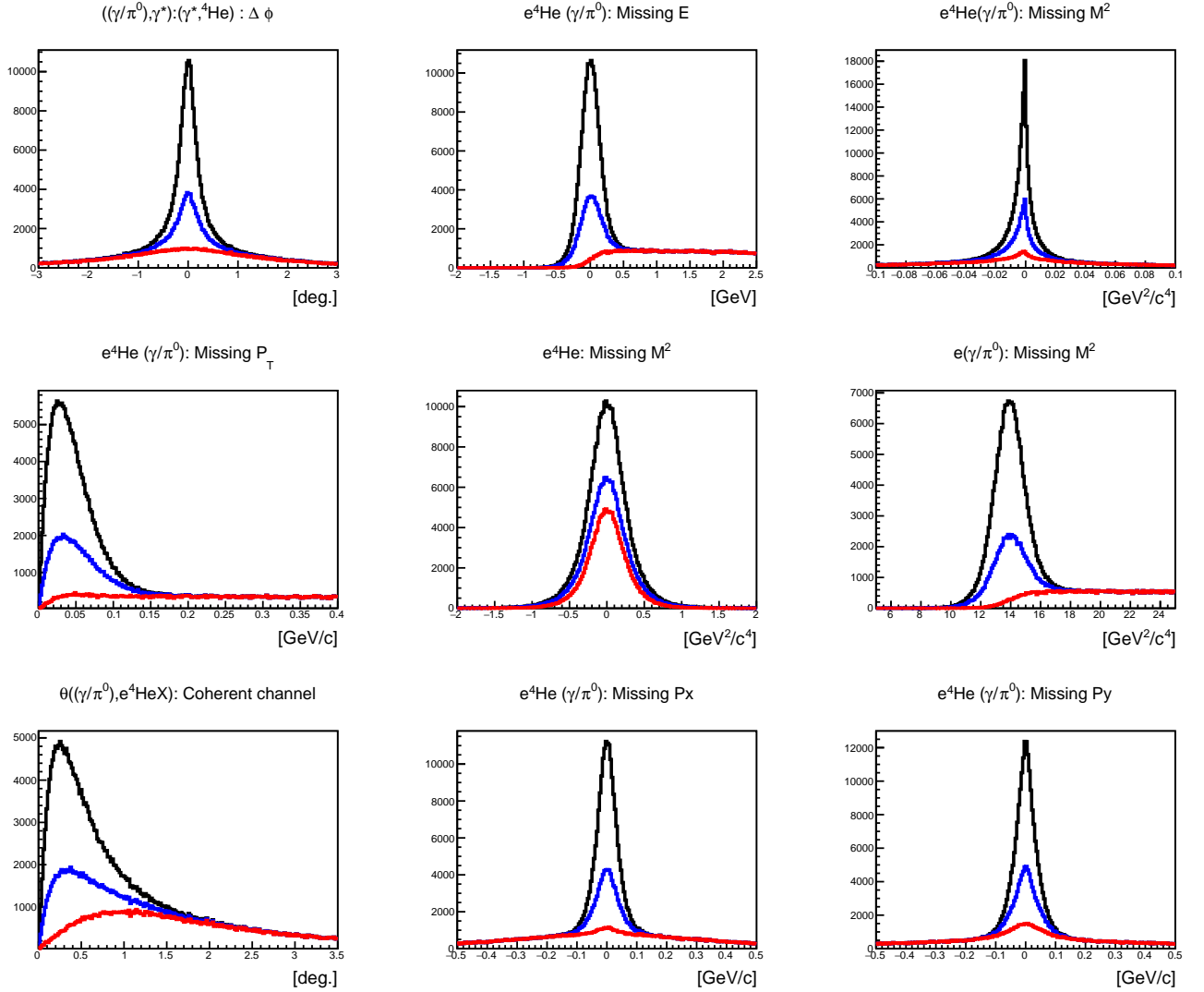
Figure 5.4: Contribution of non-exclusive (π^0) events to coherent DVCS sample. The blue curves represent the DVCS events. The black curves are the sum of the contributions from exclusive and non-exclusive events. The red curves show the π^0 events where only one photon of the π^0 two-photons decay is detected.
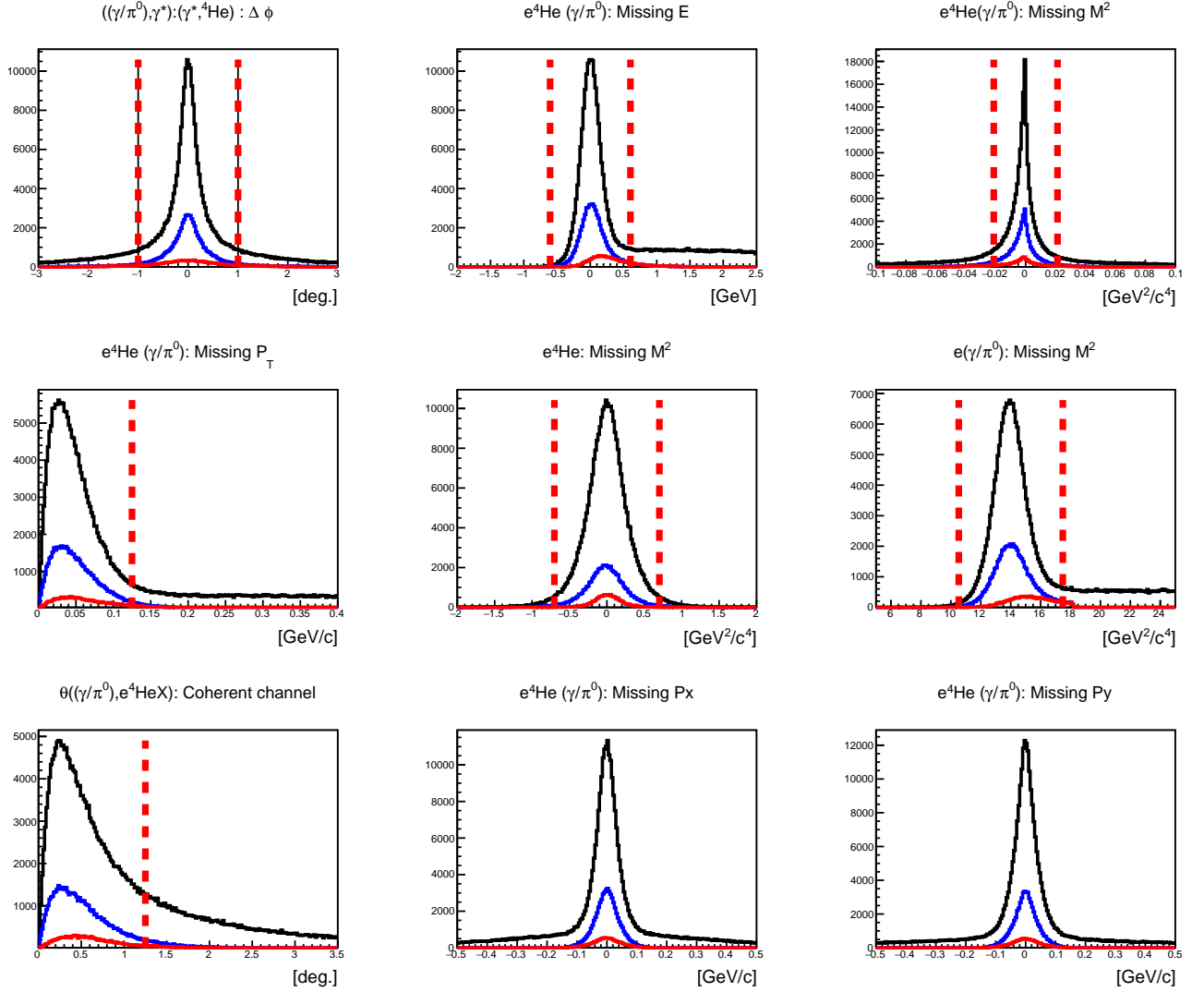
Figure 5.5: The effectiveness of the exclusivity cuts on reducing the background contamination to the coherent DVCS sample. The black curves are for the exclusive and non-exclusive events before exclusivity cuts. The blue curves are for the coherent DVCS events which satisfied the exclusivity conditions except for the cuts on the variable being displayed. The red histograms are for the π^0 background contamination that satisfied the exclusivity conditions. The red vertical lines show the values of the cuts,3σ cuts, for each exclusive variable. The missing momentum in x and y directions in the configuration $e^4He\gamma X$, are shown for information. See the text for the definition of the shown exclusive variables.
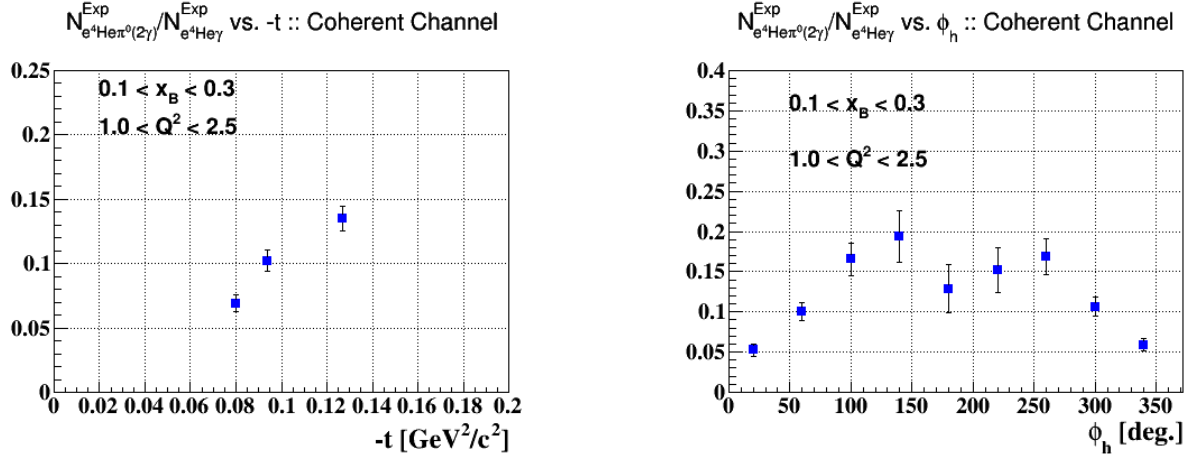
Figure 5.6: The π^0 to coherent DVCS production yield versus four-momentum transfer (-t) integrated over the photon angle ϕ (left), and versus ϕ (right) integrated over t as determined from CLAS-eg6 analysis [14]. Both plots are for $1.0 < Q^2 < 2.5$ and $0.1 < x_B < 0.3$.

kinematic bin and for each beam helicity state

$$N_{e^4He\pi^0(\gamma)}^{Exp.} = \frac{N_{e^4He\pi^0(\gamma)}^{Sim.}}{N_{e^4He\pi^0(\gamma\gamma)}^{Sim.}} * N_{e^4He\pi^0(\gamma\gamma)}^{Exp.}, \tag{5.9}$$

where $N_{e^4He\pi^0(\gamma\gamma)}^{Exp.}$ is the number of measured $e^4He\pi^0$ events, for which both photons of the π^0 have been detected. The quantity $\frac{N_{e^4He\pi^0(\gamma)}^{Sim.}}{N_{e^4He\pi^0(\gamma\gamma)}^{Sim.}}$ is the acceptance ratio for detecting an $e^4He\gamma$ event that originates from an $e^4He\pi^0$ event. It can be derived from Monte-Carlo simulations by generating and simulating $e^4He\pi^0$. $N_{e^4He\pi^0(\gamma)}^{Sim.}$ is the number of such events passing the DVCS requirements, while $N_{e^4He\pi^0(\gamma\gamma)}^{Sim.}$ is the number of simulated $e^4He\pi^0$ events passing the exclusivity cuts for $e^4He\pi^0$ events.

Figure 5.7 shows the coherent acceptance ratio as a function of ϕ_h using the CLAS12-ALERT setup. The mean value of the acceptance ratio for the coherent channel is around 8%.

The polarized beam of CEBAF and the large acceptance of CLAS will allow us to extract the beam spin asymmetry A_{LU} for various bins in Q^2, x_B, and t and ϕ for both the coherent DVCS and the π^0 electroproduction processes. The beam spin asymmetry in each bin is defined as:

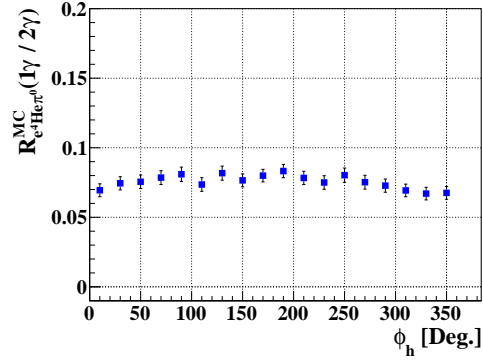$$A_{LU} = \frac{1}{P_B} \frac{N^+ - N^-}{N^+ + N^-}. \tag{5.10}$$

Figure 5.7: The coherent DVCS accpetance ratio as a function of ϕ integrated over $0.06 < -t < 0.2~GeV^2$, $1.0 < Q^2 < 2.5~GeV^2$, and $0.1 < x_B < 0.3$ using both CLAS12 and ALERT detectors.

where P_B is the beam polarization, and N^+ and N^- are the number of events detected with positive and negative electron helicity, respectively. The statistical uncertainty of A_{LU} is

$$\sigma A_{LU} = \frac{1}{P_B}\sqrt{\frac{1-(P_B A_{LU})^2}{N}} \tag{5.11}$$

where $N(N^+ + N^-)$ is the total number of measured events.

5.2 Exclusive Coherent Deep Virtual ϕ electroproduction

The CLAS12 detector will be used to detect one electron along with either a single kaon or a kaon pair, while the ALERT detector will detect the recoiling ^{4}He. The detected electron is constrained to the forward CLAS12 acceptance, and Fig. 5.8 shows the expected kinematic coverage after acceptance. The CLAS12 detector acceptance was simulated using the java-based fastMC, with resolution smearing taken from the older fortran fastMC. ALERT detector acceptance was taken from the latest detector design and simulation results.

In the case of a single kaon, the missing kaon will be reconstructed through missing momentum and energy. The missing 4-vector will be constrained to have a kaon mass, and the reconstructed mass of kaon and the missing kaon will be constrained to the ϕ mass. Fig. 5.9 shows the reconstructed mass of a missing K$^-$ after smearing the electron and K$^+$ with fastMC resolution smearing, and the detected ^{4}He with a momentum resolution in the
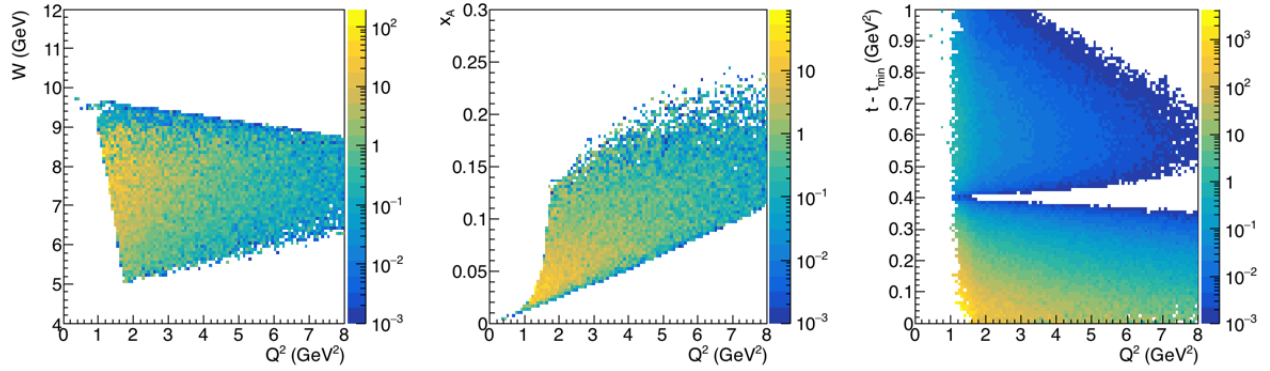
Figure 5.8: Total cross-section weighted kinematic distributions for electron, kaon, and ^{4}He coincidence events from ϕ production simulations. Z-axis units are in nb.

ALERT detector of $\Delta p < 10\%$. This ALERT detector resolution will drive the resolution of the t-variable calculation. Fig. 5.10 shows the expected $(t$ - $t_{min})$-bin migration after resolution effects.

In Fig. 5.11, the expected counts per day for the primary decay channel is shown versus t. In this calculation, the total luminosity is assumed to be 3×10^{34} cm^2/s, and the kaon and alpha detection efficiency is set at 50% in addition to the simulated acceptance. In addition to the $\phi \to K^+ K^-$ channel, we can gain additional statistics from the $\phi \to K^0_L K^0_S$ channel, with $K^0_S \to \pi^+ \pi^-$. In this case, the $\pi^+ \pi^-$ pair detection is assumed to have an efficiency of 70% in addition to the simulated acceptance.

Kaon PID will be performed through a combination of the TOF and veto from the LTCC, as proposed in PR12-12-007[25]. At kaon momenta < 5 GeV, the TOF will provide a 1-σ or better separation of kaons and pions. In combination with the charged pion momentum threshold of 2.5 GeV/c for the LTCC, kaon PID is not expected to be an issue. An additional cross-check of kaon identification can be performed with the CLAS12 RICH detector.

Background pion rates are expected to be small when the ALERT detector is required to tag a recoiling ^{4}He in the event; in this case, most pion background will come from non-ϕ meson production which can be cleaned up through missing mass cuts on the missing Kaon and reconstructed ϕ. For estimation of this background, phase-space for $\rho \to \pi^+\pi-$ and $\omega \to \pi^+\pi^-\pi^0$ was generated. Since a comprehensive cross-section calculation and parameterization for ρ/ω electroproduction off ^{4}He is non-trivial and somewhat outside the scope of the analysis, the cross-section for both ρ and ω is estimated to be 1000 times the ϕ cross-section. Misidentification of the pions or protons as kaons is simulated according to
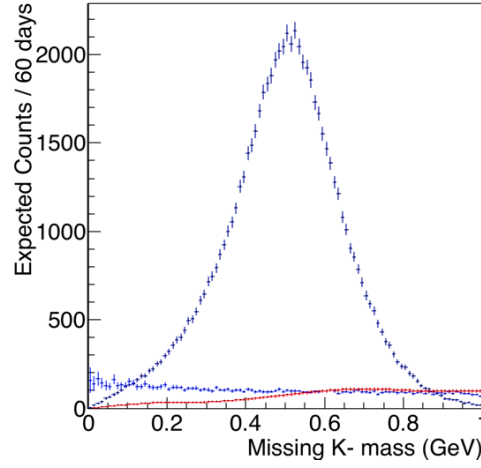
Figure 5.9: Expected K^- mass resolution from reconstruction using the electron and K^+ detected in CLAS12, and ^{4}He detected in ALERT with counts for proposed running time. The blue histogram shows the estimated background from coherent $\omega \to \pi^+\pi^-\pi^0$ and $\rho \to \pi^+\pi^-$, with a misidentified K^+ and a production cross-section 1000 times the ϕ cross-section. The red histogram estimates a misidentified ^{3}He or ^{2}H incoherent background using PYTHIA. See text for details.
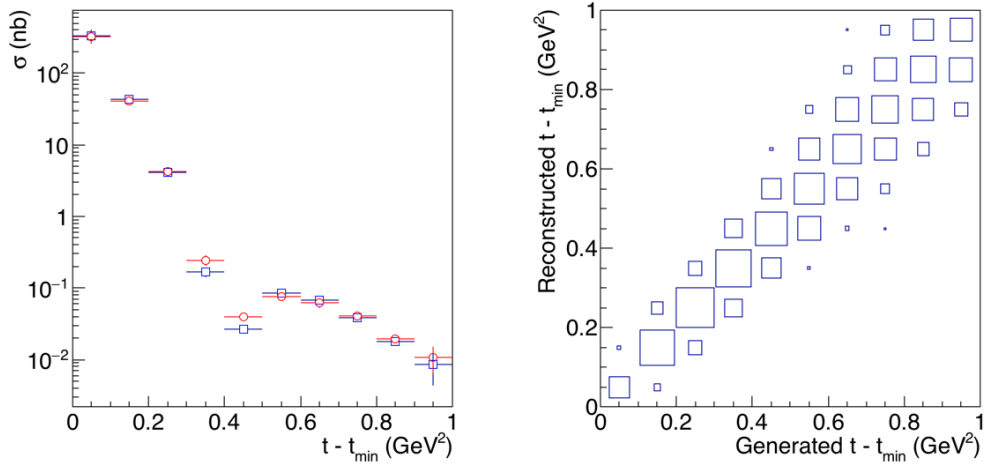

Figure 5.10: Quantification of t bin migration effects are shown in these two plots. The left plot shows cross-section versus reconstructed $t-t_{min}$ with red-circles, and the input generated $t-t_{min}$ with blue squares. On the right, reconstructed versus generated $t-t_{min}$ is plotted, which illustrates the expected bin-migration.
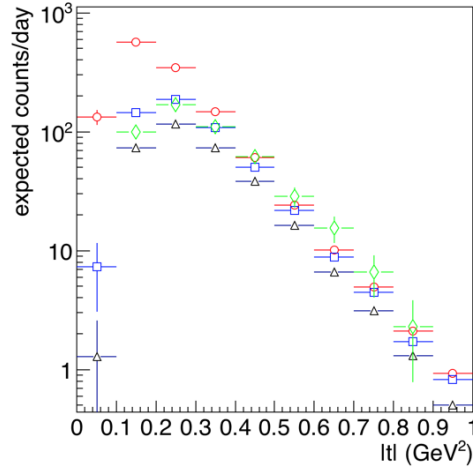
Figure 5.11: Expected counts per day for coherent ϕ production. Three analysis channels that will be investigated include the fully exclusive $K^+ K^-$ (black-triangles), missing K^- (red-circles), missing K^+ (blue-squares), and missing K^0_L with $K^0_S \to \pi^+ \pi^-$ (green-diamonds).

the expected TOF separation at low-momentum, and with a conservative 95% rejection in the LTCC above 3 GeV momentum for pions. The results are shown in Fig. 5.9. Another possible source of contamination will come from misidentification of ^{4}He in the ALERT detector. Any misidentification, combined with the missing mass cuts described above, should still provide a very clean separation of background.

A PYTHIA simulation for $\gamma + N \to X$ was performed, forcing a re-scattering between the recoil nucleon and the residual nucleus in ^{4}He. Re-scattering is required since a residual ^{3}He nucleus, with a residual momentum equal to its fermi-momentum from being bound in a ^{4}He, is almost completely outside ALERT's momentum acceptance. If the re-scattered ^{3}He or ^{2}H enters ALERT acceptance, it is assumed to have a ^{4}He misidentification probability of 10% (upper limit of expected misidentification). True kaons and misidentified protons or pions are also accepted in CLAS12 as described above and the total rate is calculated assuming the experiment's production luminosity. The total rate per day using worst-case estimates is calculated to be approximately 100 (or less than one-tenth the production rate), which will not greatly impact the ϕ identification. The estimated counts from this background are also shown in Fig. 5.9 for comparison to the signal peak.

5.3   Beam Time Request

5.3.1   Exclusive coherent DVCS Projections

5.3.1.1   Event Generator

In order to make projections of our results, we have used the following parametrization of the cross section which parameters were calibrated to reproduce the DVCS and exclusive π^0 electroproduction data from CLAS at 6 GeV [14]:

$$\frac{d^4\sigma}{dQ^2 dx_B dt d\phi} \propto \left(\frac{Q_0^2}{Q^2}\right)^\alpha \frac{1}{1+(\frac{x_B-x_c}{c})^2} \frac{1}{(1+bt)^\beta} \left(1 - d(1-cos(\phi))\right). \qquad (5.12)$$

This parametrization is the product of four factors which reproduce the DVCS and π^0, characteristics as follows:

- the Q^2-dependent term with: Q_0^2 the minimum allowed value and α a parameter which controls the shape of the distribution.

- the x_B term accounts for the dependence of the cross section on the parton distribution functions, with x_c the mean value of the Bjorken variable x_B.

- the t term accounts for the t-dependence of the elastic form factors of the helium and of the proton, via the parameters b and β.

- the ϕ term accounts for the cross section dependence on this angle, via the parameter d.

To reflect the change in the center of mass energy due to the higher beam energy of this proposal compared to E08-024 experiment, the parameter x_c (the mean value of x_B) is calculated from the DIS mean kinematic values, while the parameters b and β were scaled with respect to the center of mass energy change from 6 GeV to 11 GeV. Table 5.1 shows the values of the parameters used for the cross section parametrization of the four channels of interest: $e^4He\gamma$, $e^4He\pi^0$, $ep\gamma$, and $ep\pi^0$. Figure 5.12 shows a comparison between the experimentally identified coherent DVCS events from eg6 dataset and the simulated DVCS events as a function of the kinematic variables: Q^2, x_B, $-t$, and ϕ.

5.3.1.2   Projections

The projected precisions of the beam-spin asymmetries and Compton form factor for DVCS on ^{4}He are presented in this section. Based on the Impulse Approximation model [22], the real and the imaginary parts of the ^{4}He CFF were calculated and fed into our

Parameter	$e^4He\gamma$	$e^4He\pi^0$	$ep\gamma$	$ep\pi^0$
Q_0^2	1.0 GeV^2/c^2	1.0 GeV^2/c^2	1.0 GeV^2/c^2	1.0 GeV^2/c^2
α	2.5	3.0	1.5	1.5
b	-6.0 GeV^2/c^2	-8.8 GeV^2/c^2	-1.408 GeV^2/c^2	-1.408 GeV^2/c^2
β	6.5	7.3	4.0	1.5
x_c	0.27	0.3	0.2	0.5
c	0.2	0.3	0.2	0.5
d	0.4	0	0.4	0

Table 5.1: Values of the parameters used in our event generator.
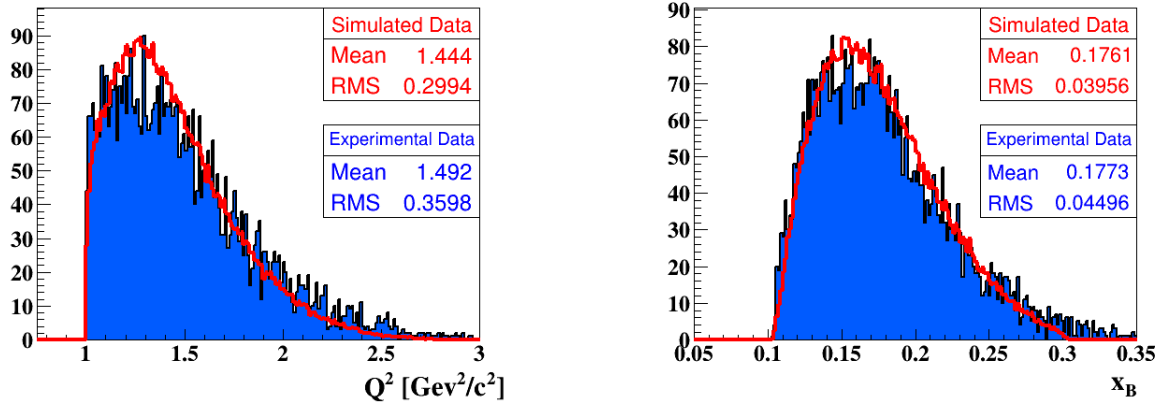
Figure 5.12: Comparison between the simulated $e^4He\gamma$ DVCS events (in red lines) and the experimental DVCS events from eg6 (in shaded blue) with 6 GeV beam as a function of the kinematic variables: Q^2 and x_B [14].
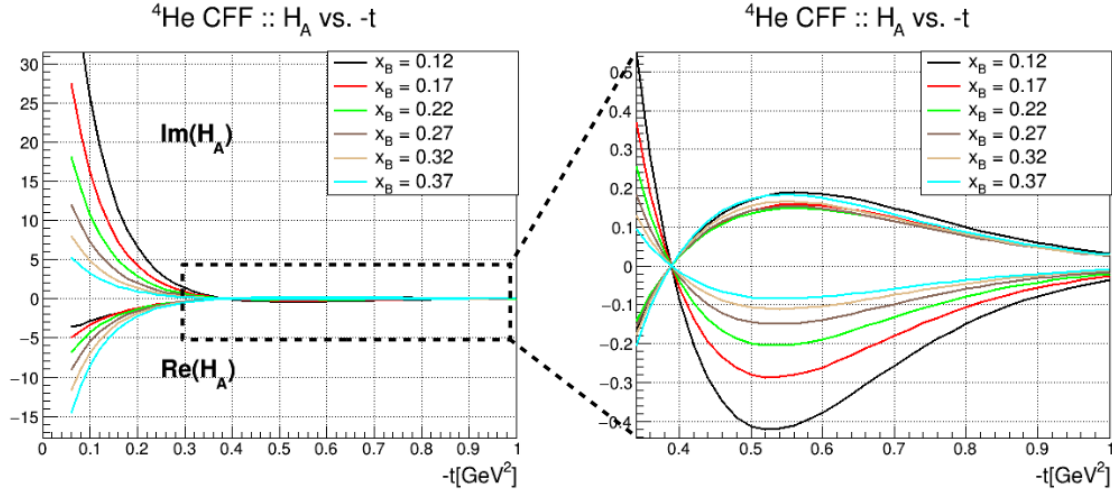
Figure 5.13: From the impulse approximation model, the imaginary and the real part of the ^{4}He CFF as a function of -t at fixed x_B values.

event generator to produce coherent DVCS events with beam-spin asymmetries following the formalism presented in section 2. Figure 5.13 presents the t dependence of the real and the imaginary parts of the ^{4}He CFF at different values of x_B.

Figure 5.14 shows the binning x_B and $-t$ binning used. The simulated data is integrated over the full Q^2 range shown in figure 5.1. For the BSA A_{LU} dependence on $-t$, the data has been binned into three bins in x_B, 11 bins in $-t$ and 13 bins in ϕ. The statistical error bars are calculated for 20 days at a luminosity of 3×10^{34} cm^{-2}s^{-1} (jointly with Tagged EMC proposal request) and 10 days at a luminosity of 6×10^{34} cm^{-2}s^{-1} specifically dedicated to this proposal. The assumed beam polarization is 80%. Figure 5.15 shows the reconstructed beam-spin asymmetries as a function of the angle ϕ for two bins in $-t$ at a fixed x_B value presenting a high and a low statistic bins. The projected precision of A_{LU} at ϕ equal to 90° for the different bins is presented in figure 5.16. The projected uncertainties on the reconstructed real and imaginary parts of the CFF is shown in figure 5.17.

The parton density profile of ^{4}He can be extracted from the CFF H^A via the so-called Hankel transform. For $\xi = 0$ ($t = -\Delta_\perp^2$), at a longitudinal momentum x and a transverse position (impact parameter $b_\perp$), the parton density reads

$$\rho(x, 0, b_\perp) = \int_0^\infty J_0(b\sqrt{t}) H^A(x, 0, t) \sqrt{t} \frac{dt}{2\pi} \qquad (5.13)$$

where J_0 is the first-order cylindrical Bessel function.

Figure 5.14: The binning in $-t$ at fixed values of x_B.
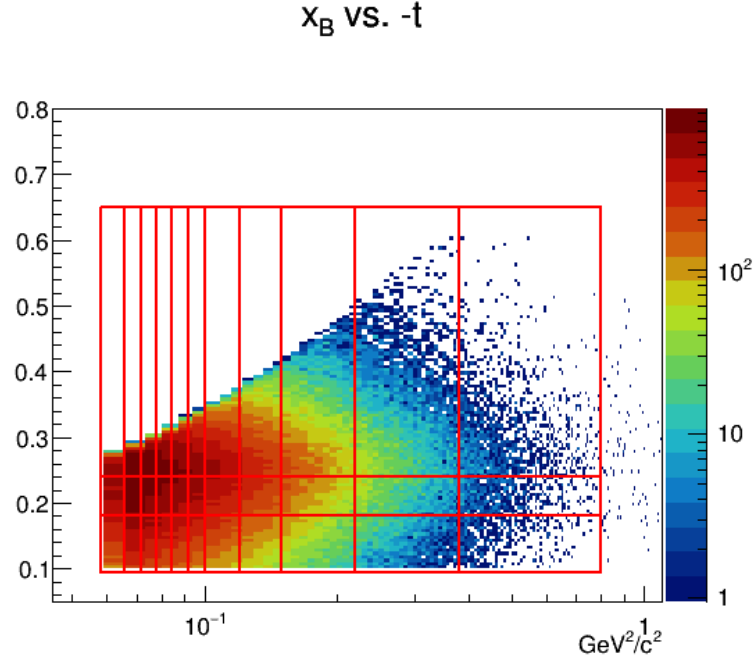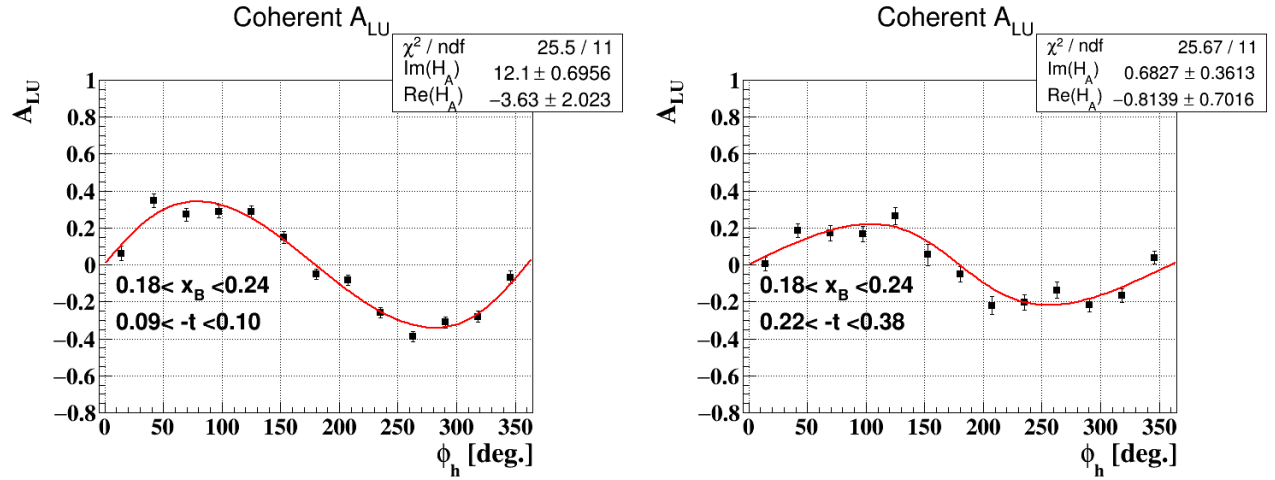

Figure 5.15: The coherent beam-spin asymmetry projections as a function of the angle ϕ between the leptonic and the hadronic planes, for two different bins $-t$ at the same x_B range. The red solid curves represent a fit to the data in the full form of the asymmetry, equation 2.8, with the real and the imaginary parts of the CFF as the free parameters of the fit.
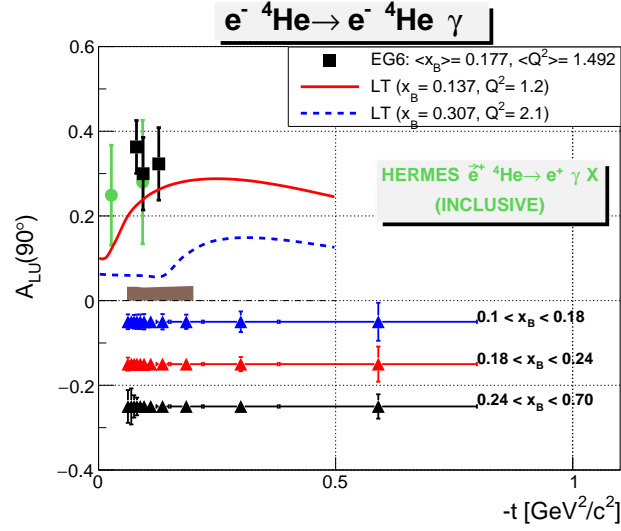
Figure 5.16: Projected precision for the A_{LU} (90°), from the fit, for coherent DVCS on ^{4}He versus $-t$ compared to the previous measurements from CLAS-eg6 (black squares), HERMES (green circles) and spectral function calculations (LT curves).
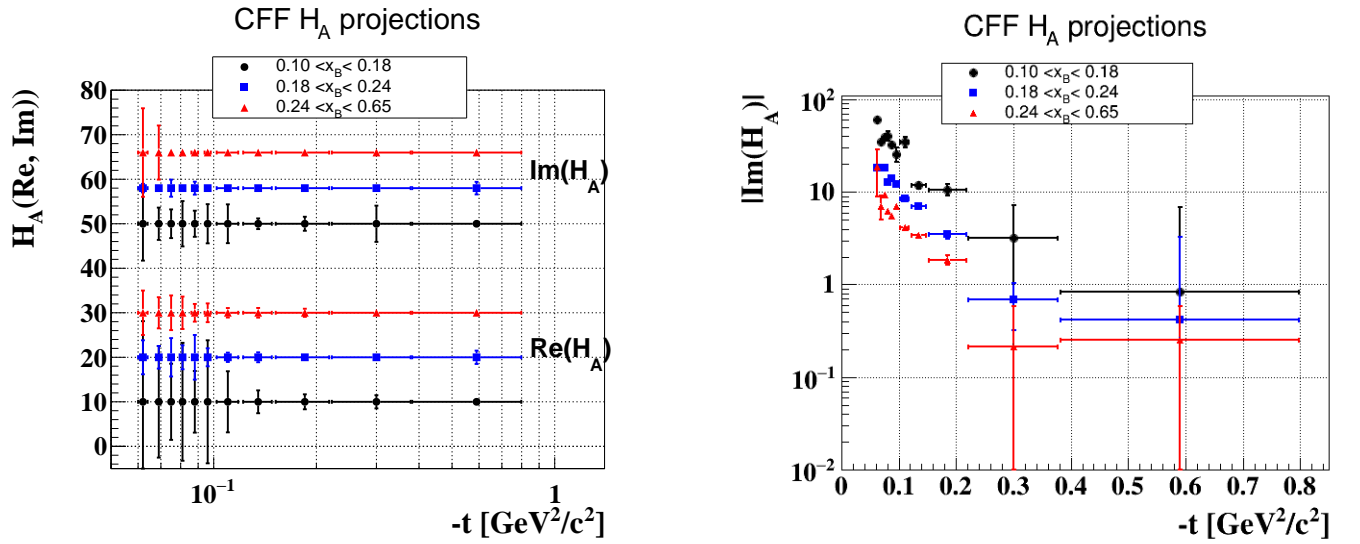
Figure 5.17: On the left, the projected statistical uncertainties for the real and imaginary parts of the CFF H_A, from the fits, as a function of $-t$ at fixed ranges in x_B. On the right, the projected statistical uncertainties of the absolute value of the imaginary part in logarithmic scale.

Figure 5.18: On left, a fit to the extracted absolute value of the CFF imaginary part H_A as a function of -t in the x_B range [0.18, 0.22]. On the right, the extracted parton density profiles as a function of the impact parameter, $b_\perp$, are compared to the Impulse Approximation (IA) calculations at the mean x_B values in the different bins.

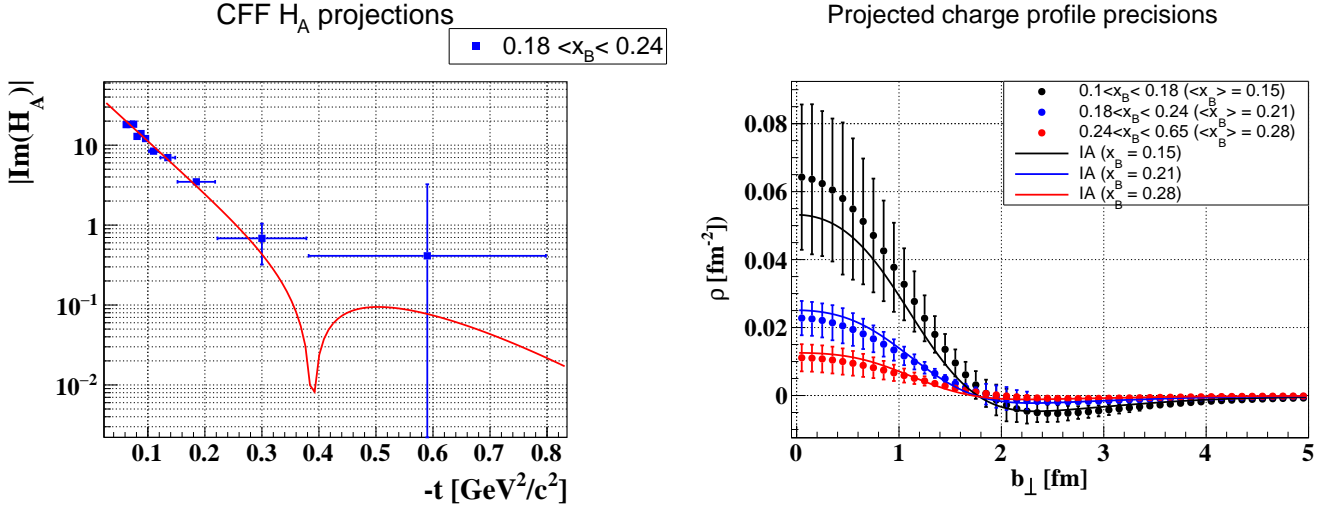The imaginary part of H^A CFF ($H^A_{Im}(\xi, t)$) is the combination of the GPD H_A at the lines $x = \pm\xi$ ($H^A_{Im}(\xi, t) = H_A(\xi, \xi, t) - H^A(-\xi, \xi, t)$), and can be extracted from the experimental BSA in a model independent way. If we assume that the anti-quark contribution is small in our kinematical region, then $H^A_{Im}(\xi, t) = H^A(\xi, \xi, t)$ is a good approximation. Experimentally, we measure the CFF $H^A(\xi, \xi, t)$, while what appears in the density equation is the CFF $H^A(\xi, 0, t)$. Reference [49] suggests that it is a 10% to 20% correction that can be applied to the data. For the moment, we do not apply this correction.

The left plot of figure 5.18 shows a fit to the extracted imaginary part of the ^{4}He CFF, H^A, as a function of $-t$ in a fixed x_B range. The fit form takes the same form of the elastic form factor, that is $[p_0(1 - (p_1 t)^6)e^{-p_2 t}]$. Using this fit, we performed an extraction of the density profile in the x_B range [0.18, 0.25] following the previously presented formalism and compared it to the calculated densities based on the Impulse Approximation model. The error bars on the projected density profile were extracted for few $b_\perp$ values by performing many Hankel transforms via varying the fitting parameters (p_0, p_1, p_2) in a Gaussian form within their uncertainties from the fit. The results are presented in figure 5.18(right).

5.3.1.3 Systematic uncertainties

It is particularly convenient to use the BSA A_{LU} as a DVCS observable, because most of the experimental systematic uncertainties, such as normalization and efficiencies that appear in the cross sections cancel out in the asymmetry ratio. However, some systematic uncertainties remain and they still contribute to the measured A_{LU}. The main known sources of systematic uncertainties are: the DVCS selection cuts, the fitting sensitivity to our binning, the beam polarization and the background (non exclusive π^0) acceptance ratio. In the following, we present estimates of the contribution from each source based on our prior knowledge during CLAS-eg6 DVCS analysis [14] and our simulation studies of the proposed ALERT detector.

In order to evaluate the systematic uncertainties stemming from the DVCS selection cuts, the eg6-analysis was repeated with changing the width of the exclusive cuts. The resulting systematic uncertainty to the A_{LU} asymmetry was around 8% for the coherent DVCS channel. Because of the important improvement we expect with ALERT in terms of resolutions, we decided to reduce this uncertainty to 5%.

Regarding the sensitivity of the fit results to our binning, the eg6 data were binned into two different bins in ϕ and the reconstructed asymmetries were compared. The associated systematic uncertainty for A_{LU} at $\phi = 90°$ was found to be of 5.1%. For the proposed measurements, we expect to achieve higher statistics and therefore we reduced the expected systematics to 3%.

The beam polarization will be measured during the experiment by the Hall B Møller polarimeter. This polarimeter measures the angular distribution of the Møller electrons to obtain the beam polarization. The precision of the Hall B Møller polarimeter was measured to be around 3.5% [50], which is expected to be improved with the upgrade. We assume therefore a 3.5% systematic uncertainty on the measured asymmetries similar to what was achieved during 6 GeV run.

To estimate the systematic uncertainty associated with the calculated acceptance ratio (R), two techniques can be used. The first is via repeating the analysis by implementing R differently, while the second technique is by using two generating models to calculate R. In CLAS-eg6 analysis both methods were investigated. A maximum variation of 0.6% has been observed on the coherent A_{LU} at $\phi = 90°$. An upper limit of 1% is assumed for the proposed measurements.

The total systematic uncertainty on the measured A_{LU} at $\phi = 90°$ is the quadratic sum

of the previously described individual uncertainties. Table 5.2 summarizes the systematic uncertainties for both CLAS-eg6 and the proposed measurements.

Systematic source	CLAS-EG6 experiment	Proposed experiment	Type of systematic error
DVCS cuts	8 %	5%	bin to bin
Data binning	5.1%	3%	bin to bin
Beam polarization	3.5%	3.5%	Normalization
Acceptance ratio	0.6%	1%	bin to bin
Total	**10%**	7%	bin to bin

Table 5.2: The systematic uncertainties on the measured coherent beam-spin asymmetries at $\phi = 90°$ from CLAS-eg6 and the proposed experiment.

5.3.2 Exclusive coherent Φ production Projections

5.3.2.1 Event Generator

Event generation for ϕ production off ^{4}He is done in two steps. First, the cross-section for ϕ production off a proton target is generated, and then the charge form-factor of ^{4}He is folded in, while the corresponding charge form-factor for the proton is divided out. The phase-space for generation is created by sampling uniformly in Q^2, x_B, and t. For event generation purposes, we define $x_A = Q^2/2M_{He}\nu$, and $t = (P_{^4He} - P'_{^4He})^2$.

Since the cross-section must first be calculated off the proton, the relevant value for t must be recalculated. For this we define a new variable t_p which is calculated assuming a target proton with a momentum uniformly distributed up to the ^{4}He fermi-momentum in the initial state, and a scattered proton with 1/4 the momentum of the recoiling ^{4}He with a uniformly distributed fermi-momentum in the final state. The cross-section is then given by:

$$\frac{d\sigma_{^4He}}{dt}(t) = \frac{d\sigma_p}{dt}(t_p)\left(\frac{A\,F_{C,^4He}(t)}{F_{C,p}(t_p)}\right)^2 \tag{5.14}$$

where A is the nucleon number of ^{4}He, and F_C the charge form factor of ^{4}He is parametrized using the world data through its first minimum in t following: $F_{C,^4He} = (1-(2.5t)^6)e^{11.7t}$. The calculation of the ϕ production cross-section off the proton follows the exact formalism as put forth by the accepted CLAS12 proposal PR12-12-007 [25]. A brief recap of that calculation is presented below: The 3rd order differential cross-section for the

unpolarized case is defined as:

$$\frac{d^3\sigma}{dx_B\,dQ^2\,dt} = \Gamma(x_B, Q^2, E)\left(\frac{d\sigma_T}{dt}(W, Q^2, t) + \varepsilon\frac{d\sigma_L}{dt}(W, Q^2, t)\right) \tag{5.15}$$

Where Γ is the virtual photon-flux and ε is the virtual photon polarization. The transverse cross-section is parameterized in W and Q^2 to fit world data. The ratio of longitudinal to transverse cross-section is also fit to world data as a function of Q^2. The t-dependence is incorporated as an exponential with a slope that depends on W. The exact functional forms for each of these is omitted here for brevity, but can be found in PR12-12-007 [25]. The total calculated cross-section for ϕ electroproduction off ^{4}He follows that formalism, except everywhere $d\sigma/dt$ enters the calculation, the calculation of Eqn. 5.14 is used instead. The plots of the cross-section versus world data from PR12-12-007 are shown below in Fig. 5.19.

5.3.2.2 Gluon GPD extraction from ϕ production

The gluon GPD $|\langle H_g\rangle|$ averaged over x_B, can be expressed as the dominant term in the longitudinal differential cross-section for coherent ϕ production [25, 59, 60, 61]:

$$\frac{d\sigma_L}{dt}(\text{proton}) = \frac{\alpha_{em}}{Q^2}\frac{x_B^2}{1 - x_B}[(1 - \xi^2)|\langle H_g\rangle|^2 + \text{terms in}\langle E_g\rangle] \tag{5.16}$$

Here α_{em} is a QED coupling constant, and ξ is the skewness. For ϕ production off the spin zero ^{4}He target, we can expect:

$$\frac{d\sigma_L}{dt}(^4\text{He}) \propto |\langle H_g\rangle|^2 \tag{5.17}$$

This longitudinal cross-section can then be written in terms of experimental observables:

$$\frac{d\sigma_L}{dt} = \frac{1}{(\varepsilon + 1/R)\Gamma(Q^2, x_B, E)}\frac{d^3\sigma}{dQ^2 dx_B dt} \tag{5.18}$$

Where $R = \sigma_L/\sigma_T$ is the ratio of longitudinal to transverse cross-sections. In order to find R, we exploit the fact that the spin-density matrix of the ϕ meson is directly related to this ratio. If one assumes s-channel helicity conservation (SCHC) for the $\gamma^* \to \phi$ transition (which HERMES data supports [62]), one can write a simplified matrix element:
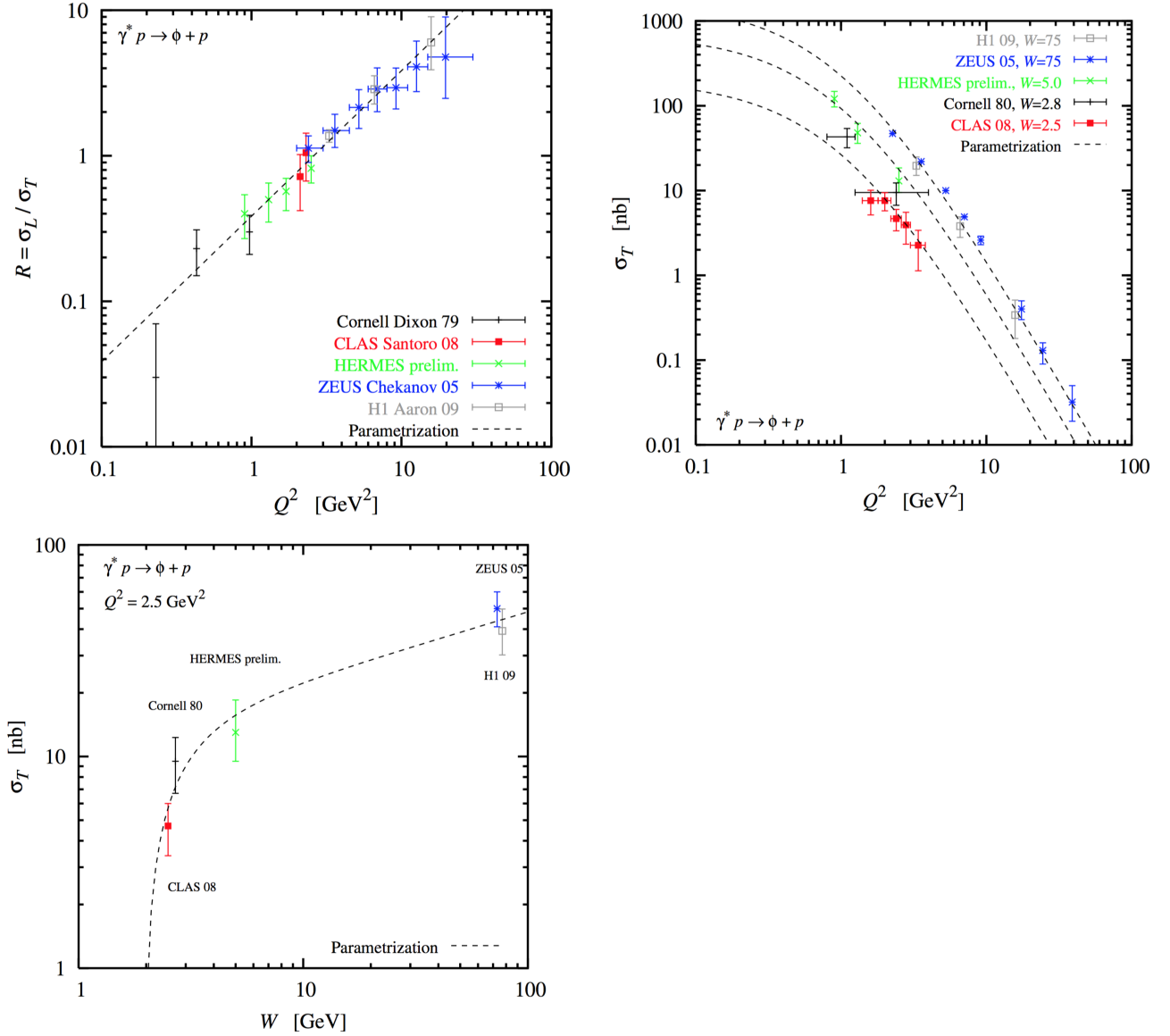
Figure 5.19: Figures come directly from PR12-12-007 [25]. The parametrization in W and Q^2 used for cross-section calculation for ϕ production off a proton target plotted against world data. For more information on the world data, see references: CLAS [51, 52], Cornell [53, 54], HERMES [55], NMC [56], ZEUS [57], and H1 [58].

$$r_{00}^{04} = \frac{\varepsilon R}{1 + \varepsilon R} \tag{5.19}$$

This element can be directly obtained through the the distribution of decay kaons in the ϕ helicity frame:

$$W(\cos\theta_H) = \frac{3}{4}\left[(1 - r_{00}^{04}) + (3r_{00}^{04} - 1)\cos^2\theta_H\right] \tag{5.20}$$

5.3.2.3   Projections

The extraction of gluon GPDs will need the cross-section calculated in bins of Q^2, x_V and $t - t_{min}$. The variable x_V is similar to x_A but takes into account the production of a vector of mass greater than zero, and is useful for direct comparison between DVMP and DVCS. A summary of the many different notations for x calculation using different target masses and vector masses is shown below:

$$x_B = \frac{Q^2}{W^2 + Q^2 + M_p^2} \tag{5.21}$$

$$x_A = \frac{Q^2}{W^2 + Q^2 + M_{^4He}^2} \tag{5.22}$$

$$x_V = \frac{Q^2 + M_V^2}{W^2 + Q^2 + M_{^4He}^2} = \left(\frac{Q^2 + M_V^2}{Q^2}\right)x_A \tag{5.23}$$

$$x_{Vp} = \frac{Q^2 + M_V^2}{W^2 + Q^2 + M_p^2} = \left(\frac{Q^2 + M_V^2}{Q^2}\right)x_B \tag{5.24}$$

The exact binning will depend on total run-time, but a feasible binning for 30 days beam-time is shown in Fig. 5.20. In this binning configuration, the largest occupancy bins will have greater than 1000 signal events in the proposed (20+10) days beam request. The smaller occupancy bins can have 100 or less events, and may be folded together where necessary. Additionally, an identical binning to the DVCS analysis can be performed for a more direct comparison of results; the data are expected to overlap in much of the t, Q^2 and $x_{V,A}$ phase-space.

To extract the ratio R, it is necessary to boost to the ϕ-helicity frame and fit the $\cos(\theta)$ distribution of one of the decay kaons, as described in Eqn. 5.20. The resolution of this θ distribution is highly dependent on the ALERT momentum resolution of the ^{4}He.
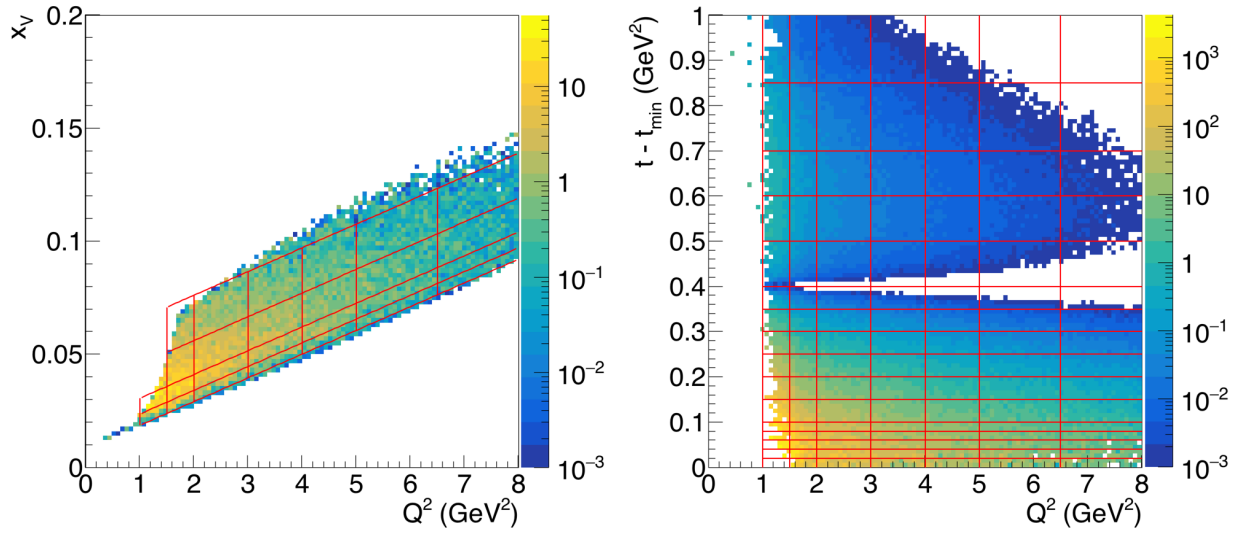
Figure 5.20: A possible binning over the accepted phase-space for gluon GPD extraction with ϕ production.

Shown in Fig. 5.21 is the extraction of r_{00}^{04} for a bin with $[0.02 < t - t_{min} < 0.04\,GeV^2]$, $[0.025 < x_V < 0.05]$, and $[1.5 < Q^2 < 2.0\,GeV^2]$. The two panels show the effect of resolution on the extraction; the left plot has standard CLAS12 resolutions plus a 5% momentum resolution for the ^{4}He detected by ALERT, and the right plot shows the same except a resolution of 10% in ALERT. The general characteristic of increasing resolution, is a flattening of the $\cos(\theta)$ distribution. Additional constraints may be able to improve the momentum resolution of the ALERT detector and even correct the θ distributions. For comparison, an R extraction in a less populated bin is shown in Fig. 5.22.

Once R is extracted, the average gluon density is calculated by performing a Hankel transformation (Eqn. 5.13), where the gluon GPD is defined as the square-root of the normalized longitudinal differential cross-section:

$$|\langle H_g \rangle|(t) \propto \sqrt{\frac{d\sigma_L}{dt}(t - t_{min}) \Big/ \frac{d\sigma_L}{dt}(0)} \tag{5.25}$$

This normalization of the cross-section to the $t = t_{min}$ point simplifies the analysis and cancels some of the systematic effects that would otherwise increase the uncertainty. An example of this Hankel transformation is shown in Fig. 5.23. The extraction is performed on the simulated events with all acceptance, smearing, and background effects included. The binning choice reflects that of the example extraction performed above for DVCS: x_{Vp} between 0.18 and 0.25, with an additional Q^2 cut between 2.0 and 3.0 GeV^2. A

Figure 5.21: A fit to the $\cos(\theta)$ distribution of the K^+ in the reconstructed ϕ-helicity frame within a bin of values $[0.02 < t - t_{min} < 0.04\,GeV^2]$, $[0.025 < x_V < 0.05]$, and $[1.5 < Q^2 < 2.0\,GeV^2]$. This is one of the highest count bins, and is calculated to have over 1000 events during the run period. The dashed line shows the distribution that was generated. The data are then fitted after acceptance and resolution smearing for comparison to the generated values. The left plot assumes a momentum resolution of 5% for the ALERT detection of ^{4}He, and the right plot assumes a momentum resolution of 10% .
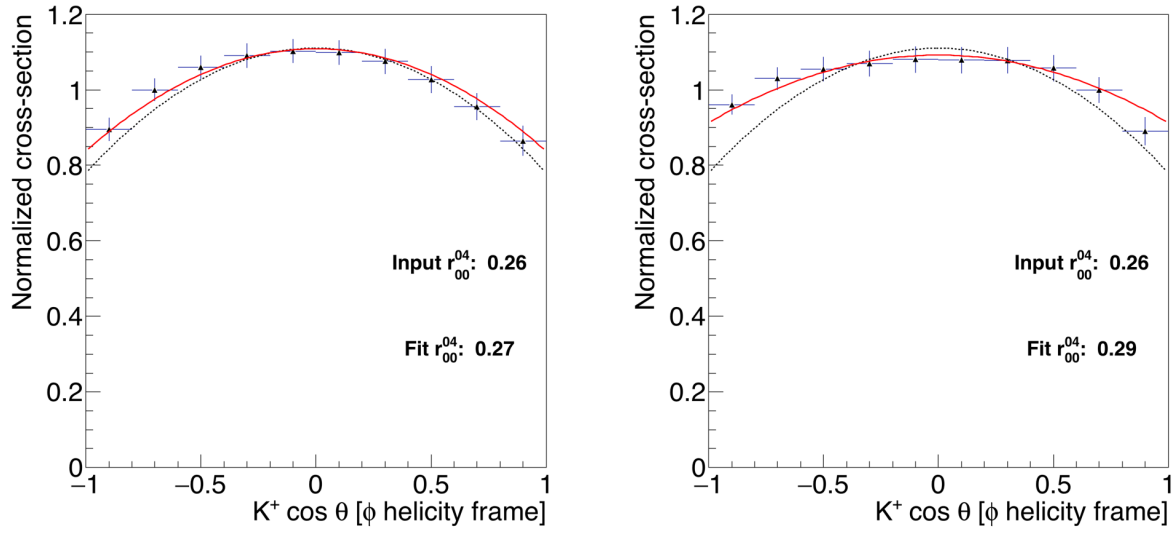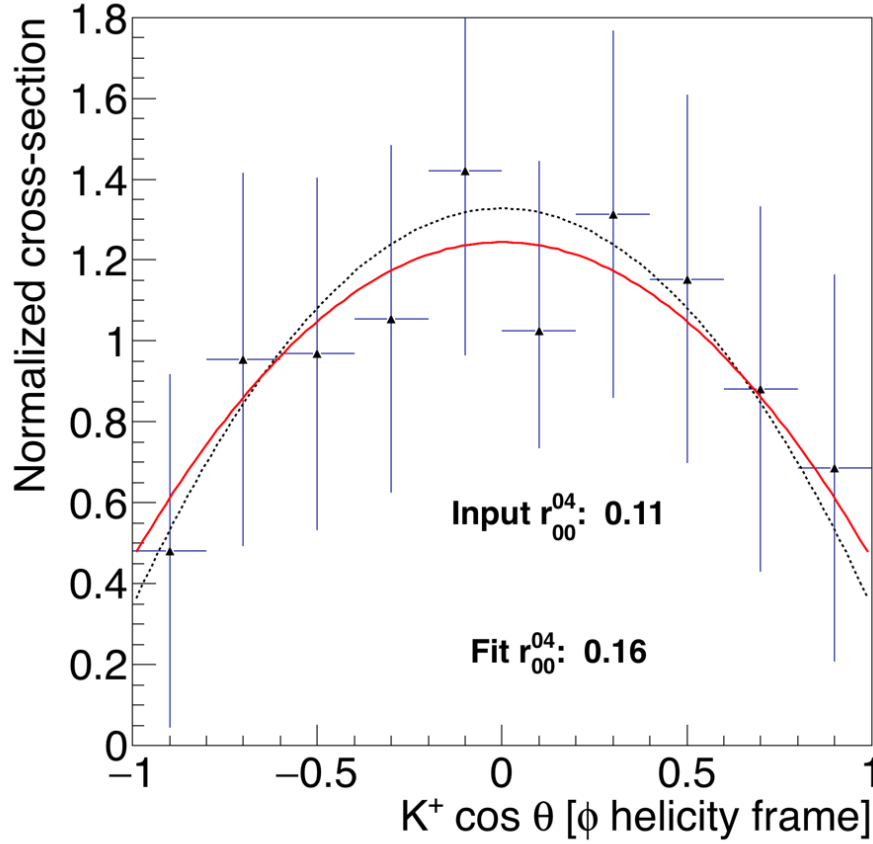
Figure 5.22: A fit to the $\cos(\theta)$ distribution of the K$^+$ in the reconstructed ϕ-helicity frame within a bin of values $[0.2 < t - t_{min} < 0.25\,GeV^2]$, $[0.075 < x_V < 0.1]$, and $[2.0 < Q^2 < 2.5\,GeV^2]$. This is a lower occupancy bin, expected to have 100 events after 60 days, and is shown for comparison to the high statistics fit from Fig. 5.21. The dashed line shows the distribution that was generated. The data are then fitted after acceptance and resolution smearing for comparison to the generated values. An ALERT detector momentum resolution of 5% is assumed.

Figure 5.23: An example of the calculated average gluon density for an x_{Vp} bin between 0.18 and 0.25, and a Q^2 bin between 2.0 and 3.0 GeV^2. The band represents the combined statistical and systematic uncertainties.

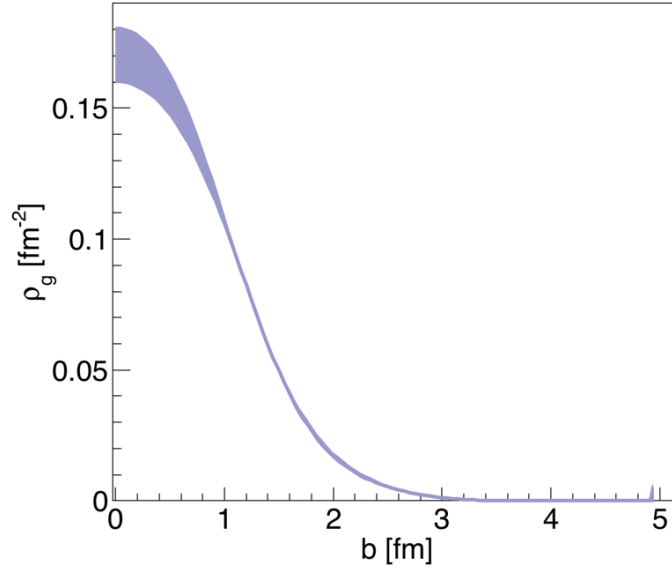second transformation is performed on the generated cross-section before any acceptance or resolution effects. The difference between this pre-acceptance/smearing transformation and the post acceptance/smearing transformation is used to estimate the total systematic uncertainty on the calculation. The combined systematic and statistical uncertainty is shown in the width of the band for the gluon density calculation in Fig. 5.23.

The sensitivity of the low-b calculation of gluon density comes from high-t events. Investigating the location of the first diffractive minimum in F_C for ^{4}He is important for the discussion of the comparison between charge and gluon densities. The requested beam-time for this experiment provides just the required statistics to quantitatively discern the location, if it exists, of the first diffractive minimum within the t range available. Fig. 5.24 shows the expected root-t spectrum, with uncertainties that reflect statistics and systematics after all acceptance and resolution smearing and the same binning used to extract the gluon density in Fig. 5.23 above: $0.18 < x_{Vp} < 0.25$, and $2.0 < Q^2 < 3.0 \, GeV^2$. The blue line shows a fit used to find the diffractive minimum. Fewer statistics would still allow a high precision gluonic RMS radius calculation, where low-t events are most important. Higher statistics would allow us to better locate a diffractive minimum if additional nuclear effects reduce the sharpness of the minimum.
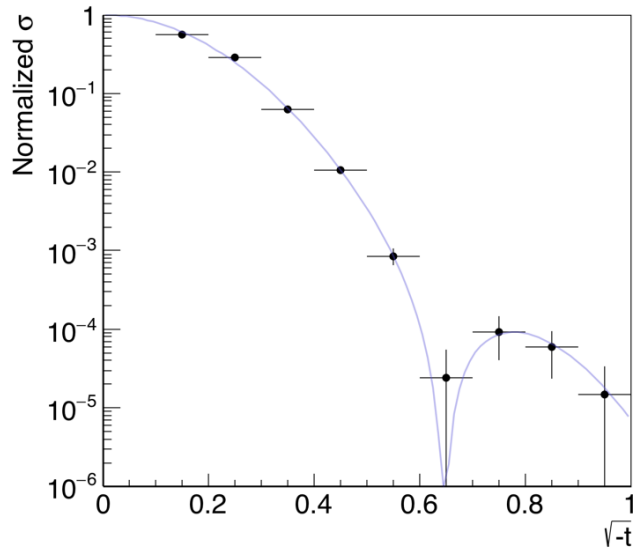
Figure 5.24: The normalized cross-section as a function of $\sqrt{-t}$ for an x_{Vp} bin between 0.18 and 0.25, and a Q^2 bin between 2.0 and 3.0 GeV^2. Total running time for this experiment provides adequate statistics to locate the first diffractive minimum if it exists from ϕ production within ALERT t acceptance. The graph points have uncertainties that include all statistical and resolution/bin-smearing effects. The blue line is a fit to the graph with a similar form of $|F_C|^2$ for the ^{4}He nucleus.

Summary and Beam Time Request

We are proposing an experimental program that will provide data, for the first time, required for a global analysis that will extract partonic GPDs in a dense nucleus, in this case GPD $H_{^4\text{He}}$ for both quarks and gluons together in ^{4}He. The DVCS process has been the hallmark of the 3-D investigation of the nucleon structure at large x at Jefferson Lab. This investigation was extended successfully to the ^{4}He nucleus in the 6 GeV era albeit with limited kinematic leverage and statistics. This proposal will not only provide Compton form factors for the quarks contributions but also uses the electroproduction of ϕ to explore the contribution of gluons at large x, in tandem with that of the quarks.

This program will be a precursor of physics to be explored at a future EIC, namely 3-D imaging of spin zero nuclei. Other mesons will be accessible in the same data stream of this proposed experiment extending the physics reach of this proposal. For example, a flavor decomposition of these form factors will be possible by investigating the deep exclusive production of pseudoscalar and vector mesons with masses below the ϕ meson, like π^0, ρ, ω. Given the limited energy reach of Jefferson Lab, the most promising access to the gluonic structure of nucleon and nuclei is by using the ϕ meson production as a probe as was done in proposal E12-12-007. Of course a future EIC will allow the use of heavier mesons such as the J/Ψ and the Υ for a "cleaner" gluonic probe, nevertheless we believe that at large x the strange quark contribution could be separated from that of the gluons in a global analysis where DVCS and DVMP data from different pseudoscalar and vector mesons, thus this coherent proposal.

In order to achieve the error bars presented in this proposal, we request 20 days of running with 11 GeV electron beam at a luminosity of 3×10^{34} cm^{-2}s^{-1} (same beam time request as the tagged EMC proposal) and 10 days at 6×10^{34} cm^{-2}s^{-1} with helium target (specific to this proposal), both with 80% longitudinally polarized beam. We will also need 5 days of commissioning of the ALERT detector at 11 GeV and 2.2 GeV with helium and hydrogen targets.

Relation to other proposals

Our proposal has no direct relation to other approved proposals, except that similar measurements have been proposed an approved for the proton. These are the first coherent DVCS and DVMP measurements that are proposed for a ^{4}He target.

Appendix A

Twist-2 $e\ ^4He \to e\ ^4He\ \gamma$ cross section

Following the definitions of reference [31], the variables that appear in equations 2.3 to 2.5 are defined as:

$\mathcal{P}_1(\phi)$ and $\mathcal{P}_2(\phi)$ are BH propagators and defined as:

$$\mathcal{P}_1(\phi) = \frac{(k-q')^2}{Q^2} = -\frac{1}{y(1+\varepsilon^2)}\left[J + 2K\cos(\phi)\right] \tag{A.1}$$

$$\mathcal{P}_2(\phi) = \frac{(k-\Delta)^2}{Q^2} = 1 + \frac{t}{Q^2} + \frac{1}{y(1+\varepsilon^2)}\left[J + 2K\cos(\phi)\right] \tag{A.2}$$

with,

$$J = \left(1 - y - \frac{y\varepsilon^2}{2}\right)\left(1 + \frac{t}{Q^2}\right) - (1-x_A)(2-y)\frac{t}{Q^2} \tag{A.3}$$

$$K^2 = -\delta t\,(1-x_A)\left(1 - y - \frac{y^2\varepsilon^2}{4}\right)\left\{\sqrt{1+\varepsilon^2} + \frac{4x_A(1-x_A)+\varepsilon^2}{4(1-x_A)}\delta t\right\} \tag{A.4}$$

$$\delta t = \frac{t - t_{min}}{Q^2} = \frac{t}{Q^2} + \frac{2(1-x_A)\left(1 - \sqrt{1+\varepsilon^2}\right) + \varepsilon^2}{4x_A(1-x_A) + \varepsilon^2} \tag{A.5}$$

where t_{min} represents the kinematic boundary of the process and defined as:

$$t_{min} = Q^2\frac{2(1-x_A)(1-\sqrt{1+\varepsilon^2}) + \varepsilon^2}{4x_A(1-x_A) + \varepsilon^2} \tag{A.6}$$

The Fourier coefficients, in equations 2.3, 2.4 and 2.5, of a spin-0 target are defined as:

$$c_0^{BH} = \left[\ \left\{(2-y)^2 + y^2(1+\varepsilon^2)^2\right\}\left\{\frac{\varepsilon^2 Q^2}{t} + 4(1-x_A) + (4x_A+\varepsilon^2)\frac{t}{Q^2}\right\}\right.$$

$$+2\varepsilon^2\left\{4(1-y)(3+2\varepsilon^2) + y^2(2-\varepsilon^4)\right\} - 4x_A^2(2-y)^2(2+\varepsilon^2)\frac{t}{Q^2}$$

$$\left. +8K^2\frac{\varepsilon^2 Q^2}{t} \ \right] F_A^2(t) \tag{A.7}$$

$$c_1^{BH} = -8(2-y)K\left\{2x_A + \varepsilon^2 - \frac{\varepsilon^2 Q^2}{t}\right\} F_A^2(t) \tag{A.8}$$

$$c_2^{BH} = 8K^2\frac{\varepsilon^2 Q^2}{t}F_A^2(t) \tag{A.9}$$

where $F_A(t)$ is the electromagnetic form factor of the ^{4}He. At leading twist, the $|\mathcal{T}_{DVCS}|^2$ writes as a function of only one CFF according to

$$c_0^{DVCS} = 2\frac{2-2y+y^2+\frac{\varepsilon^2}{2}y^2}{1+\varepsilon^2}\mathcal{H}_A\mathcal{H}_A^\star \tag{A.10}$$

and the interference amplitude coefficients are written as:

$$s_1^{INT} = F_A(t)\Im m(\mathcal{H}_A)S_{++}(1), \tag{A.11}$$

with

$$S_{++}(1) = \frac{-8K(2-y)y}{1+\varepsilon^2}\left(1 + \frac{1-xA+\frac{\sqrt{1+\varepsilon^2}-1}{2}}{1+\varepsilon^2}\frac{t-t_{min}}{Q^2}\right)\cdot F_A(t) \tag{A.12}$$

$$c_0^{INT} = F_A(t)\Re e(\mathcal{H}_A)C_{++}(0), \tag{A.13}$$

with

$$C_{++}(0) = \frac{-4(2-y)(1+\sqrt{1+\varepsilon^2})}{(1+\varepsilon^2)^2}\left\{\frac{\widetilde{K}^2}{Q^2}\frac{(2-y)^2}{\sqrt{1+\varepsilon^2}}\right. \tag{A.14}$$

$$\left. + \ \frac{t}{Q^2}\left(1-y-\frac{\varepsilon^2}{4}y^2\right)(2-x_A)\left(1 + \frac{2x_A(2-x_A+\frac{\sqrt{1+\varepsilon^2}-1}{2}+\frac{\varepsilon^2}{2x_A})\frac{t}{Q^2}+\varepsilon^2}{(2-x_A)(1+\sqrt{1+\varepsilon^2})}\right)\right\}$$

$$c_1^{INT} = F_A(t)\Re e(\mathcal{H}_A)C_{++}(1), \tag{A.15}$$

with

$$
\begin{aligned}
C_{++}(1) \;=\; & \frac{-16K(1 - y + \frac{\varepsilon^2}{4}y^2)}{(1+\varepsilon^2)^{5/2}} \left\{ \left(1 + (1 - x_A)\frac{\sqrt{1+\varepsilon^2} - 1}{2x_A} + \frac{\varepsilon^2}{4x_A} \right) \frac{x_A t}{Q^2} - \frac{3\varepsilon^2}{4.0} \right\} \\
& - \; 4K \left(2 - 2y + y^2 + \frac{\varepsilon^2}{2}y^2 \right) \frac{1 + \sqrt{1+\varepsilon^2} - \varepsilon^2}{(1+e2)^{5/2}} \left\{ 1 - (1 - 3x_A)\frac{t}{Q^2} \right. \\
& \left. + \frac{1 - \sqrt{1+\varepsilon^2} + 3\varepsilon^2}{1 + \sqrt{1+\varepsilon^2} - \varepsilon^2} \frac{x_A * t}{Q^2} \right\}
\end{aligned}
\tag{A.16}
$$

Bibliography

[1] J. J. Aubert *et al.*, "The ratio of the nucleon structure functions $F2_n$ for iron and deuterium," *Phys. Lett.*, vol. B123, pp. 275–278, 1983.

[2] G. A. Miller and J. R. Smith, "Return of the emc effect.," *Phys.Rev.*, vol. C65, p. 015211, 2002.

[3] A. W. Thomas, "New insight into nuclear structure from qcd," *Annalen Phys*, vol. 13, pp. 731–739, 2004.

[4] S. Liuti and S. K. Taneja, "Nuclear medium modifications of hadrons from generalized parton distributions," *Phys. Rev.*, vol. C72, p. 034902, 2005.

[5] A. H. Rezaeian and H.-J. Pirner, "The nuclear matter stability in a non-local chiral quark model," *Nucl. Phys.*, vol. A769, pp. 35–52, 2006.

[6] Z.-m. He, X.-x. Yao, C.-g. Duan, G.-l. Li, and H.-g. Peng, "Double Q**2 rescaling model and the nuclear effect of the parton distribution functions," *Eur. Phys. J.*, vol. C4, pp. 301–306, 1998.

[7] A. Accardi, D. Grunewald, V. Muccifora, and H. J. Pirner, "Atomic mass dependence of hadron production in deep inelastic scattering on nuclei," *Nucl. Phys.*, vol. A761, pp. 67–91, 2005.

[8] A. Accardi, D. Grunewald, V. Muccifora, and H. Pirner, "Erratum: Atomic mass dependence of hadron production in deep inelastic scattering on nuclei," 2005.

[9] A. Kirchner and D. Mueller, "Deeply virtual Compton scattering off nuclei," *Eur. Phys. J.*, vol. C32, pp. 347–375, 2003.

[10] M. Burkardt, "Impact parameter dependent parton distributions and off-forward parton distributions," *Phys. Rev.*, vol. D62, p. 071503, 2000.

[11] M. Diehl, "Generalized parton distributions in impact parameter space," *Eur.Phys.J.*, vol. C25, pp. 223–232, 2002.

[12] A. V. Belitsky and D. Mueller, "Nucleon hologram with exclusive leptoproduction," *Nucl. Phys.*, vol. A711, pp. 118–126,, 2002.

[13] M. Burkardt, "Transverse deformation of parton distributions and transversity decomposition of angular momentum," *Phys. Rev.*, vol. D72, p. 094020, 2005.

[14] M. Hattawy *et al.* (EG6 Working Group), "Deeply Virtual Compton Scattering off ^{4}He," *CLAS internal analysis note*, 2016.

[15] M. V. Polyakov, "Generalized parton distributions and strong forces inside nucleons and nuclei," *Phys. Lett.*, vol. B555, pp. 57–62, 2003.

[16] J. Gomez *et al.*, "Measurement of the A-dependence of deep inelastic electron scattering," *Phys.Rev.*, vol. D49, pp. 4348–4372, 1994.

[17] F. E. Close, R. G. Roberts, and G. G. Ross, "The Effect of Confinement Size on Nuclear Structure Functions," *Phys. Lett.*, vol. B129, p. 346, 1983.

[18] O. Nachtmann and H. J. Pirner, "Color Conductivity in Nuclei and the EMC Effect," *Z. Phys.*, vol. C21, p. 277, 1984.

[19] R. L. Jaffe, F. E. Close, R. G. Roberts, and G. G. Ross, "On the Nuclear Dependence of Electroproduction," *Phys. Lett.*, vol. B134, p. 449, 1984.

[20] F. E. Close, R. G. Roberts, and G. G. Ross, "Factorization Scale Independence, the Connection between Alternative Explanations of the EMC Effect and QCD Predictions for Nuclear Properties," *Nucl. Phys.*, vol. B296, p. 582, 1988.

[21] S. Liuti and S. K. Taneja, "Microscopic description of deeply virtual Compton scattering off spin-0 nuclei," *Phys. Rev.*, vol. C72, p. 032201, 2005.

[22] V. Guzey and M. Strikman, "DVCS on spinless nuclear targets in impulse approximation," *Phys. Rev.*, vol. C68, p. 015204, 2003.

[23] V. Guzey and M. Siddikov, "On the A-dependence of nuclear generalized parton distributions," *J. Phys.*, vol. G32, pp. 251–268, 2006.

[24] S. Scopetta, "Generalized parton distributions of He-3," *Phys. Rev.*, vol. C70, p. 015205, 2004.

[25] F. X. Girod, M. Guidal, A. Kubarovsky, V. Kubarovsky, P. Stoler, C. Weiss, *et al.* Proposal to Jefferson Lab PAC39, Exclusive Phi Meson Electroproduction with CLAS12: PR12-12-007, 2012.

[26] A. Accardi *et al.*, "Electron Ion Collider: The Next QCD Frontier - Understanding the glue that binds us all," 2012.

[27] A. V. Belitsky and A. V. Radyushkin, "Unraveling hadron structure with generalized parton distributions," *Phys. Rept.*, vol. 418, pp. 1–387, 2005.

[28] M. Burkardt, "Impact parameter space interpretation for generalized parton distributions," *Int. J. Mod. Phys.*, vol. A18, pp. 173–208, 2003.

[29] A. L. H. A. C. Camsonne, "Jlab measurement of the ^{4}He charge form factor at large momentum transfers," *Phys. Rev. Lett.*, vol. 112, p. 132503, Apr 2014.

[30] R. F. Frosch, J. S. McCarthy, R. E. Rand, and M. R. Yearian, "Structure of the he^4 nucleus from elastic electron scattering," *Phys. Rev.*, vol. 160, pp. 874–879, Aug 1967.

[31] A. V. Belitsky and D. Mueller, "Refined analysis of photon leptoproduction off spinless target," *Phys. Rev.*, vol. D79, p. 014017, 2009.

[32] F. Ellinghaus, R. Shanidze, and J. Volmer, "Deeply-virtual Compton scattering on deuterium and neon at HERMES," *AIP Conf. Proc.*, vol. 675, pp. 303–307, 2003.

[33] M. Mazouz *et al.*, "Deeply Virtual Compton Scattering off the neutron," *Phys. Rev. Lett.*, vol. 99, 2007.

[34] A. V. Belitsky, D. Mueller, A. Kirchner, and A. Schafer, "Twist-three analysis of photon electroproduction off pion," *Phys. Rev.*, vol. D64, p. 116002, 2001.

[35] F. X. Girod *et al.*, "Measurement of Deeply virtual Compton scattering beam-spin asymmetries," *Phys. Rev. Lett.*, vol. 100, p. 162002, 2008.

[36] H. S. Jo *et al.*, "Cross sections for the exclusive photon electroproduction on the proton and Generalized Parton Distributions," *Phys. Rev. Lett.*, vol. 115, no. 21, p. 212003, 2015.

[37] V. Guzey, "Neutron contribution to nuclear DVCS asymmetries," *Phys. Rev.*, vol. C78, p. 025211, 2008.

[38] A. Airapetian *et al.*, "Nuclear-mass dependence of azimuthal beam-helicity and beam-charge asymmetries in deeply virtual Compton scattering," *Phys. Rev.*, vol. C81, p. 035202, 2010.

[39] "CLAS12 Technical Design Report," 2008.

[40] J. Peyré, B. Genolini, and J. Poutas, "A Full-Scale Prototype for the Tracking Chambers of the ALICE Muon Spectrometer," 1998.

[41] T. Abe *et al.*, "Belle II Technical Design Report," 2010.

[42] E. Etzion *et al.*, "The Certification of ATLAS Thin Gap Chambers Produced in Israel and China," 2004.

[43] S. Biagi, "Monte Carlo simulation of electron drift and diffusion in counting gases under the influence of electric and magnetic fields," *Nucl.Instrum.Meth.*, vol. A421, pp. 234–240, 1999.

[44] M. Battaglieri *et al.*, "The Heavy Photon Search test detector," *Nucl.Instrum.Meth.*, vol. A777, pp. 91–101, 2015.

[45] T. C. Collaboration, "Clas12 forward tagger (ft) technical design report." https://www.jlab.org/Hall-B/clas12-web/docs/ft-tdr.2.0.pdf, 2012. Online; accessed 29 January 2016.

[46] K. Emi *et al.*, "Study of a dE/ dx measurement and the gas-gain saturation by a prototype drift chamber for the BELLE-CDC," *Nucl. Instrum. Meth.*, vol. A379, pp. 225–231, 1996.

[47] H. Fenker *et al.*, "BoNus: Development and use of a radial TPC using cylindrical GEMs," *Nucl. Instrum. Meth.*, vol. A592, pp. 273–286, 2008.

[48] M. Amaryan *et al.*, "The Structure of the Free Neutron at Large x-Bjorken (PR12-06-113)," *A proposal to PAC 30*, 2006.

[49] M. Guidal, H. Moutarde, and M. Vanderhaeghen, "Generalized Parton Distributions in the valence region from Deeply Virtual Compton Scattering," *Rept. Prog. Phys.*, vol. 76, p. 066202, 2013.

[50] J. M. e. a. Grames, "Unique electron polarimeter analyzing power comparison and precision spin-based energy measurement," *Phys. Rev. ST Accel. Beams*, vol. 7, p. 042802, Apr 2004.

[51] K. Lukashin *et al.*, "Exclusive electroproduction of phi mesons at 4.2-GeV," *Phys. Rev.*, vol. C63, p. 065205, 2001.

[52] J. P. Santoro *et al.*, "Electroproduction of $\phi(1020)$ mesons at $1.4 < Q^2 < 3.8 GeV^2$ measured with the CLAS spectrometer," *Phys. Rev.*, vol. C78, p. 025210, 2008.

[53] R. L. Dixon, R. Galik, D. Larson, A. Silverman, M. Herzlinger, S. D. Holmes, F. M. Pipkin, S. Raither, and R. L. Wagner, "Spectrometer study of ϕ meson electroproduction," *Phys. Rev.*, vol. D19, p. 3185, 1979.

[54] D. G. Cassel *et al.*, "Exclusive ρ^0, ω and ϕ Electroproduction," *Phys. Rev.*, vol. D24, p. 2787, 1981.

[55] A. Borissov. in Proceedings of Meson 2000 Workshop, Cracow, Poland, May 19 through 23, 2000.

[56] M. Arneodo *et al.*, "Exclusive rho0 and phi muoproduction at large q**2," *Nucl. Phys.*, vol. B429, pp. 503–529, 1994.

[57] S. Chekanov *et al.*, "Exclusive electroproduction of phi mesons at HERA," *Nucl. Phys.*, vol. B718, pp. 3–31, 2005.

[58] F. D. Aaron *et al.*, "Diffractive Electroproduction of rho and phi Mesons at HERA," *JHEP*, vol. 05, p. 032, 2010.

[59] A. Aktas *et al.*, "Measurement of event shape variables in deep-inelastic scattering at HERA," *Eur. Phys. J.*, vol. C46, pp. 343–356, 2006.

[60] S. V. Goloskokov and P. Kroll, "The Role of the quark and gluon GPDs in hard vector-meson electroproduction," *Eur. Phys. J.*, vol. C53, pp. 367–384, 2008.

[61] M. Diehl, W. Kugler, A. Schafer, and C. Weiss, "Exclusive channels in semi-inclusive production of pions and kaons," *Phys. Rev.*, vol. D72, p. 034034, 2005. [Erratum: Phys. Rev.D72,059902(2005)].

[62] M. Golembiovskaya (HERMES collaboration). AIP Conf.Proc.1350:60-63,2011; A. Borissov, AIP Conf.Proc.1105:19-23,2009.